NORTHWESTERN UNIVERSITY

Three-Dimensional Image Reconstruction From Multi-Focus Microscopy

A DISSERTATION

SUBMITTED TO THE GRADUATE SCHOOL

IN PARTIAL FULFILLMENT OF THE REQUIREMENTS

for the degree

DOCTOR OF PHILOSOPHY

Field of Electrical Engineering and Computer Science

By

Seunghwan Yoo

EVANSTON, ILLINOIS

September 2018

ABSTRACT

Three-Dimensional Image Reconstruction From Multi-Focus Microscopy

Seunghwan Yoo

In this dissertation thesis, I introduce three-dimensional (3D) image reconstruction algorithms for multi-focus microscopy (MFM). MFM provides a fast way to obtain 3D information of the sample by simultaneously capturing multiple focal planes on a single camera shot. However, stacking the sub-images from different focal planes does not provide a good reconstruction of 3D image because of low signal-to-noise ratio (SNR) and severe out-of-focus blur of the microscopy. I analyze different models of the imaging process for MFM and derive multiple ways of 3D image reconstruction. First, I present image reconstruction methods based on models that assume Gaussian noise in the observation. As a base algorithm, I present a total-variation (TV) regularized least squares (RLS) algorithm for image reconstruction. We have developed two different algorithms to improve the performance of image reconstruction by using (1) multiple-frame processing, and (2) joint parameter estimation through a Bayesian framework, respectively. Multiple-frame processing utilizes the information from neighboring frames in addition to the current frame to improve the image quality. For joint parameter estimation, maximum-a-posteriori (MAP) is used for automatic estimation of the regularization parameter as well as 3D image reconstruction. Poisson noise model

is also investigated to handle the low photon resource of MFM. For this, I present an alternating directions methods of multipliers (ADMM) based image reconstruction algorithm. This method splits the Poisson image deconvolution problem into two simpler problems - deblurring and Poisson denoising problems, providing an efficient way to solve the optimization problem. Experimental results with synthetic and real data verify the effectiveness of the methods.

Acknowledgements

I would like to thank my advisor, Prof. Katsaggelos for his guidance and advice throughout my Ph.D study. His support has been essential in many ways. He motivates me to work hard and push forward myself to be a better researcher. His expertise in image restoration helps me to get my research work progress. Also, he gave opportunities to colloaborate with other groups, which leverage my research, and broaden my views.

I would like to thank Prof. Cossairt and Dr. Gursoy for their co-supervision. Prof. Cossairt has provided great intuitions for many problems we encountered and suggested creative ideas, being my inspiration. Dr. Gursoy supervised me during my internship at Argonne National Laboratory (ANL). He is a knowelegable and experienced researcher, broadening my research experience.

I would like to thank Pablo for going through the mathematical details of the methods we developed. As an expert in Bayesian theory and inverse problems, he provides good intuitions on the problems and ideas on how to solve them.

I thank all the colleagues from CompPhoto Lab, ANL and University of Chicago for helpful discussions and sharing different expertise. I also thank IVPLers for their friendship and comradeship.

I also thank my family including parents, sisters, and brothers, and friends for their unceasing prayer, encouragement, and support. I am so grateful to my dear wife, Josie, who

has suffered together throughout the whole journey. Without her spiritual, moral, and food support, I would not be able to make it this far.

Lastly but most importantly I would like to thank God for His grace, provision, and guidance. All glory to Him!

Table of Contents

List of Tables

List of Figures

CHAPTER 1

Introduction

Fluorescence microscopy is an essential imaging tool in biology and biomedial sciences [1]. It enables observation and visualization of the physiology of the living cells at sub-cellular resolution. It makes use of a property of fluorophores that when they are excited by specific band of light, they emit a different band of wavelength of light. Once the samples are dyed with fluorophores, the sample can be observed as the emitted light from the sample is captured on the camera. Thanks to its sub-cellular resolution and non-invasive and high biochemical labeling, the structure and dynamics of the living cells can be observed.

There have been advances of fluoroscene microscopy techniques over the past decade increasing its capability to capture higher resolution image in different aspects - lateral resolution, axial resolution, and temporal resolution [2, 3]. Confocal microscopy increases the resolution in the optical axis by using pinhole in front of the detector, blocking the out-of-focus light [4, 5]. Structured illumination fluoroscence microscopy (SIM) achieves super-resolution in the spatial domain by using the structured illumination, increasing the support of the signal in the frequency domain [6, 7]. Light-sheet fluoroscence microscopy uses an orthogonal emisson configuration in order to only excite the sample inside a selective plane each time [8, 9]. It improves the spatial resolution of the microscopy by reducing the emission from other planes. Stimulated emission depletion (STED) fluorescence microscopy reduces the size of effective point spread function (PSF) through stimulated emission with a second laser beam, achieving super-resolution [10, 11].

The aforementioned microscopies increase spatial resolution but they require sequential refocusing for three-dimensional (3D) imaging, and therefore they lack of high temporal resolution. Multi-plane microscopy (MUM) [12,13] and multi-focus microscopy (MFM) [14] are developed to increase temporal resolution for microscopy. They capture multiple focal planes simultaneously, providing 3D information in a fast way.

1.1. Multi-Focus Microscopy

Fast acquisition of 3D data is one of the challenges in modern microscopy. Conventional microscopy only captures the information from a single focal plane. To obtain 3D data in the microscopy, they must capture each focal plane one by one, changing the focus in-between. This sequential refocusing has serious disadvantages: (1) it is too slow to capture fast movement of 3D samples, (2) it is prone to photobleaching, and (3) the stage movement for refocusing can cause perturbation of the sample.

Multi-plane microscopy (MUM) mitigates these limitations and thus allows tracking of the living sample in 3D space at high temporal resolution [12, 13]. It splits the light from different focal planes into different paths and captures each focal planes with a different camera. However, their system is only able to capture up to four focal planes which corresponds the number of cameras. It is useful for object localization or tracking but it is not suitable for imaging extended objects.

Multi-focus microscopy (MFM) provides a fast way to obtain 3D information of the sample by simultaneously capturing multiple focal planes on a single camera [14–18]. MFM uses a diffractive grating to form multiple focus-shifted images. It splits the light from different focal depths of the sample into separate paths and forms an array of $K \times K$ images on the camera. Figure 1.1 illustrates the difference between a conventional microscope and an

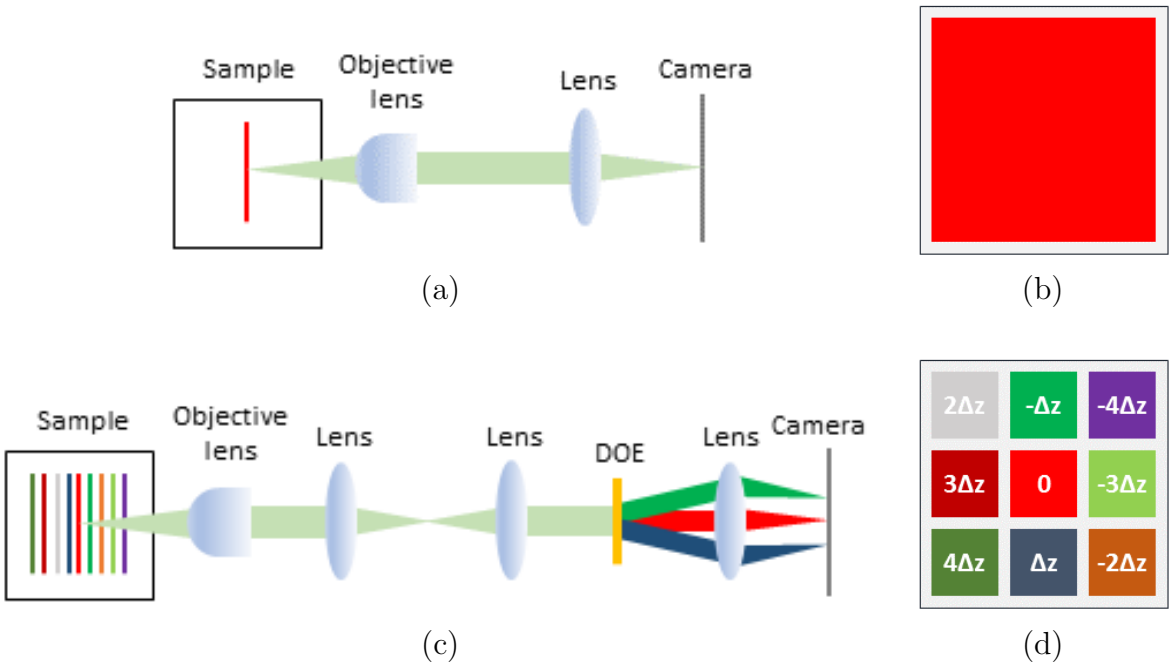

Figure 1.1. Conventional microscopy vs. MFM. (a, b) Schematic and captured information of conventional microscopy, and (c, d) schematic and captured information of MFM.

MFM. Figure 1.1 (a) and (b) show the schematic of conventional microscopy and the captured data on its camera. The optical system of the conventional microscope only focuses on a single plane (red colored), and the camera captures information from the focal plane. On the other hand, MFM contains additional components including two lens and a diffractive optical element (DOE) to split the light from different focal planes as shown in Figure 1.1 (c). The data captured on the camera is composed of 3×3 sub-images from different focal depths as shown in Figure 1.1 (d), and thus it gives information in 9 different depths $(-4\Delta z, -3\Delta z, \cdots, 3\Delta z, 4\Delta z)$. Note that the pixel resolution in the lateral (xy) plane is reduced in order to get the volumetric information in MFM.

Figure 1.2 shows two MFM experimental measurements of a tumbling fluorescently labelled bacterium. These two frames are picked from 1023-frame video. In this MFM setup,

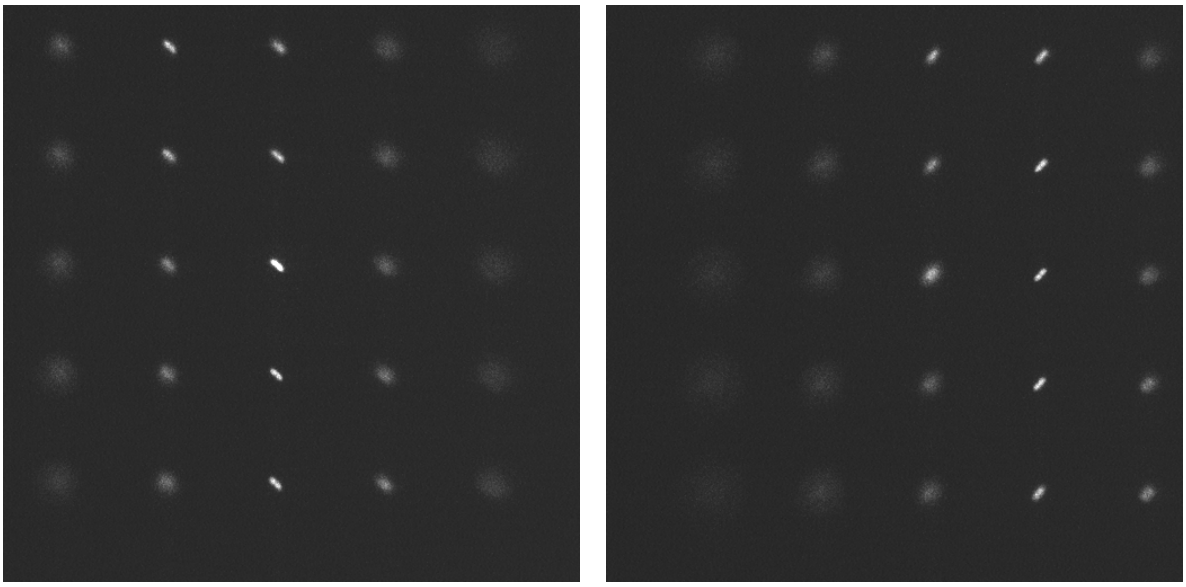

(a) (b)

Figure 1.2. MFM experimental measurement of a tumbling fluorescently labelled bacterium. A MFM measurement is composed of 5 by 5 sub-images with different focal planes. (a) The signal is stronger in the sub-images in the center, which means the bacterium is located in the middle in the z-axis. (b) The bacterium is in a different position and in a different location from MFM image (a)

a MFM measurement is composed of 5 by 5 sub-images with different focal planes [17]. The movement of the bacterium is observed between two frames. The signal in Fig. 1.2 (a) is stronger in the sub-image in the center, which means the bacterium is located in the center in the z-axis. The bacterium in Fig. 1.2 (b) is away from the center in the z-axis since it is more focused on a different sub-image.

1.2. Image Reconstruction

Image reconstruction and image restoration problems include image deconvolution [19–29], image deblurring [30–34], image denoising [35–40], and image super-resolution [41–47]. The goal of these problems is to estimate the original, clear, noiseless, high-resolution image

for a given blurred, noisy, or/and down-sampled observation. These problems are essentially inverse problems in very high dimensions and a great deal of efforts have been made and applied to different imaging systems [48–57].

In most cases, the image degradation process is modeled as a linear model with noise as follows:

$$\mathbf{g} = \mathcal{N}(\mathbf{H}\mathbf{f}), \tag{1.1}$$

where $\mathbf{f} \in \mathbb{R}^{N\times 1}$, $\mathbf{g} \in \mathbb{R}^{M\times 1}$, and $\mathbf{H} \in \mathbb{R}^{M\times N}$ denote the original image to be restored, the degraded image, and the point spread function (PSF) matrix which characterizes blurring and downsampling. $\mathcal{N}(\cdot)$ is a noise operator, which is usually assumed as Gaussian noise or Poisson noise depending on the imaging system.

With an assumption of Gaussian noise, it is natural to formulate least squares (LS) for image reconstruction as follows:

$$\hat{\mathbf{f}} = \arg\min_{\mathbf{f}} \ \|\mathbf{g} - \mathbf{H}\mathbf{f}\|^2, \tag{1.2}$$

whose analytical solution is

$$\hat{\mathbf{f}} = (\mathbf{H}^T\mathbf{H})^{-1}\mathbf{H}^T\mathbf{g}. \tag{1.3}$$

Note that in most cases, however, this cannot be solved directly as Eq. 1.3 for image reconstruction. Because $\mathbf{f}$ is high dimensional, it is not feasible to store $\mathbf{H}$ in memory nor calculate its inverse in general. Instead, iterative methods are used to solve the linear system or filtering operation in frequency domain is performed for some cases.

The LS solution is equivalent to the solution maximizing the likelihood function, $p(\mathbf{g}|\mathbf{f})$, assuming independent identically distributed (i.i.d.) Gaussian noise ($\sim \mathcal{N}(0, \sigma^2\mathbf{I})$) as

$$\hat{\mathbf{f}} = \arg\max_{\mathbf{f}} \; p(\mathbf{g}|\mathbf{f}) \tag{1.4}$$

$$= \arg\min_{\mathbf{f}} \; -\log p(\mathbf{g}|\mathbf{f}) \tag{1.5}$$

LS works when the number of unknowns is larger than or equal to the number of known variables ($M \geq N$) and $\mathbf{H}$ is well-conditioned, but it is often not the case. $\mathbf{H}$ is usually ill-conditioned so the presence of noise causes a bad solution. A common way to solve this issue is regularization. Adding a regularization term to the objective function of LS in Eq. 1.2 stabilizes the solution, and significantly improve the quality of the solution. The regularized least squares (RLS) is formulated as

$$\hat{\mathbf{f}} = \arg\min_{\mathbf{f}} \; \|\mathbf{g} - \mathbf{H}\mathbf{f}\|^2 + \lambda\Phi(\mathbf{f}) \tag{1.6}$$

where λ is a regularization parameter, and $\Phi(\cdot)$ is a regularization function.

RLS is equivalent to finding $\mathbf{f}$ that maximizes the posterior distribution, $p(\mathbf{f}|\mathbf{g})$, as

$$\hat{\mathbf{f}} = \arg\max_{\mathbf{f}} \; p(\mathbf{f}|\mathbf{g}) \tag{1.7}$$

$$= \arg\max_{\mathbf{f}} \; p(\mathbf{g}|\mathbf{f})p(\mathbf{f}) \tag{1.8}$$

$$= \arg\min_{\mathbf{f}} \; -\log p(\mathbf{g}|\mathbf{f})p(\mathbf{f}) \tag{1.9}$$

$$= \arg\min_{\mathbf{f}} \; -\log p(\mathbf{g}|\mathbf{f}) - \log p(\mathbf{f}) \tag{1.10}$$

where $p(\mathbf{f})$ denotes the prior distribution. Note that, in this perspective, the prior is the counterpart of the regularization term of RLS.

Regularization function has an important role in image reconstruction. Different regularization functions will result in different solutions, and thus a proper regularization function must be chosen to obtain better solutions. In order to choose the right regularization function, we use the high level prior information that we know about the solution. For example, $\Phi(\mathbf{f}) = \|\mathbf{f}\|_2^2$ finds a solution whose magnitude is small, and $\Phi(\mathbf{f}) = TV(\mathbf{f})$ finds a piecewise smoothness solution. In addition, solvability is a critical criterion to choose the regularization function. Even though it reflects the signal well, there may be no way to solve the optimization problem with some regularization function.

There are several types of regularization function that are widely used in image reconstruction. First, Tikhonov regularization, $\Phi(\mathbf{f}) = \|\mathbf{C}\mathbf{f}\|_2^2$, is a $l2$ norm regularization that enforces small magnitude ($\mathbf{C} = \mathbf{I}$) or smootheness ($\mathbf{C}$: Laplacian operator) of the signal. The analytical solution of the RLS with this regularization term exists as

$$\hat{\mathbf{f}} = (\mathbf{H}^T\mathbf{H} + \lambda\mathbf{C}^T\mathbf{C})^{-1}\mathbf{H}^T\mathbf{g}, \tag{1.11}$$

which can be solved iteratively or in frequency domain similar to LS.

Total variation (TV) regularization has been popular in signal processing since Rudin *et al.* developed the TV regualrized denoising algorithm [35]. The TV regularization function (2D) is defined as

$$\mathrm{TV}(\mathbf{f}) = \sum_{i=1}^{N} \sqrt{(\Delta_i^x \mathbf{f})^2 + (\Delta_i^y \mathbf{f})^2} \tag{1.12}$$

where i is an index for pixels, and Δ^x and Δ^y denote the first difference operator along the x, and y directions, respectively. It enforces piecewise smoothness, so it effectively removes noise while preserving the edges. It is a non-smooth function so it is not simple to optimize RLS with TV regularization but effective algorithms have been developed as in [26, 35, 36, 58].

Finally, $l1$ norm regularization, $\Phi(\mathbf{f}) = \|\mathbf{f}\|_1$, which enforces sparsity of the signal, has become popular with the advent of compressive sensing theory [59–61]. The theory proves that a sparse signal can be perfectly restored from small portion of the observation by using sparsity regularization under certain condition. Natural signals such as audio and image can be represented as sparse signals in some domain, thus sparsity regularization have been successfully used. In fact, TV regularization can be seen as sparsity regularization in gradient domain. $l1$ norm is, like TV prior, non-smooth, but highly efficient algorithms have been developed [62, 63], to name a few, iterative shrinkage thresholding algorithm (ISTA), two-step ISTA (TwIST), and fast ISTA (FISTA) [24, 25].

1.3. Scope of the Dissertation

In this dissertation, I analyze different models of the imaging process for MFM and propose algorithms for 3D image reconstruction. First, I review MFM imaging models based on two noise models: (1) Gaussian noise, and (2) Poisson noise. Then I introduce three different image reconstruction methods in three different chapters.

The first two methods are based on imaging models that assume Gaussian noise in the observation. We have developed two different algorithms to improve the performance of image reconstruction by using (1) multiple-frame processing, and (2) joint parameter estimation through a Bayesian framework, respectively. Multiple-frame processing utilizes the information from neighboring frames in addition to the current frame to improve the image quality. For joint parameter estimation, maximum-a-posteriori (MAP) is used for automatic estimation of the regularization parameter as well as the 3D image.

Poisson noise model is also investigated to handle the low-light-level measurement of MFM. I present an alternating directions methods of multipliers (ADMM) based image

reconstruction algorithm. This method separates the Poisson image deconvolution problem into two simpler problems - deblurring and Poisson denoising problems, providing an efficient way to solve the optimization problem.

Experimental results with synthetic and real data verify the effectiveness of the methods, which means they will make it possible to capture 4D (3D space + time) events of the samples.

The rest of this dissertation is outlined as follows:

- Chapter 2: we review the acquisition models for MFM. General imaging models for fluorescence microscopy will be introduced first, and two noise models will be described as MFM acquisition models based on them. We also develop the 3D reconstruction algorithms for based on the acquisition models. The methods we present in this chapter will be the bases for the proposed methods in Chapter 3, 4, and 5.
- Chapter 3: we present multiple-frame MFM 3D image reconstruction algorithms. First, we introduce the MFM system, and the single-frame 3D reconstruction algorithm for MFM. We propose to use information from multiple frames with two different schemes - (1) the batch approach and (2) the recursive approach, to improve the performance of 3D image reconstruction.
- Chapter 4: we present a Bayesian modeling of the problem of 3D image reconstruction from MFM measurement. The MFM acquisition system is modeled by likelihood function, which takes into account two different noise schemes: (1) the same noise for all the tiles, and (2) different noise for each tile. Then we propose to use a prior model based on the TV norm. The reconstructed 3D object as well

as the parameters of the model are estimated using maximum a posteriori (MAP) inference.

- Chapter 5: we present a Poisson noise model for the imaging system and ADMM-based image reconstruction algorithms for it. By using ADMM, we split the complex problem into two simpler problems - deblurring and Poisson denosing. We use the Bayesian approach from Chapter 4 for deblurring with estimation of the regularization parameter. The step for the background signal estimation is also incorporated in the ADMM framework.
- Chapter 6: we conclude the thesis along with prospect discussing remaining challenges and potential future work.

CHAPTER 2

Review of Acquisition Models for Multi-Focus Microscopy

In this chapter, we review mathematical models for multi-focus microscopy (MFM) imaging system and corresponding image reconstruction methods. We describe general forward models for fluorescence microscopy and MFM, and then, introduce two different noise models: Gaussian and Poisson noise models. Based on these two noise models, we model the acquisition process for MFM in two different ways. We also derive the formulation for image reconstruction from the two acquisition models by using their likelihood function and regularization terms. This chapter is the review for mathematical models of MFM imaging system and corresponding image reconstruction methods and guide for the following chapters, but it does not have any experiment.

2.1. Acquisition Models for MFM

2.1.1. Acquisition Model for Fluorescence Microscopy

Fluorescence microscopy produces a two-dimensional (2D) image from a 3D sample. This process involves 3D convolution between the point spread function (PSF) of the system and the 3D sample, and extraction of the focused plane or $z = 0$ without loss of generality. The captured image also contains a background signal that comes from scattering and reflection of fluorescence light in the medium, which can be approximated as a uniform signal. Also, random noise will be involved in imaging process. Noise can come from multiple sources

such as electrical circuit of the sensor, shot noise from quantum fluctuation, quantization error, etc.

Let $\mathbf{f} \in \mathbb{R}^{N\times 1}$, $\mathbf{g} \in \mathbb{R}^{M\times 1}$, and $\mathbf{b} \in \mathbb{R}^{M\times 1}$ denote the lexicographical representation of the original image, the observed image, and the background signal, and $\mathbf{H} \in \mathbb{R}^{N\times N}$ and $\mathbf{D} \in \mathbb{R}^{M\times N}$ the PSF matrix that characterizes blurring from the optical system, and the extraction matrix, respectively. Considering all the factors above, the image acquisition process of fluorescence microscope can be generally modeled as

$$\mathbf{g} = \mathcal{N}(\mathbf{DHf} + \mathbf{b}), \tag{2.1}$$

$$= \mathcal{N}(\mathbf{Kf} + \mathbf{b}), \tag{2.2}$$

where $\mathbf{K} = \mathbf{DH}$, and $\mathbf{D} \in \mathbb{R}^{M\times N}$ and $\mathbf{H} \in \mathbb{R}^{N\times N}$ are the extraction and the PSF matrices, respectively. $\mathcal{N}(\cdot)$ denotes noise operator, which is usually assumed as Gaussian noise or Poisson noise depending on the imaging system.

2.1.2. Acquisition Model for MFM

MFM produces a 2D image that contains multiple sub-images (or tiles) from a 3D sample. PSF for each tile is unique because it is focused on a different position in the z axis, and it also has different shapes due to chromatic aberration from the DOE. Let $\mathbf{g}^j \in \mathbb{R}^{M_t\times 1}$ and $\mathbf{H}^j \in \mathbb{R}^{N\times N}$ denote the j-th tile on a MFM image and the corresponding PSF, respectively. Then, the acquisition process for the j-th tile of MFM is modeled as

$$\mathbf{g}^j = \mathcal{N}(\mathbf{DH}^j\mathbf{f} + \mathbf{b}^j) \tag{2.3}$$

$$= \mathcal{N}(\mathbf{K}^j\mathbf{f} + \mathbf{b}), \tag{2.4}$$

where $j = 1, \ldots, N_t$, with N_t being the number of tiles for MFM.

Then, the whole observation including all the tiles can be represented as

$$\mathbf{g} = \mathcal{N}(\mathbf{K}\mathbf{f} + \mathbf{b}), \tag{2.5}$$

where

$$\mathbf{g} = \begin{bmatrix} \mathbf{g}^1 \\ \vdots \\ \mathbf{g}^{N_t} \end{bmatrix}, \mathbf{K} = \begin{bmatrix} \mathbf{K}^1 \\ \vdots \\ \mathbf{K}^{N_t} \end{bmatrix}, \mathbf{b} = \begin{bmatrix} \mathbf{b}^1 \\ \vdots \\ \mathbf{b}^{N_t} \end{bmatrix}. \tag{2.6}$$

2.1.3. Noise Model

Noise on the image has multiple sources and each noise has different statistical properties. For example, noise from the sensor is well-modeled as Gaussian noise. Shot noise from quantum fluctuation follows Poisson statistics, and the quantization error noise has uniform distribution. Having the right noise model is important for the image reconstruction because the likelihood function, which corresponds to the data fidelity measure, is derived from statistics of the noise. In most imaging system, the most dominant noise models are Gaussian and Poisson noise models. We also consider these two models for MFM.

2.1.3.1. Gaussian Noise Model. Gaussian noise is the most common noise model in signal processing due to the generality and simplicity of Gaussian distribution. It is additive and signal-independent. The image acquisition model for i-th pixel with Gaussian noise model is as

$$\mathbf{g}_i = \mathbf{K}\mathbf{f}_i + \mathbf{b}_i + \epsilon \tag{2.7}$$

where ϵ follows the probability distribution as

$$p(\epsilon) = \frac{1}{\sqrt{2\pi}\beta^{-1/2}} \exp\Big\{ -\frac{\beta}{2}\epsilon^2 \Big\}, \tag{2.8}$$

where β is the precision or the inverse variance of the Guassian statistics.

For the whole image, the acquisition model will be written as

$$\mathbf{g} = \mathbf{K}\mathbf{f} + \mathbf{b} + \boldsymbol{\epsilon} \tag{2.9}$$

where $\boldsymbol{\epsilon}$ follows the probability distribution as

$$p(\boldsymbol{\epsilon}|\beta) = \frac{\beta^{M/2}}{(2\pi)^{M/2}} \exp\Big\{ -\frac{\beta}{2}\|\boldsymbol{\epsilon}\|^2 \Big\}, \tag{2.10}$$

assuming the i.i.d. Gaussian distribution. It can be expressed as $\boldsymbol{\epsilon} \sim \mathcal{N}(0, \beta^{-1}\mathbf{I})$ for simplicity.

2.1.3.2. Poisson Noise Model. Poisson noise is from photon counting/arrival process from the photon detector and it appears dominant in low-level-light imaging systems. Unlike Gaussian noise, Poisson noise is not additive and signal-dependent. The image acquisition model with Poisson noise for the i-th pixel is expressed as

$$\mathbf{g}_i = \mathcal{P}(\mathbf{K}\mathbf{f}_i + \mathbf{b}_i), \tag{2.11}$$

with nonlinear Poisson noise operator $\mathcal{P}(\cdot)$, which follows the probability distribution as

$$p(\mathbf{g}_i|\mathbf{f}) = -\log p(\mathbf{g}|\mathbf{f}) \tag{2.12}$$

$$= \frac{\big[\mathbf{K}\mathbf{f} + \mathbf{b}\big]_i^{\mathbf{g}_i} \exp\big(-\big[\mathbf{K}\mathbf{f} + \mathbf{b}\big]_i\big)}{\mathbf{g}_i!}, \tag{2.13}$$

where $[\cdot]_i$ indicates the i-th pixel.

For the whole image, the acquisition model with Poisson noise will be written as

$$\mathbf{g} = \mathcal{P}(\mathbf{Kf} + \mathbf{b}), \tag{2.14}$$

with the probability distribution as

$$p(\mathbf{g}|\mathbf{f}) = \prod_{i=1}^{M} \frac{\left[\mathbf{Kf} + \mathbf{b}\right]_i^{\mathbf{g}_i} \exp\left(-\left[\mathbf{Kf} + \mathbf{b}\right]_i\right)}{\mathbf{g}_i!}. \tag{2.15}$$

where M denotes the number of pixels in $\mathbf{g}$.

2.2. Acquisition Models and 3D Image Reconstruction for MFM

In this section, we introduce two MFM acquisition models with two different noise models from Section 2.1.3, and describe image reconstruction methods based on the acquisition models. For each acquisition model, we can formulate the optimization problem for image reconstruction, whose objective function consists of the negative log-likelihood function as data fidelity term and the 3D total variation (TV) term as regularization with non-negativity constraint. The problem formulation described here will be the foundation of the advanced methods in Chapters 3, 4, and 5.

2.2.1. Acquisition model based on Gaussian noise

Assuming Gaussian noise, the acquisition model for j-th MFM tile is expressed as

$$\mathbf{g}^j = \mathbf{K}^j\mathbf{f} + \mathbf{b}^j + \boldsymbol{\epsilon}^j \tag{2.16}$$

where $j = 1, \ldots, N_t$, with the probability distribution as

$$p(\boldsymbol{\epsilon}^j|\beta^j) = \frac{{\beta^j}^{M_t/2}}{(2\pi)^{M_t/2}} \exp\Big\{ -\frac{\beta^j}{2}\|\boldsymbol{\epsilon}^j\|^2 \Big\}. \tag{2.17}$$

Thus, the likelihood for the whole MFM image is described as

$$p(\mathbf{g}|\mathbf{f}, \boldsymbol{\beta}) = \prod_{j=1}^{N_t} \frac{{\beta^j}^{M_t/2}}{(2\pi)^{M_t/2}} \exp\Big\{ -\frac{\beta^j}{2}\|\mathbf{g}^j - \mathbf{K}^j\mathbf{f} - \mathbf{b}^j\| \Big\}. \tag{2.18}$$

The image reconstruction problem can be formulated as minimization of the sum of the negative log-likelihood and TV regularizer as follows:

$$\hat{\mathbf{f}} = \arg\min_{\mathbf{f}\geq\mathbf{0}} \frac{1}{2}\sum_{j=1}^{N_t} \beta^j\|\mathbf{g}^j - \mathbf{K}^j\mathbf{f} - \mathbf{b}^j\|^2 + \alpha \mathrm{TV}(\mathbf{f}), \tag{2.19}$$

where $\mathrm{TV}(\mathbf{f})$ is defined as

$$\mathrm{TV}(\mathbf{f}) = \sum_{i=1}^{N} \sqrt{(\Delta_i^x\mathbf{f})^2 + (\Delta_i^y\mathbf{f})^2 + (\Delta_i^z\mathbf{f})^2} \tag{2.20}$$

where i is the index for voxels, and Δ^x, Δ^y, and Δ^z denote the first difference operator along the x, y, and z directions, respectively.

Assuming $\mathbf{b}^j$ is known, Eq. 2.19 can be re-written as

$$\hat{\mathbf{f}} = \arg\min_{\mathbf{f}\geq\mathbf{0}} \frac{1}{2}\sum_{j=1}^{N_t} \beta^j\|\mathbf{g}'^j - \mathbf{K}^j\mathbf{f}\|^2 + \alpha \mathrm{TV}(\mathbf{f}). \tag{2.21}$$

where $\mathbf{g}'^j = \mathbf{g}^j - \mathbf{b}^j$. This MFM model and the image reconstruction method will be used in Chapter 4.

As a special case, we can assume the same level of Gaussian noise for all the tiles ($\beta^j = \beta$ for all j). Then the acquisition model of MFM becomes as

$$\mathbf{g} = \mathbf{K}\mathbf{f} + \mathbf{b} + \boldsymbol{\epsilon} \tag{2.22}$$

where $\boldsymbol{\epsilon} \sim N(\mathbf{0}, \beta^{-1}\mathbf{I}_M)$.

Similarly, the image reconstruction problem is formulated as follows:

$$\hat{\mathbf{f}} = \arg\min_{\mathbf{f}\geq\mathbf{0}} \frac{\beta}{2} \sum_{j=1}^{N_t} \|\mathbf{g}'^j - \mathbf{K}^j\mathbf{f}\|^2 + \alpha \mathrm{TV}(\mathbf{f}) \tag{2.23}$$

$$= \arg\min_{\mathbf{f}\geq\mathbf{0}} \frac{1}{2} \sum_{j=1}^{N_t} \|\mathbf{g}'^j - \mathbf{K}^j\mathbf{f}\|^2 + \lambda \mathrm{TV}(\mathbf{f}), \tag{2.24}$$

$\lambda = \alpha/\beta$ is the regularization parameter.

Assuming $\mathbf{b}$ is known, Eq. 2.24 can be re-written as

$$\hat{\mathbf{f}} = \arg\min_{\mathbf{f}\geq 0} \ \frac{1}{2}\|\mathbf{g}' - \mathbf{K}\mathbf{f}\|_2^2 + \lambda \mathrm{TV}(\mathbf{f}), \tag{2.25}$$

where $\mathbf{g}' = \mathbf{g} - \mathbf{b}$. This MFM model and the image reconstruction formulation will be used in Chapter 3.

2.2.2. Acquisition model based on Poisson noise

Assuming Poisson noise, the acquisition model for MFM becomes as

$$\mathbf{g} = \mathcal{P}(\mathbf{K}\mathbf{f} + \mathbf{b}). \tag{2.26}$$

where $\mathcal{P}(\cdot)$ is Poisson noise operator.

From this acquisition model, the image reconstruction problem can be formulated as follows:

$$\hat{\mathbf{f}} = \arg\min_{\mathbf{f}\geq\mathbf{0}} \; -\log p(\mathbf{g}|\mathbf{f}) + \lambda \mathrm{TV}(\mathbf{f}) \tag{2.27}$$

$$= \arg\min_{\mathbf{f}\geq\mathbf{0}} \mathcal{L}(\mathbf{f}) + \lambda \mathrm{TV}(\mathbf{f}), \tag{2.28}$$

where $\mathcal{L}(\mathbf{f})$ denotes the negative log-likelihood from Poisson statistics ignoring the constant factors, defined as

$$\mathcal{L}(\mathbf{f}) = \sum_{i=1}^{M} \Big\{ \big[\mathbf{K}\mathbf{f} + \mathbf{b}\big]_i - \mathbf{g}_i \log \big[\mathbf{K}\mathbf{f} + \mathbf{b}\big]_i \Big\}, \tag{2.29}$$

where i is the pixel index. This acquisition model and the image reconstruction formulation will be used in Chapter 5.

2.3. Conclusion

In this chapter we have reviewed the two different acquisition models for MFM based on two different noise models, and formulate the corresponding image reconstruction methods. The acquisition models and the reconstruction methods will be bases for the advanced methods in Chapter 3, 4, and 5.

CHAPTER 3

Three-Dimensional Image Reconstruction from Multi-Focus Microscope: Axial Super-Resolution and Multiple-Frame Processing

In this chapter, we present a multiple-frame (MF) three-dimensional (3D) image reconstruction algorithm for multi-focus microscope (MFM) images. Multi-focus microscope (MFM) provides a way to obtain 3D information by simultaneously capturing multiple focal planes. The naive method for MFM reconstruction is to stack the sub-images with alignment. However, the resolution in the z-axis in this method is limited by the number of acquired focal planes. In this work we build on a recent reconstruction algorithm for MFM, using information from multiple frames to improve the reconstruction quality. We propose two multiple-frame MFM image reconstruction algorithms: batch and recursive approaches. In the batch approach, we take multiple MFM frames and jointly estimate the 3D image and the motion for each frame. In the recursive approach, we utilize the reconstructed image from the previous frame. Experimental results show that the proposed algorithms produce a sequence of 3D object reconstruction with high quality that enable reconstruction of dynamic extended objects.

3.1. Introduction

The conventional way to acquire a 3D image of the sample (i.e., the object) with a microscope is via sequential refocusing. Once a focal stack of the object is captured, and

given the point spread function (PSF) of the optical system, a 3D deconvolution is performed to reconstruct the 3D object. However, sequential refocusing has serious disadvantages. It is too slow to accurately capture the dynamics and the stage movement for refocusing can cause perturbation of the sample. To overcome these limitations, Abrahamsson *et al.* developed the multi-focus microscopy (MFM) to capture multiple focal planes as a single snapshot [14]. MFM uses a diffractive grating or diffractive optical element (DOE) to split the light from different focal planes into separate paths and forms an array of images on the camera.

Given a single MFM measurement, a 3D volume can be generated simply by stacking the sub-images with the alignment [14]. However, in this way, one can only reconstruct as many focal planes as the number of sub-images, and the z spacing between the slices is limited to the focal shift between two adjacent sub-images. Also, it will suffer from the out-of-focus blur. Huang *et al.* proposed a reconstruction method that uses a densely z-sampled 3D PSF comprised of these 2D depth-encoded MFM images [17]. This approach handles the out-of-focus blur and results in improved resolution in the z-axis for single frame MFM images.

Because MFM is able to capture video of dynamic scenes, we can make use of multiple frames to obtain a higher quality reconstruction. The same idea has been widely used in the super-resolution (SR) literature, where the motion between different frames is taken into account to complete sub-pixel information [41–44, 46, 47, 64, 65]. Tsai and Huang first proposed to use multiple images to obtain a high resolution (HR) image but only considered translational motion [64]. Farsiu *et al.* proposed a robust estimation method by using l_1 minimization and extended the motion model to the affine transformation [65]. He *et al.* modeled the degradation with a nonlinear function to represent motion with both rotation and translation [41]. Belekos *et al.* used the maximum a posteriori (MAP) framework for

video SR [42] and Babacan *et al.* proposed a variational Bayesian framework for multiple-frame SR [43]. Liu *et al.* proposed a MAP based video SR method that jointly estimates the HR image, blur, motion, and noise. They used an optical flow algorithm to estimate local motion [44]. Recent learning-based video SR methods also utilized an optical flow algorithm for motion estimation [46, 47].

All the methods described above were developed for 2D image SR. Here we extend multiple-frame (MF) image SR schemes to 3D space to obtain a higher resolution along the z-axis in MFM. We build on single frame MFM reconstruction approach in [17] and improve the reconstruction using multiple frames. We propose two approaches for MF reconstruction: the batch approach which exploits the multiple neighboring frames, and the recursive approach which uses the 3D reconstruction obtained for the previous frames. The proposed methods can also be applied to a broader range of inverse problems with multiple observations, such as, 3D image reconstruction from conventional microscopy or uncalibrated tomography [56].

The chapter is organized as follows. Single frame reconstruction from [17] is summarized in Section 3.2 using notation consistent with the rest of the paper. The MF reconstructions algorithms are introduced in Section 3.3. Experimental results and discussion are provided in Section 3.4 and we conclude our paper in Section 3.5.

3.2. Single-Frame MFM Reconstruction

3.2.1. Acquisition Model

Fig. 1.1 (a) illustrates our MFM system. The DOE splits the light from different focal planes, forming $K \times K$ tiles as shown in Fig. 1.1 (b). Each tile corresponds with the image obtained for a different focal plane. Because it is a linear spatially invariant system, its whole optical

system can be characterized by its PSF. The 3D PSF is estimated by sequential refocusing with a fixed fluorescent bead.

Let $f \in \mathbb{R}^{N_x \times N_y \times N_z}$, $g \in \mathbb{R}^{M_x \times M_y}$, and $h \in \mathbb{R}^{M_x \times M_y \times M_z}$ denote a 3D object, its MFM measurement, and the 3D PSF of the MFM, respectively. The acquisition process of MFM can be modeled as the extraction of one plane (suppose $z = 0$) after 3D convolution of f and h, and equivalently as the sum of 2D convolutions of $f(x, y; -z)$ and $h(x, y; z)$, plus additive Gaussian noise $\epsilon \in \mathbb{R}^{M_x \times M_y}$ as

$$\begin{aligned} g(x,y) &= h(x,y,z) *_{3D} f(x,y,z)\big|_{z=0} + \epsilon(x,y) \\ &= \sum_{z=-\lfloor N_z/2 \rfloor}^{\lfloor N_z/2 \rfloor} h(x,y;z) *_{2D} f(x,y;-z) + \epsilon(x,y), \end{aligned} \tag{3.1}$$

where $*_{3D}$ and $*_{2D}$ denote the 3D convolution and the 2D convolution operators, respectively. Eq. 3.1 can also be expressed in matrix-vector notation as

$$\mathbf{g} = \mathbf{H}\mathbf{f} + \boldsymbol{\epsilon} \tag{3.2}$$

where $\mathbf{f} \in \mathbb{R}^{N_x N_y N_z \times 1}$, $\mathbf{g} \in \mathbb{R}^{M_x M_y \times 1}$, and $\boldsymbol{\epsilon} \in \mathbb{R}^{M_x M_y \times 1}$ are vectorized f, g, and ϵ, respectively, and $\mathbf{H} \in \mathbb{R}^{M_x M_y \times N_x N_y N_z}$ denotes the MFM PSF matrix.

3.2.2. Single-Frame Reconstruction (SFR)

To reconstruct a 3D object, $\mathbf{f}$, when provided a MFM image, $\mathbf{g}$, and the MFM PSF matrix, $\mathbf{H}$, we can formulate the inverse problem as in [17]. Assuming Gaussian noise, a regularized least squares method to reconstruct $\mathbf{f}$ is formulated as follows:

$$\hat{\mathbf{f}} = \arg\min_{\mathbf{f}} \ \|\mathbf{g} - \mathbf{H}\mathbf{f}\|_2^2 + \lambda\Phi(\mathbf{f}), \quad \text{subject to} \ \ \mathbf{f} \geq 0 \tag{3.3}$$

where λ is a regularizing parameter, and $\Phi(\cdot)$ is a regularizer function. In this paper we chose the 3D total variation (TV) regularizer because it encourages piecewise smoothness of the signal by enforcing sparsity in the gradient domain. It is suitable for extended objects, such as bacteria that we want to reconstruct. The TV regularizer for a 3D object, $\mathbf{f}$, is defined as

$$\Phi(\mathbf{f}) = \sum_i \sqrt{(\Delta_i^x \mathbf{f})^2 + (\Delta_i^y \mathbf{f})^2 + (\Delta_i^z \mathbf{f})^2} \tag{3.4}$$

where i is a voxel index and $\Delta_i^x \mathbf{f}$, $\Delta_i^y \mathbf{f}$, and $\Delta_i^z \mathbf{f}$ denote first-order difference operators in the x, y, and z directions, respectively. Eq. 3.3 is solved by employing the two-step iterative shrinkage/thresholding (TwIST) algorithm [**24**] with the projected gradient scheme for the non-negativity constraint. Note that the choice of the regularizing parameter, λ, is important for the quality of reconstruction. If it is too large or too small, it converges to a poor solution. In our experiments, we performed an exhaustive search for this parameter to obtain an optimal reconstruction.

3.3. Multiple-frame MFM Reconstruction

Given a sequence of MFM images, we can use multiple MFM images to achieve a higher quality 3D reconstruction. We first describe two acquisition models for MF MFM images and introduce two approaches for the MF MFM reconstruction. Here we assume that there is a single rigid object in the sample space and model the motion as a rigid transformation that only includes 3D translation and 3D rotation.

3.3.1. Acquisition Model

The first model for the acquisition process describes a mapping from a 3D object at k-th frame, $\mathbf{f}_k \in R^{N_x N_y N_z \times 1}$, to the captured MFM image, $\mathbf{g}_k \in R^{M_x M_y \times 1}$. Let $\mathbf{H} \in R^{M_x M_y \times N_x N_y N_z}$

and $\boldsymbol{\epsilon}_k \in R^{M_x M_y \times 1}$ denote the MFM PSF matrix and the noise in k-th frame respectively. Then, the acquisition process is modeled as

$$\mathbf{g}_k = \mathbf{H}\mathbf{f}_k + \boldsymbol{\epsilon}_k. \tag{3.5}$$

which is the same form as Eq. 3.2 in Section 3.2 for the SFR algorithm. The acquisition model in Eq. 3.5 can be extended by considering the relationship between frames as

$$\mathbf{g}_k = \mathbf{H}\mathbf{M}_{l,k}(\boldsymbol{\alpha}_{l,k})\mathbf{f}_l + \boldsymbol{\epsilon}_{l,k} \tag{3.6}$$

where $\boldsymbol{\alpha}_{l,k}$ and $\mathbf{M}_{l,k}(\boldsymbol{\alpha}_{l,k})$ denote the motion parameters for the 3D object from l-th frame to k-th frame and the warping matrix corresponding to $\boldsymbol{\alpha}_{l,k}$, and $\boldsymbol{\epsilon}_{l,k}$ is a Gaussian noise term. $\boldsymbol{\alpha}_{l,k}$ consists of three parameters for 3D translation and three parameters for 3D rotation since rigid transformation is assumed for the motion. Note that, in this model, every MFM measurement originates from the reference object, $\mathbf{f}_l$, through a geometric transformation and MFM imaging with noise.

3.3.2. Batch Approach

Based on the acquisition model in Eq. 3.6, we suggest to use a batch of MFM measurements to reconstruct one frame, $\mathbf{f}_l$, and we call it the batch approach for MF reconstruction. We formulate the optimization problem to estimate $\mathbf{f}_l$ for the batch approach as

$$\begin{aligned}\{\hat{\mathbf{f}}_l, \hat{\boldsymbol{\alpha}}_{l,k}\} = \arg\min_{\mathbf{f_l}\geq 0, \boldsymbol{\alpha}_{l,k}} & \sum_{k=l-m}^{l+m} \|\mathbf{g}_k - \mathbf{H}\mathbf{M}_{l,k}(\boldsymbol{\alpha}_{l,k})\mathbf{f}_l\|_2^2 \\ & + \lambda\Phi(\mathbf{f}_l) + \omega \sum_{k=l-m}^{l+m} \|\boldsymbol{\alpha}_{l,k}\|_2^2\end{aligned} \tag{3.7}$$

where m is a positive number that determines the number of neighboring frames used in the reconstruction, and ω is the regularizing parameter for $\boldsymbol{\alpha}_{l,k}$.

The first term in Eq. 3.7 is the data fidelity term based on the acquisition model in Eq. 3.6. In principle, the whole sequence of MFM image can be used for the reconstruction of $\mathbf{f}_l$, but it is computationally demanding and frames far in time can possibly degrade the reconstruction quality due to large mis-registration error. Therefore, we use a batch of frames around $\mathbf{f}_l$. The last term in Eq. 3.7 is a regularizer for the motion parameters. Since the motion between two frames is small for a short period of time, we chose the l_2 norm to enforce small values for $\boldsymbol{\alpha}_{l,k}$. ω is chosen empirically and is set to small values.

The alternating descent scheme is applied to solve the multi-variable non-convex problem of Eq. 3.7. We solve for $\mathbf{f}_l$ while fixing $\boldsymbol{\alpha}_{l,k}$ first, and then solve for the motion parameters set by set while fixing $\mathbf{f}_l$ and the other motion parameter sets. Note that in this approach we have $2m$ sets of motion parameters to estimate ($\boldsymbol{\alpha}_{l,k}$ for $k = l-m, \cdots, -1, 1, \cdots, l+m$). The alternation is repeated until it converges.

3.3.3. Recursive Approach

Based on Eq. 3.5, each frame can be reconstructed by the SFR method as described in Section 3.2. For $k = 1, \cdots, S$, it can be expressed as

$$\hat{\mathbf{f}}_k = \arg\min_{\mathbf{f_k} \geq 0} \ \|\mathbf{g}_k - \mathbf{H}\mathbf{f}_k\|_2^2 + \lambda\Phi(\mathbf{f}_k). \tag{3.8}$$

Here we can exploit the information from previous frames in a recursive manner by using the 3D reconstruction data from the previous frame. Since we assume the 3D object is rigid, we add a constraint that the reconstruction at k-th frame should be the same as the

reconstruction at $(k-1)$-th frame under a rigid transformation as

$$\begin{aligned}\{\hat{\mathbf{f}}_k, \hat{\boldsymbol{\alpha}}_{k-1,k}\} = \arg \min_{\mathbf{f}_k \geq 0, \boldsymbol{\alpha}_{k-1,k}} & \|\mathbf{g}_k - \mathbf{H}\mathbf{f}_k\|_2^2 + \lambda\Phi(\mathbf{f}_k) \\ & + \eta\|\mathbf{f}_k - \mathbf{M}_{k-1,k}(\boldsymbol{\alpha}_{k-1,k})\mathbf{f}_{k-1}\|_2^2,\end{aligned} \tag{3.9}$$

where λ and η are the regularizing parameters for each regularizer term, which can be chosen by exhaustive search.

Eq. 3.9 is a non-convex optimization problem with two unknown variables, $\mathbf{f}_k$ and $\boldsymbol{\alpha}_{k-1,k}$. Similarly to the batch approach, we use the alternating descent algorithm to solve for each variable in an alternating fashion until convergence.

3.4. Experimental Results

In this section, we evaluate the performance of single-frame reconstruction (SFR), multiple-frame batch approach (MF batch) and multiple-frame recursive approach (MF recursive), on both synthetic and real datasets.

3.4.1. Synthetic Experiment

For the synthetic experiment, a 3D image of a double-lobe bacterium was acquired by using confocal microscopy. The 3D image is scaled, cropped, and located in the center of the space of $50 \times 50 \times 51$. 30 frames were generated by sequentially adding to each new frame a rotation of 5° along the y-axis and 2° along the z-axis, and a 3D random shift generated by multivariate Gaussian with mean 0 and covariance matrix $\mathbf{I}_{3\times3}$. Fig. 3.2 (a) and Fig. 3.3 (a) show the simulated 3D object at different frames. To visualize the 3D image more effectively, we used a colormap such that blue and red colors indicate the lowest and the highest intensity respectively, and display three projections onto the xy, yz, and zx planes as well. The object

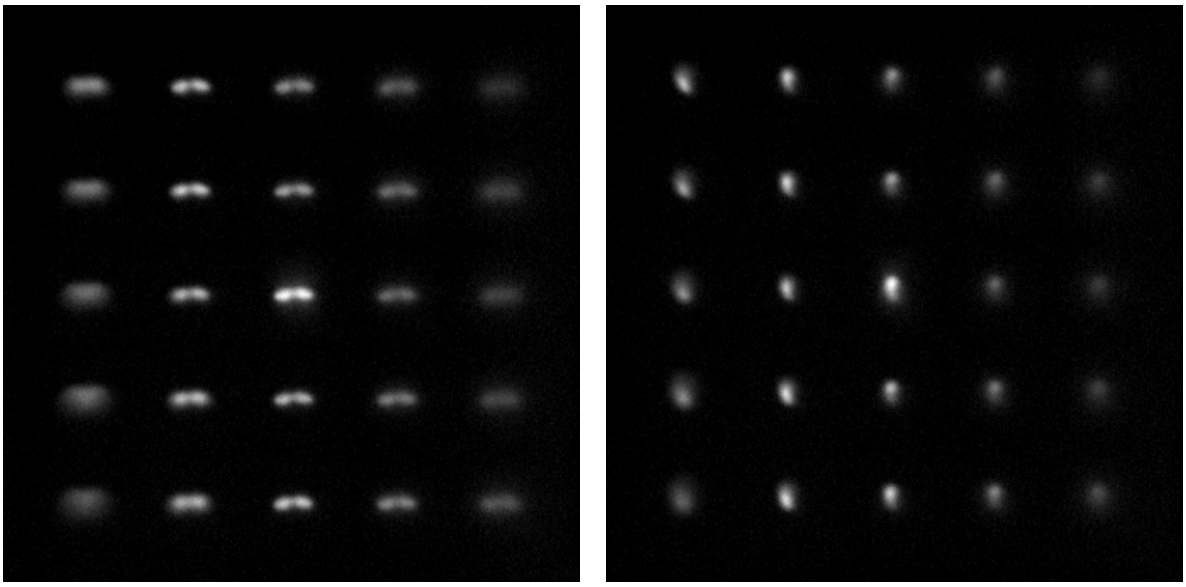

(a) (b)

Figure 3.1. Simulated MFM images with a bacterium-like object with Gaussian noise ($\sigma_n = 0.02$). (a) The object lies in the xy plane at frame 3, and (b) stands along the z-axis at frame 21.

lies along xy plane at frame 3, and stands along the z direction at frame 21. The obtained frames are used as ground truth in our experiments.

To simulate the MFM acquisition model, each frame is degraded according to Eq. 3.1, with a scaled version of the measured PSF. We generated observations for two different standard deviation values of the Gaussian noise $\sigma_n = 0.01$ and $\sigma_n = 0.02$. Fig. 3.1 shows the simulated MFM images at different frames with $\sigma_n = 0.02$.

Figures 3.2 and 3.3 show the original and the reconstructed 3D images, with noise $\sigma_n = 0.02$, at frames 3 and 21 out of 30 frames. For both frames, we observe that the reconstructions become elongated along the z axis, which is caused by the missing cone problem in microscopy imaging [**66**, **67**]. Nevertheless, we can observe the reconstructions are very similar to the ground truth, especially along the xy plane. The quality between reconstruction methods is distinguished at frame 21 where SFR fails reconstructing the double

lobe. However, MF reconstruction approaches reconstruct the two lobes as can be clearly seen in the projections. The reconstruction of MF batch is better than SFR but it is visually noisier than MF recursive.

Table 3.1 summarizes the overall performance of the MFM reconstruction algorithms in average peak signal-to-noise ratio (PSNR) and structural similarity index (SSIM). The MF reconstruction methods improve the performance, and MF recursive results in the most significant improvement in average. These numbers match the visual quality from Figs. 3.2 and 3.3. As the more neighboring frames are used, MF batch results in better performance but with more intense computation.

The plots in Fig. 3.4 show the PSNR values for all the frames. They tell a few things about the reconstruction methods. First, the MF approaches give better reconstruction compared to the SFR method. The PSNRs of the MF approaches are higher than those of the SFR method at most of the frames. Second, MF batch follows the trend of the SFR, but produces higher quality reconstruction than SFR by using multiple observation. The more observation, the better reconstruction. Third, the performance of MF recursive depends on the previous reconstruction. The reconstruction quality does not change as abruptly as the other methods frame by frame. Because it encourages the reconstruction to be the same

Table 3.1. Performance and running time of MFM image reconstruction algorithms. Average PSNR, SSIM, and running time are calculated over 26 frames. Running time is recorded in the unit of minute.

	$\sigma_n = 0.01$			$\sigma_n = 0.02$		
Methods	PSNR	SSIM	Time	PSNR	SSIM	Time
SFR	38.30	0.9868	1.12	36.47	0.9786	0.83
MF batch, $m = 1$	39.04	0.9899	19.97	37.31	0.9786	36.03
MF batch, $m = 2$	40.05	0.9919	49.58	38.17	0.9814	123.30
MF recursive	40.20	0.9897	4.36	39.57	0.9842	4.37

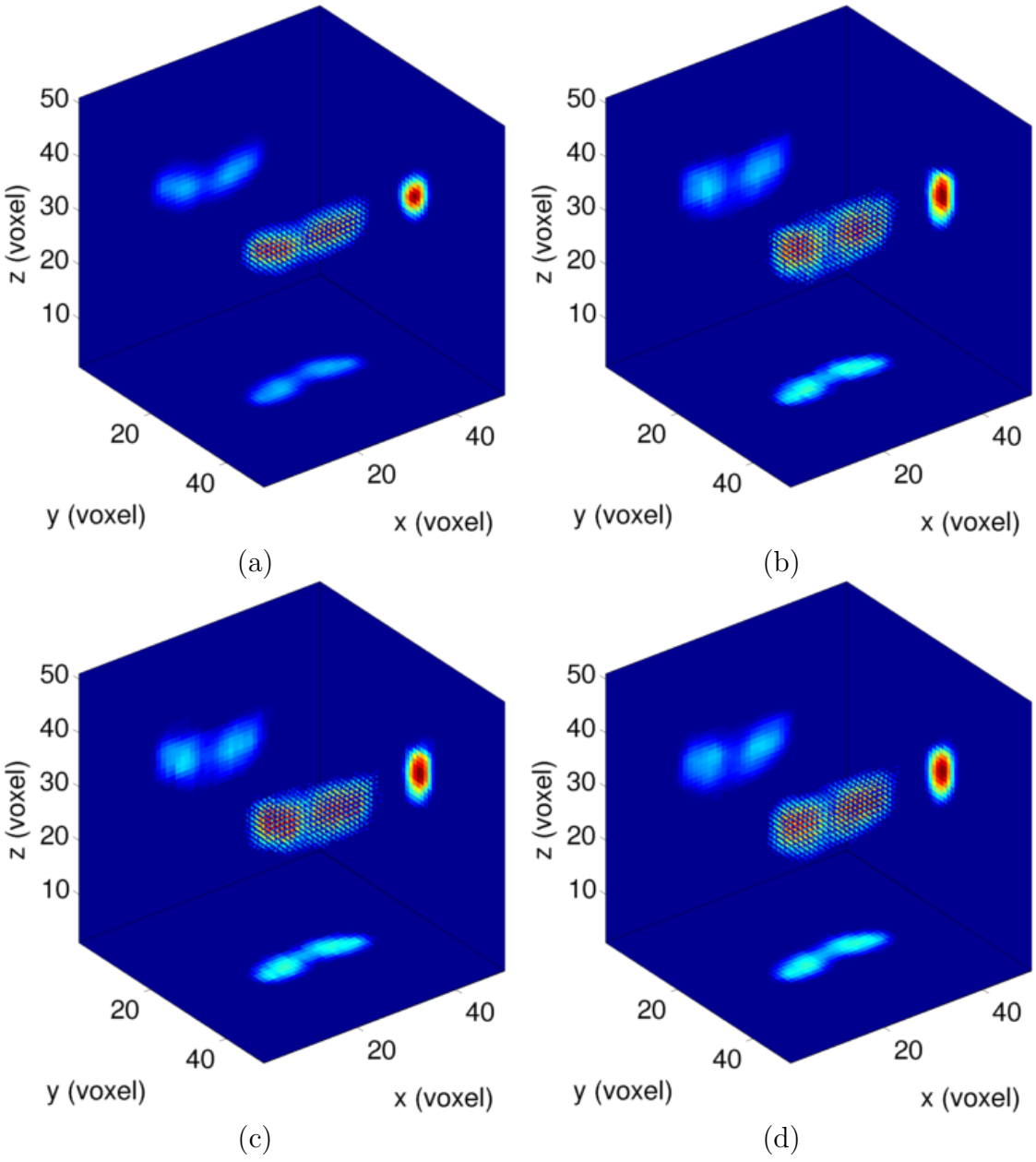

Figure 3.2. Reconstructed 3D images at frame 3 with $\sigma_n = 0.02$. (a) Ground truth, (b) SFR, PSNR:37.24, SSIM:0.9868, (c) MF batch ($m = 2$), PSNR:38.13, SSIM:0.9887, (d) MF recursive, PSNR:37.79, SSIM:0.9877.

as previous reconstruction, it tries to keep the 3D shape. In this way, it produces more consistent 3D reconstruction over the sequence.

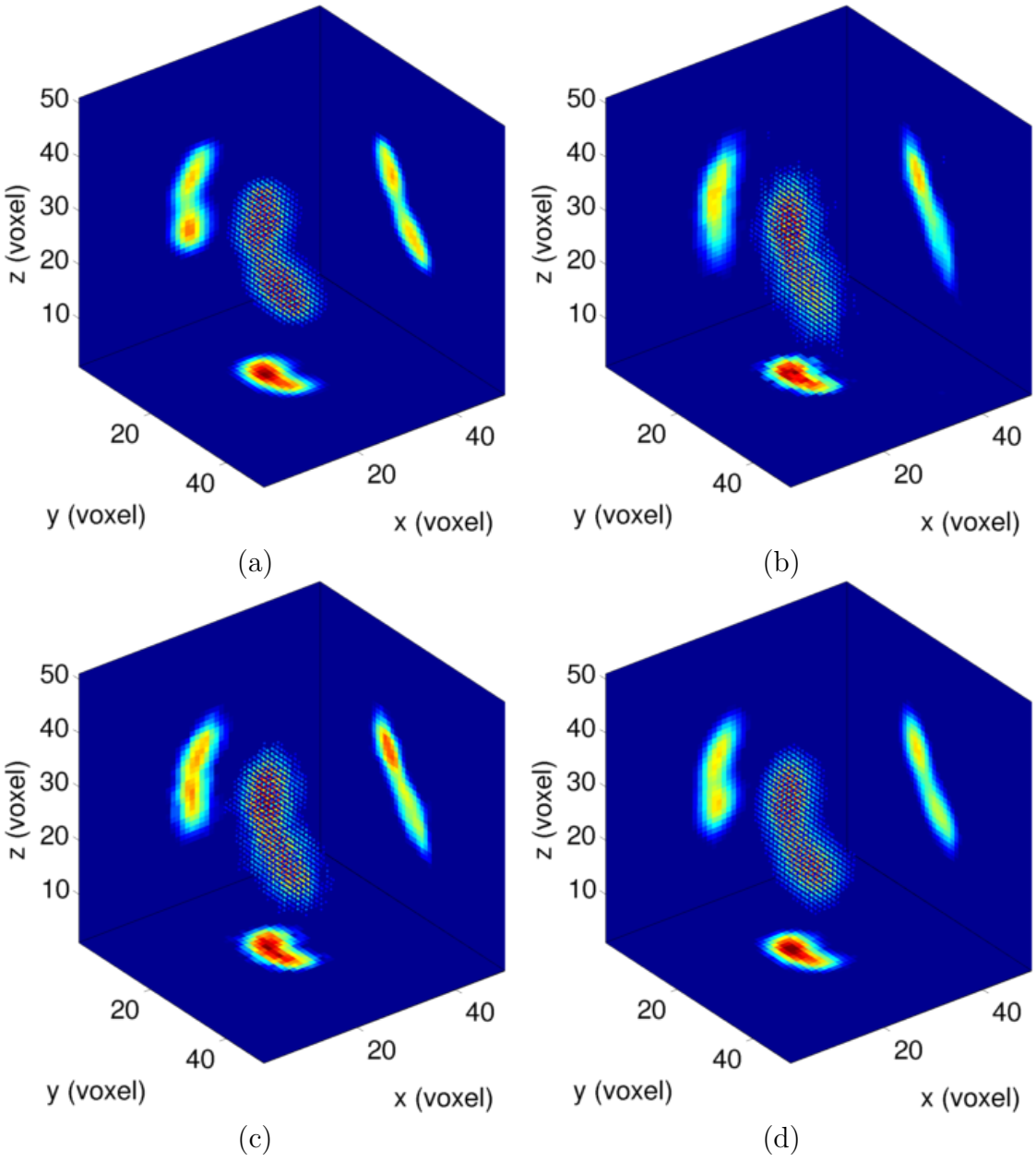

Figure 3.3. Reconstructed 3D images at frame 21 with $\sigma_n = 0.02$. (a) Ground truth, (b) SFR, PSNR:36.39, SSIM:0.9747, (c) MF batch ($m = 2$), PSNR:38.80, SSIM:0.9835, and (d) MF recursive, PSNR:40.97, SSIM:0.9866.

Table 3.1 also shows the average running time of the reconstruction in the unit of minute. The MF reconstruction algorithms takes more time since they have more data to process

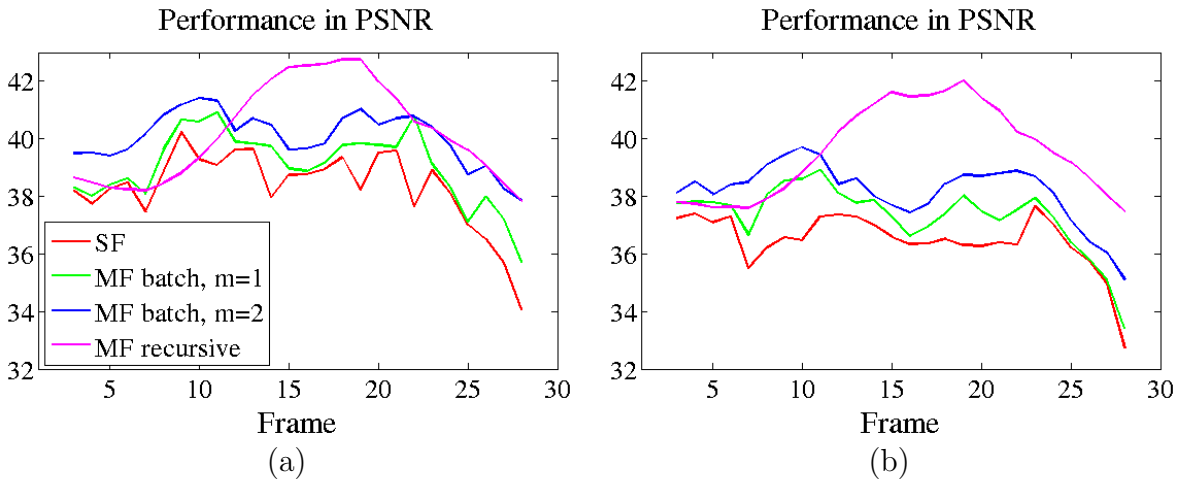

Figure 3.4. PSNRs for each frame, (a) $\sigma_n = 0.01$, (b) $\sigma_n = 0.02$.

and have to estimate the motion between frames in addition to the 3D image in an iterative manner. The batch approach uses $(2m + 1)$ times as much data as SFR and also it has $2m$ sets of the motion parameters to estimate. For the recursive approach, it adds as much data as the reconstruction object for image estimation, and has one set of motion parameters to estimate. Note that the time in the table for SFR does not include the time for the exhaustive search for an optimal λ.

3.4.2. Real Experiment

A tumbling bacterium was captured with our MFM system [**17**]. The frame rate was about 30 fps and the illumination time was 20 ms per frame. The effective pixel size is $98nm \times 98nm$ and the pixel resolution of the camera is 1024×1024. Fig. 3.5 (a) shows an MFM image at frame 22.

For real data, the reconstruction results are evaluated by visual quality. Fig. 3.5 shows the MFM measurement and the reconstruction results with the three algorithms: SFR, MF batch, and MF recursive at frame 22. While all three methods reconstruct the 3D image of

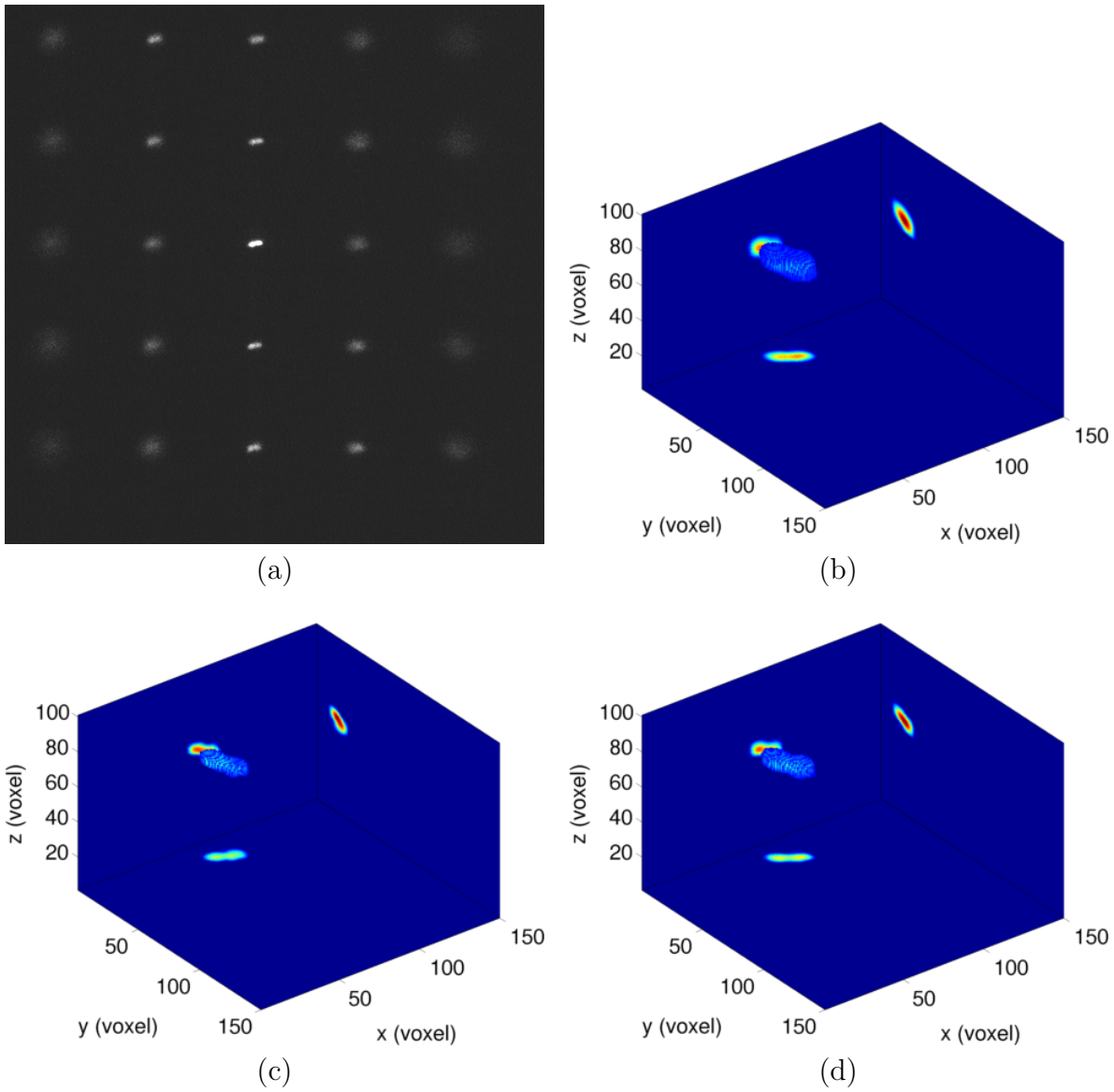

Figure 3.5. Reconstructed 3D images from the real data at frame 22 (a) MFM measurement, (b) SFR, (c) MF batch approach, and (d) MF recursive approach.

the bacterium that conforms to the size and the shape of the bacteria that we already know, the MF reconstruction methods produce sharper 3D images than SFR. Also, SFR becomes more sensitive to the choice of λ for the real data so we tried up to 15 values of λ to obtain reasonable reconstruction quality.

3.5. Conclusion

We have developed two multiple-frame (MF) 3D image reconstruction algorithms for MFM: MF batch, and MF recursive. Our methods outperform the single-frame reconstruction, achieving higher quality image reconstruction in axial super-resolution. MF batch uses a batch of neighboring MFM images for reconstruction while MF recursive utilizes the reconstructed 3D image from the previous frame. Experimental results with both synthetic and real data show the effectiveness of our methods.

CHAPTER 4

Bayesian Approach for Automatic Joint Parameter Estimation in Three-Dimensional Image Reconstruction from Multi-Focus Microscope

In this chapter, we present a Bayesian approach for 3D image reconstruction of an extended object imaged with multi-focus microscopy (MFM). MFM simultaneously captures multiple sub-images of different focal planes to provide 3D information of the sample. The naive method to reconstruct the object is to stack the sub-images along the z-axis, but the result suffers from poor resolution in the z-axis. The maximum a posteriori framework provides a way to reconstruct a 3D image according to its observation model and prior knowledge. It jointly estimates the 3D image and the model parameters. Experimental results with synthetic and real experimental data show that it enables the high-quality 3D reconstruction of an extended object from MFM.

4.1. Introduction

Multi-focus microscopy (MFM) was developed for fast acquisition of three-dimensional (3D) information [14]. In addition to the conventional microscopy setup, MFM includes a diffractive optical element (DOE), which splits the light from different focal planes into different positions on a camera (see Fig. 1.1 (a)). A captured MFM image includes $K \times K$ sub-images (or tiles) of a focal stack as shown in Fig. 1.1 (b). By capturing a stack of N_t

focal planes with a single shot, MFM enables the capture of a dynamic scene in biological samples.

In [14], Abrahamsson *et al.* showed that MFM can be used for imaging movement of cells and tracking a single molecule. However, they do not propose an algorithm to reconstruct the original 3D object from an MFM measurement. Instead MFM sub-images are stacked and aligned to get the 3D volume. With this scheme, one can only obtain as many focal planes as the number of sub-images, and the z spacing of the reconstructed image is limited to the focal shift between two adjacent sub-images. Also, this approach suffers from severe out-of-focus blur, which is a common issue for wide-field microscopy [66, 67].

In order to overcome these limitations, Huang *et al.* [17] proposed a method to reconstruct the 3D volume from the measured MFM images. To deal with the ill-posedness of the problem, they developed an optimization approach using sparsity (ℓ_1) and total variation (TV) regularizers. Yoo *et al.* [68] proposed an improved approach to reconstruct the 3D volume from a sequence of frames of the scene. Both methods achieved super-resolution in the z-axis for its 3D image reconstruction, increasing the number of the xy slices from 25 to 101.

The performance of the methods proposed in [17, 68] heavily depends on regularization parameters, which must be selected through an exhaustive search. The use of the Bayesian paradigm can help to mitigate this problem by automatically estimating all the unknowns of the problem from the data [69, 70]. Some examples of its applications in image processing are image restoration [71], blind image deconvolution [29], image and video super-resolution [43, 44] or light field acquisition [72].

In this work, we develop a Bayesian approach to the problem of 3D object reconstruction from MFM images. The MFM acquisition system is modeled by a likelihood function,

which takes into account two different noise schemes: (1) the same noise for all the tiles, and (2) different noise for each tile. Then we use a prior model based on the TV norm, following [17, 68]. The reconstructed 3D object as well as the parameters of the model are estimated using maximum a posteriori (MAP) inference.

The two-dimensional (2D) TV regularizer was introduced in [35] and it has been widely used in image reconstruction to enforce piece-wise smoothness on the reconstructed images (see [72, 73]). In addition to [17, 68], the 3D TV regularizer has been used in [74] in a tomography problem. However, to the best of our knowledge, a method for estimating the regularization parameter for the 3D TV function has not been reported in the literature. The Bayesian approach we develop allows extension of the methodology introduced in [73] to estimate the TV prior parameter in the 3D case.

In summary, the novelties of our work are: (1) a Bayesian modeling of the problem of 3D reconstruction from an MFM image, (2) a new noise model that allows different noise levels for each MFM sub-image, and (3) automatic estimation of all the noise variances as well as the parameter of the 3D TV prior.

The rest of this chapter is organized as follows. The Bayesian modeling is described in Section 4.2. MAP estimation based on the modeling is explained in Section 4.3. Experimental results and discussion are provided in Section 4.4 and we conclude the chapter in Section 4.5.

4.2. Bayesian modeling

The image acquisition process in MFM microscopy can be modeled as follows:

$$\mathbf{g}^j = \mathbf{D}\mathbf{H}^j\mathbf{f} + \boldsymbol{\epsilon}^j, \quad j = 1, \ldots, N_t. \tag{4.1}$$

In the j-th tile, we acquire a sub-image $\mathbf{g}^j \in \mathbb{R}^{M\times 1}$ written as a column vector. The 3D object to be recovered, also written as a column vector $\mathbf{f} \in \mathbb{R}^{N\times 1}$, is convolved with a 3D point spread function (PSF). In matrix notation, this 3D convolution is represented as $\mathbf{H}^j \in \mathbb{R}^{N\times N}$. Note that for each tile, we have a different PSF. This is due to chromatic aberrations introduced by the DOE, which produce different blur for each tile in addition to the different focus (see [14, 17] for details). Once the original 3D object is convolved with the PSF, we extract the central slice using the downsampling operator $\mathbf{D} \in \mathbb{R}^{M\times N}$ to be captured on a 2D sensor. The observation includes additive Gaussian noise $\boldsymbol{\epsilon}^j \in \mathbb{R}^{M\times 1}$.

In this work, we consider two cases of noise: (1) all the tiles have the same noise variance β^{-1}, and (2) each tile has different noise variance $\beta^{j^{-1}}$. Both cases lead to the following likelihood function

$$\mathrm{p}(\mathbf{g}|\mathbf{f},\boldsymbol{\beta}) = \prod_{i=1}^{N_t} \frac{\beta^{j\,M/2}}{(2\pi)^{M/2}} \exp\left\{-\frac{\beta^j}{2}\|\mathbf{g}^j - \mathbf{D}\mathbf{H}^j\mathbf{f}\|_2^2\right\}, \tag{4.2}$$

where $\mathbf{g} = [\mathbf{g}^{1^T}, \ldots, \mathbf{g}^{N_t{}^T}]^T$ and $\boldsymbol{\beta} = [\beta^1, \ldots, \beta^{N_t}]^T$. This observation model is related to the one introduced in [43], where the authors make use of the Bayesian framework to solve a super-resolution problem. However, there are differences between the two models. In our model, the downsampling matrix $\mathbf{D}$ extracts a 2D slice of a 3D volume, while in [43] the downsampling matrix reduces the size of an image in 2D. Also, an additional warping matrix is considered in [43] to register the observed images.

3D object reconstruction from MFM is a highly undetermined problem because we recover many more slices than the number of tiles in the MFM images. Use of priors mitigates this

problem, and we follow [17] and [68], and introduce a 3D TV prior

$$\mathrm{p}(\mathbf{f}|\alpha) = \frac{1}{Z_\alpha} \exp\left\{-\alpha \mathrm{TV}(\mathbf{f})\right\}, \tag{4.3}$$

where $\mathrm{TV}(\mathbf{f}) = \sum_{i=1}^{N} \sqrt{(\Delta_i^x \mathbf{f})^2 + (\Delta_i^y \mathbf{f})^2 + (\Delta_i^z \mathbf{f})^2}$ and Z_α is the partition function depending on the parameter α.

In order to estimate the parameters from the data, we need to know the partition function $Z_\alpha^{-1} = \int \exp\left\{-\alpha \mathrm{TV}(\mathbf{f})\right\} \mathrm{d}\mathbf{f}$, however, this integral is not tractable and Z_α cannot be explicitly calculated. In [58], the authors approximate the partition function of the 2D TV prior. Applying the same procedure as in [58] for the 3D case, we calculate the integral

$$\int_{\mathbb{R}^3} \exp\left\{-\alpha\sqrt{u^2+v^2+w^2}\right\} \mathrm{d}(u,v,w) = \frac{8\pi}{\alpha^3}, \tag{4.4}$$

which leads to the following approximation of the prior distribution

$$\mathrm{p}(\mathbf{f}|\alpha) \propto \alpha^{N/2} \exp\{-\alpha \mathrm{TV}(\mathbf{f})\}. \tag{4.5}$$

Note that the approximated partition function coincides with the 2D case used in [26, 58].

Finally, all of the available information about the problem is summarized in the joint distribution

$$\mathrm{p}(\mathbf{g}, \mathbf{f}, \boldsymbol{\beta}, \alpha) = \mathrm{p}(\mathbf{g}|\mathbf{f}, \boldsymbol{\beta}) \mathrm{p}(\mathbf{f}|\alpha) \mathrm{p}(\boldsymbol{\beta}) \mathrm{p}(\alpha), \tag{4.6}$$

where $\mathrm{p}(\boldsymbol{\beta})$ and $\mathrm{p}(\alpha)$ are non-informative flat priors.

4.3. Maximum a Posteriori (MAP) Inference

In order to estimate all the unknowns of the model, we estimate the maximum of the posterior distribution subject to all the voxels of the restored 3D object having non-negative

values, that is,

$$\{\hat{\mathbf{f}}, \hat{\boldsymbol{\beta}}, \hat{\alpha}\} = \arg \max_{\mathbf{f} \geq \mathbf{0}, \boldsymbol{\beta}, \alpha} \mathrm{p}(\mathbf{f}, \boldsymbol{\beta}, \alpha | \mathbf{g}) \tag{4.7}$$

$$= \arg \max_{\mathbf{f} \geq \mathbf{0}, \boldsymbol{\beta}, \alpha} \frac{\mathrm{p}(\mathbf{g}, \mathbf{f}, \boldsymbol{\beta}, \alpha)}{\mathrm{p}(\mathbf{g})} \tag{4.8}$$

$$= \arg \max_{\mathbf{f} \geq 0, \boldsymbol{\beta}, \alpha} \mathrm{p}(\mathbf{g}, \mathbf{f}, \boldsymbol{\beta}, \alpha) \tag{4.9}$$

$$= \arg \min_{\mathbf{f} \geq 0, \boldsymbol{\beta}, \alpha} - \log \mathrm{p}(\mathbf{g}, \mathbf{f}, \boldsymbol{\beta}, \alpha) \tag{4.10}$$

$$= \arg \min_{\mathbf{f} \geq 0, \boldsymbol{\beta}, \alpha} - \log \mathrm{p}(\mathbf{g} | \mathbf{f}, \boldsymbol{\beta}) \mathrm{p}(\mathbf{f} | \alpha) \mathrm{p}(\boldsymbol{\beta}) \mathrm{p}(\alpha). \tag{4.11}$$

$$\arg \min_{\mathbf{f} \geq 0, \boldsymbol{\beta}, \alpha} \sum_{j=1}^{N_t} \left\{ -\frac{M}{2} \log \beta^j + \frac{\beta^j}{2} \|\mathbf{g}^j - \mathbf{D}\mathbf{H}^j \mathbf{f}\|_2^2 \right\} - \frac{N}{2} \log \alpha + \alpha \mathrm{TV}(\mathbf{f}) \tag{4.12}$$

Since we cannot minimize Eq. (4.11) with respect to all of the unknowns at the same time, we alternate the estimations of the 3D object, $\mathbf{f}$, and the parameters, $\boldsymbol{\beta}$ and α, and iterate until the method converges.

Given the estimated parameters, $\boldsymbol{\beta}^{(n)}$ and $\alpha^{(n)}$ for the n-th iteration, the 3D object, $\mathbf{f}$, is estimated by minimizing

$$\mathbf{f}^{(n+1)} = \arg \min_{\mathbf{f} \geq \mathbf{0}} \frac{1}{2} \sum_{j=1}^{N_t} \beta^{j(n)} \|\mathbf{g}^j - \mathbf{D}\mathbf{H}^j \mathbf{f}\|^2 + \alpha^{(n)} \mathrm{TV}(\mathbf{f}), \tag{4.13}$$

which can be efficiently solved by using the TwIST algorithm introduced in [**24**], with the non-negativity constraint modification used in [**17**, **68**].

When we have the same variance of noise for all the tiles, we substitute $\mathbf{f}^{(n+1)}$ for $\mathbf{f}$ in Eq. (4.11). Taking derivatives with respect to β and equating to zero, we obtain the following

update rule:

$$\beta^{(n+1)} = \frac{MN_t}{\sum_{j=1}^{N_t} \|\mathbf{g}^j - \mathbf{D}\mathbf{H}^j\mathbf{f}^{(n+1)}\|^2}. \tag{4.14}$$

Similarly, for the case of different noise variance for each tile, we obtain the following update rule for $\boldsymbol{\beta}$:

$$\beta^{j(n+1)} = \frac{M}{\|\mathbf{g}^j - \mathbf{D}\mathbf{H}^j\mathbf{f}^{(n+1)}\|^2}, \quad j = 1, \ldots, N_t. \tag{4.15}$$

To update α, we substitute $\mathbf{f}^{(n+1)}$ for $\mathbf{f}$ in Eq. (4.11), and taking derivatives with respect to α and equating to zero, we obtain the following update rule:

$$\alpha^{(n+1)} = \frac{N}{2\mathrm{TV}(\mathbf{f}^{(n+1)})}. \tag{4.16}$$

The proposed method is summarized in Algorithm 1. Note that the objective function in Eq. (4.11) is always positive, and decreases in each iteration and, therefore, the convergence of the proposed algorithm is guaranteed.

Algorithm 1 MAP-TV Reconstruction for MFM

Require: $n = 0$, the observation $\mathbf{g}$, $\boldsymbol{\beta}^{(0)}$ and $\alpha^{(0)}$.
1: **repeat**
2: Calculate $\mathbf{f}^{(n+1)}$ using TwIST to solve problem in Eq. (4.13).
3: Calculate $\boldsymbol{\beta}^{(n+1)}$ using $\mathbf{f}^{(n+1)}$ in Eq. (4.14) or Eq. (4.15);
4: Calculate $\alpha^{(n+1)}$ using $\mathbf{f}^{(n+1)}$ in Eq. (4.16);
5: $n = n + 1$;
6: **until** Convergence

4.4. Experimental Results

To validate our algorithm, we performed experiments with both synthetic and real data. We compare the performance of the proposed method with the regularized least squares with TV regularizer (RLS-TV) proposed in [**17**]. For RLS-TV, we need to set the regularization

parameter and we performed the exhaustive search for the parameter. Our method is tested in two schemes. In the first scheme, we assume $\beta^1 = \cdots = \beta^{N_t} = \beta$ and estimate β as in Eq. (4.14) (MAP1). MAP1 assumes the same level of noise for all the tiles as RLS-TV. In the second scheme, we estimate each β^j separately as in Eq. (4.15) (MAP2).

4.4.1. Simulation with synthetic data

Our synthetic data is based on experimental data from a 3D image stack of a bacterium obtained by confocal microscopy. It is scaled, cropped, and located to the center of volume composed of $50 \times 50 \times 51$ voxels. Fig. 4.1 (a) shows the bacterium image. To visualize 3D image effectively, we cropped the region around the bacterium to be the size of $35 \times 35 \times 21$ and the center slices of the volume in xy / yz / zx planes are shown in top-left, top-right, and bottom-left of the figure, respectively.

To simulate the MFM experiment, we used the forward model defined in Eq. (4.1) with a measured PSF. We simulated two different levels of Gaussian noise, setting the standard deviation of the noise to $\sigma \in \{0.02, 0.05\}$. At the same time, we also simulated two types of noise for MFM: (1) Gaussian noise whose level is based on the maximum intensity over the whole MFM image, producing the same level of noise for all the sub-images (type 1 noise), and (2) Gaussian noise whose level is proportional to the maximum intensity of each sub-image, producing different level of noise for each sub-image (type 2 noise). By combination of two levels and two types, four different noise cases are simulated. The two cases are shown in Fig. 4.2. From the figures, we can see that the noise level is the same for the whole MFM image in Fig. 4.2 (a), while each tile has a different amount of noise in Fig. 4.2 (b).

The performance of reconstruction in PSNR and SSIM is summarized in Table 4.1. We performed the same simulations 10 times with different random number generator seeds

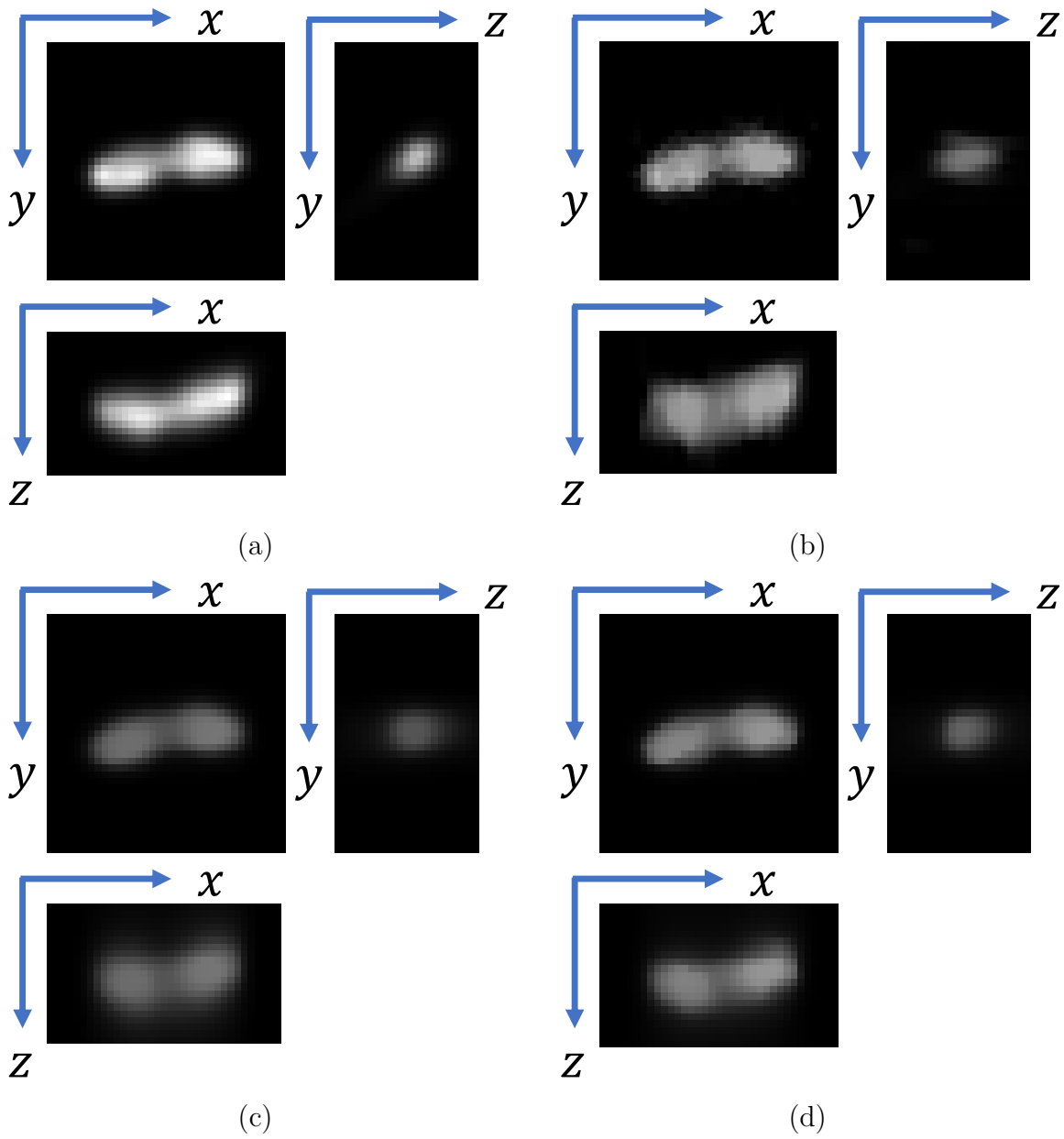

Figure 4.1. Image of a fluorescently labelled bacterium and reconstructed images from MFM measurement with noise type 2, $\sigma = 0.02$. (a) Ground truth from a confocal microscopy image stack, (b) RLS-TV, (c) MAP1, and (d) MAP2

for noise, and calculated the average of the PSNRs and SSIMs of the reconstruction. As described in the table, RLS-TV results in higher PSNRs and SSIMs in most cases. It is

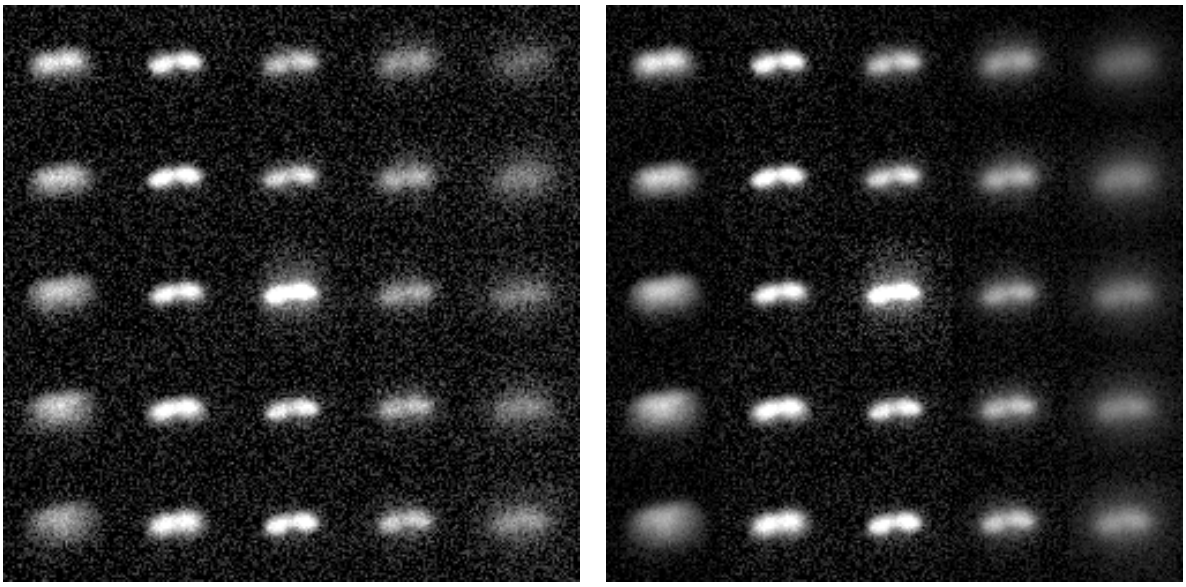

(a) (b)

Figure 4.2. Simulated MFM data based on experimental data of a fluorescently labelled bacterium with two different types of noise. Each of the 25 tiles is at a different focal plane of the same object. (a) Type 1 noise, $\sigma_n = 0.05$, and (b) type 2 noise, $\sigma_n = 0.05$.

reasonable that RLS-TV produces better solutions than MAP-TV1 because we perform an exhaustive search for RLS-TV. The optimal value of the regularization parameter for RLS-TV is chosen based on PSNR/SSIM. MAP1 jointly estimates the parameters corresponding the regularization parameters (α, β) and the 3D image, based on posterior probability but it does not necessarily match the best PSNR parameter. The solution is biased toward the prior that prefers a piecewise smooth image. This argument also applies to MAP2. In fact, for type 2 noise, the MAP2 even produces comparable or better PSNR and SSIM. This is because RLS-TV is based on the assumption that the noise is the same for all tiles, while MAP2 considers different noise levels for each tile. Note that we can also revise RLS-TV to consider different noise by adding the weights for all tiles. However, it becomes impossible

to perform an exhaustive search. Considering 10 values for each parameter, the number of reconstructions to perform in an exhaustive search would be 10^{25}.

Table 4.1. Performance of MFM image reconstruction algorithms. Average PSNR and SSIM are calculated over 10 realizations of noise

	RLS-TV		MAP1		MAP2	
Noise	PSNR	SSIM	PSNR	SSIM	PSNR	SSIM
Type 1, $\sigma = 0.02\max(\mathbf{g})$	36.67	0.9826	35.03	0.9647	34.99	0.9668
Type 1, $\sigma = 0.05\max(\mathbf{g})$	35.01	0.9673	31.14	0.9207	31.22	0.9228
Type 2, $\sigma = 0.02\max(\mathbf{g}^j)$	37.40	0.9891	36.83	0.9773	38.25	0.9804
Type 2, $\sigma = 0.05\max(\mathbf{g}^j)$	35.81	0.9811	33.27	0.9590	34.03	0.9516

The reconstructed images are shown in Fig. 4.1. Visual quality of the reconstructed images from MAP1/2 are clearly better than those from RLS-TV. The reconstructed images from RLS-TV are distorted in xy and elongated in the z-axis. In contrast, MAP1/2 produce more smooth and natural images. The overall intensity level becomes a bit lower than the ground truth but this can be easily compensated. We also notice the different performance between MAP1 and MAP2. The results are similar but MAP2 gives sharper images and less elongation in the z-axis. We observe that the difference between them becomes more obvious with type 2 noise. Because MAP2 is able to estimate different noise for each tile, it also reconstructs higher-quality images.

Fig. 4.3 shows the performance of parameter estimation for noise. For noise type 1, both MAP1 and MAP2 estimate β close to the ground truth. The estimated β^j from MAP2 is varying for each tile even though it has the fixed noise level. This is because the captured object in the tiles affects the variance of the signal. As can be seen in Fig. 4.3 (c) and (d), MAP2 estimates the different noise level precisely, while MAP1 estimates the average noise level.

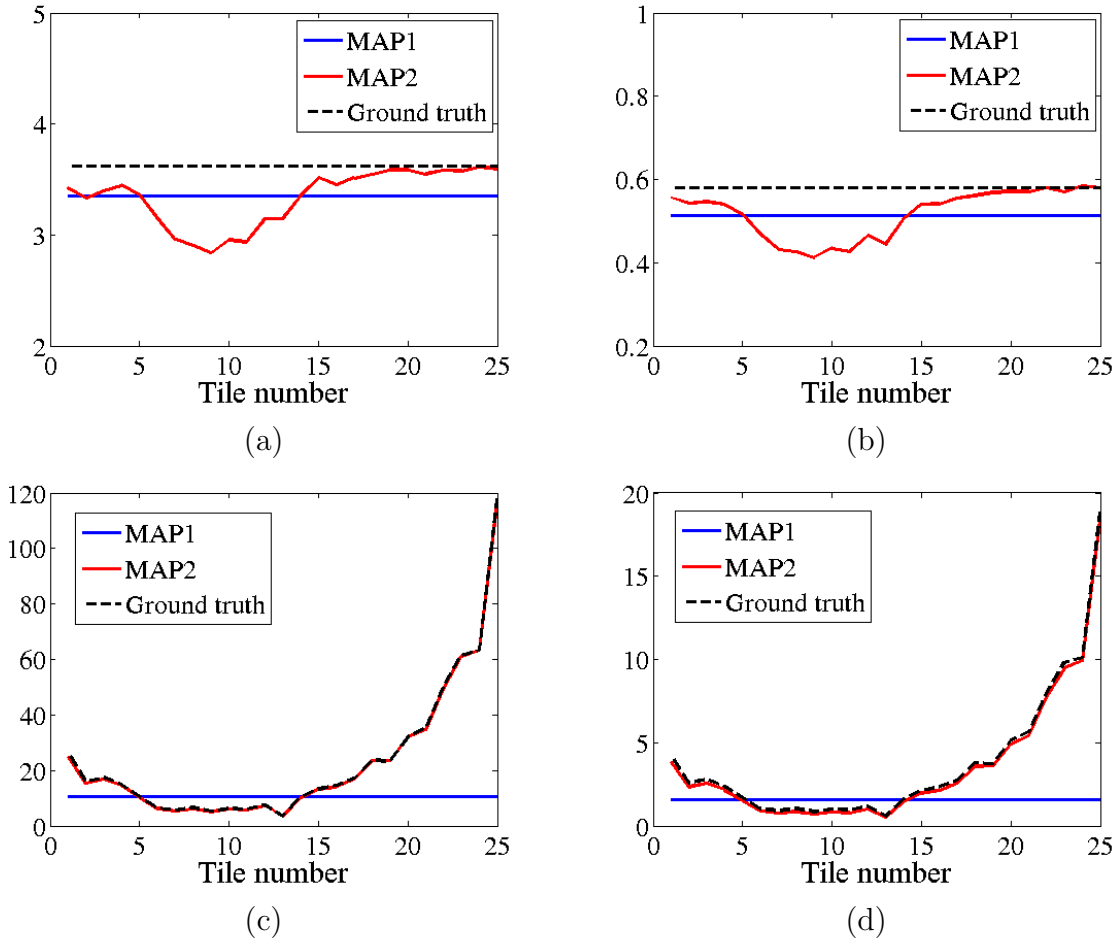

Figure 4.3. Estimation of β with different types and levels of noise. (a) Type 1 noise, $\sigma = 0.02\max(\mathbf{g})$, (b) type 1 noise, $\sigma = 0.05\max(\mathbf{g})$, (c) type 2 noise, $\sigma = 0.02\max(\mathbf{g}^j)$, and (d) type 2 noise, $\sigma = 0.05\max(\mathbf{g}^j)$.

4.4.2. Real experiments

We captured experimental MFM images of a tumbling bacterium with our MFM system [17]. The effective pixel size is $98nm \times 98nm$ and the pixel resolution of the camera is 1024×1024. The image from the MFM consists of 5×5 tiles, and 150×150 pixels in each tile, which is equivalent to $14.7\mu m \times 14.7\mu m$ in sample space. Fig. 4.4 shows a single MFM image from a 200 frame video.

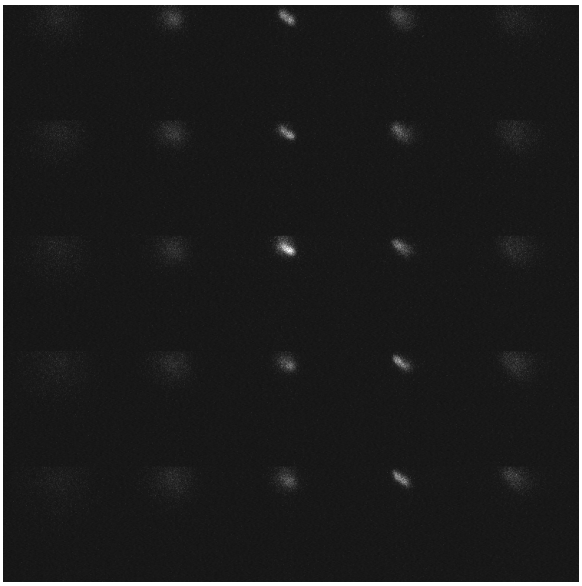

Figure 4.4. MFM experimental measurement of a tumbling fluorescently labelled bacterium

The 3D image reconstructions from the experimental MFM data are shown in Fig. 4.5. We cropped the volume as described in Section 4.4.1 for the simulated data. Fig. 4.5 (a) shows the 3D volume obtained by stacking the tiles with cubic interpolation along the z-axis. It is very noisy and also blurred. Severe out-of-focus blur causes poor resolution in the z-axis. RLS-TV and MAP1/MAP2 produce high-quality reconstructions, achieving axial super-resolution, as shown in Fig. 4.5 (b-d). To compare these methods, MAP-TV is superior to RLS-TV in two aspects. First, it achieves better axial super-resolution. Looking at the xz and yz cuts of the 3D volume in Fig. 4.5, MAP1 and MAP2 produce sharper reconstructions with less elongation in the z-axis. Second, the reconstructions from MAP1 and MAP2 are automatically estimated with other model parameters, while the reconstruction by RLS-TV is obtained by visual inspection after an exhaustive search.

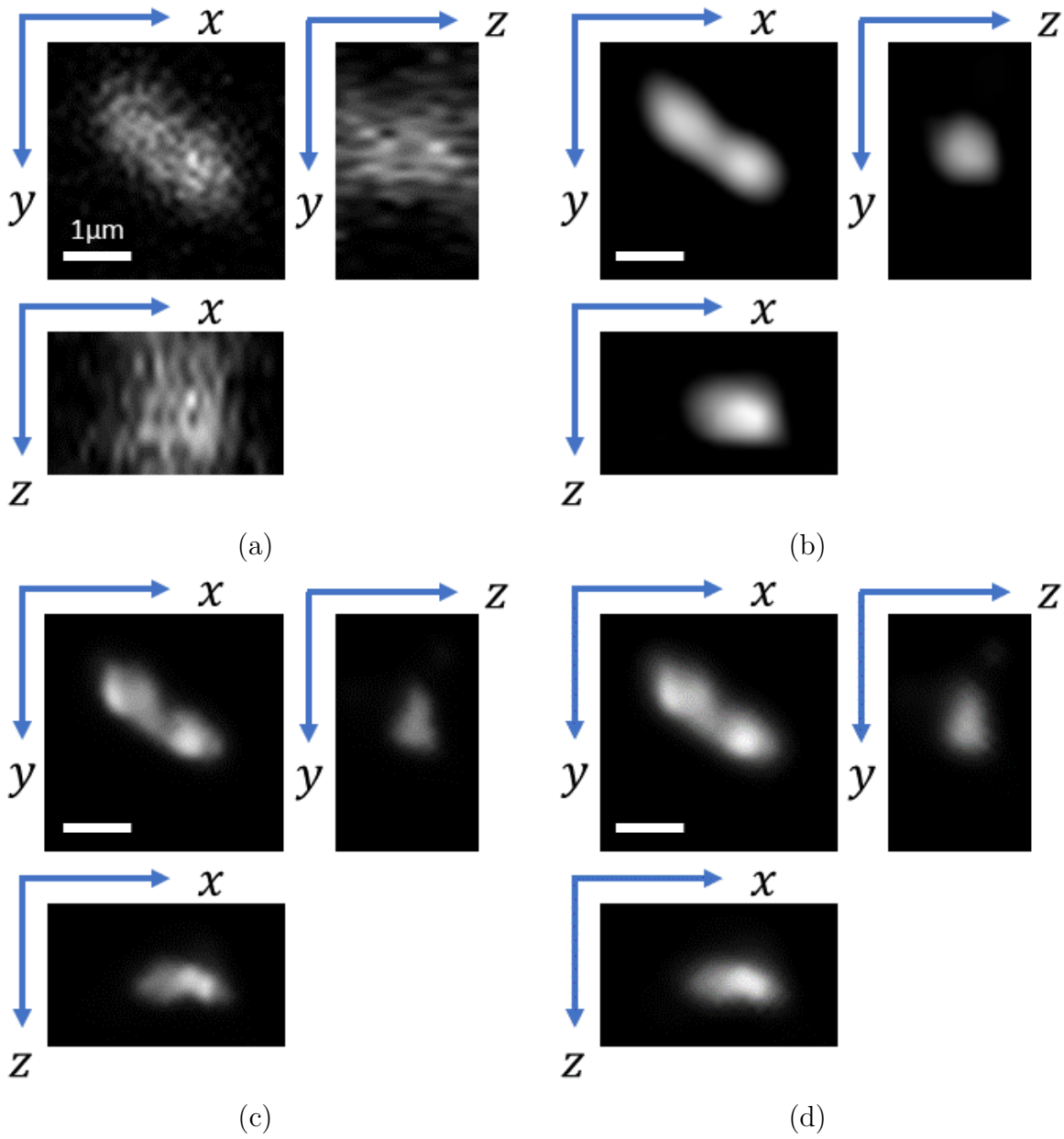

Figure 4.5. 3D image reconstruction from experimental data. (a) tile stacking, (b) RLS-TV, (c) MAP1, and (d) MAP2

4.5. Conclusion

We have introduced a Bayesian modeling for the problem of 3D image reconstruction from MFM images. The model we developed considers two scenarios: (1) the same noise

variance for all of the tiles, and (2) different noise variance for each tile. In order to estimate the parameter of the prior distribution, we have approximated the partition function of the 3D TV prior. MAP inference has been performed to derive an iterative algorithm that automatically estimates all of the unknowns of the problem from the data by alternating between the 3D object estimation and model parameter estimation. The Bayesian modeling and MAP-TV have been evaluated using both synthetic and experimental MFM data. MAP-TV obtained high-quality reconstructions of the 3D object in both cases, including accurate estimations of the noise variances in the synthetic experiment. It has been demonstrated to be competitive comparing with RLS-TV with an exhaustive search of the model parameters.

CHAPTER 5

Poisson Noise Modeling and ADMM-based Image Reconstruction for Multi-Focus Microscopy

In this chapter, we analyze Poisson noise model for multi-focus microscopy (MFM) and develop an image reconstruction algorithm to deal with Poisson noise. MFM captures multiple focal planes on a single camera by splitting the light from different focal planes into different locations on the camera sensor. While the split of light provides the 3D information, it reduces the number of photons that it captures. Thus, in this work, we consider Poisson noise in the forward model for MFM. To deal with Poisson noise, we adopt an alternating direction method of multipliers (ADMM) framework. ADMM splits a Poisson image deconvolution problem into two simpler problems - deblurring and Poisson denoising, allowing an efficient optimization. Maximum a posteriori (MAP) inference is used to estimate the regularization parameter, and the background signal estimation is incorporated in the ADMM framework. Experimental results with synthetic and real data verify the effectiveness of the proposed algorithm.

5.1. Introduction

Acquisition of four-dimensional (4D) data is one of the challenges in modern microscopy. Conventional microscopy requires sequential refocusing for 3D data acquisition, which is too slow to capture the dynamic events in real-time. Multi-focus microscopy (MFM), introduced by Abrahamsson *et al.* in [14], overcomes this problem by simultaneously capturing multiple

focal planes with a single snapshot. Figure 1.1 illustrates the differences between conventional microscopy and MFM. While conventional microscopy (Fig. 1.1 (a) and (b)) can only capture the information for one focal plane, a diffractive optical element (DOE) is introduced in MFM (Fig. 1 (c)) to split the light from different focal planes into different regions of the camera sensor. The 2D image captured by MFM comprises $K \times K$ tiles or sub-images, where each of them corresponds to a different focal plane (see Fig. 1.1 (d)).

In [14], the authors reconstruct the 3D information by stacking the observed tiles, mainly for localization and tracking of an object in the 3D space. However, this method only provides a small number of slices ($K^2 = 9$ or $K^2 = 25$) and the out-of-focus blur and noise remains in the 3D stack. To overcome these limitations, several methods have been developed achieving the 3D reconstruction of an extended object [17, 68, 75]. Huang *et al.* estimated the 3D object using regularized least squares with sparsity and total variation regularizers [17]. Yoo *et al.* further improved the performance of 3D image reconstruction by incorporating information from multiple frames [68]. In [75], Yoo *et al.* proposed a Bayesian modeling for MFM with maximum a posteriori (MAP) inference to jointly estimate the 3D image and the model parameters.

The aforementioned methods assume that the captured image is corrupted by Gaussian noise. In [75], Yoo *et al.* suggested a more general noise model that consider a different noise level for each tile, but they still assume only Gaussian noise. However, MFM has a low photon budget due to its light splitting and low diffraction efficiency of DOE [76] and Poisson noise should be considered in its image reconstruction. Poisson noise is more dominant in a low-photon imaging system, such as, astronomical [52, 53, 71, 77, 78] and biomedical imaging [48, 49, 79–82]. The Richardson-Lucy (RL) algorithm is a classical deconvolution method for Poisson noise model, which uses a multiplicative update based on

the gradient of its log-likelihood function [19,20]. It is known that RL algorithm converges to a noisy solution and thus early stopping must be used. To avoid the undesired noisy solution, regularized RL algorithms were developed [79,83,84]. Tikhonov regularization [83,84], and total variation (TV) regularization [79] are incorporated in RL algorithm.

Other Poisson image deconvolution methods have been developed in the literature [85–87]. Harmany *et al.* presented an optimization framework to use a quadratic approximation of the objective function that consists of log-likelihood and sparsity-promoting penalty terms [85]. Figueiredo and Biocaus-Dias proposed an alternating direction method of multipliers (ADMM) based Poisson image deconvolution method (PIDAL) [86], and Setzer *et al.* presented an algorithm based on split Bregman technique, which is closely related to ADMM [87].

Recently, He *et al.* modeled the MFM imaging system with Poisson noise and applied the TV regularized RL algorithm for 3D image reconstruction [76]. They also jointly estimated the regularization parameter based on the method introduced in [80]. However, the algorithm does not converge to the optimal solution thus the early stopping is used.

In this work, we propose an ADMM framework for 3D image reconstruction from MFM measurements that deals with a Poisson noise and jointly estimates the regularization parameter and the background signal. We formulate the Poisson image reconstruction problem based on the log-likelihood of a Poisson probability distribution and the 3D TV regularization term. In order to handle the non-quadratic, non-separable, and non-smooth objective function, ADMM is used. By using ADMM, we split the Poisson image deconvolution problem into two simpler problems: (1) deblurring and (2) Poisson denoising. We also incorporate the step to estimate the regularization parameter estimation into our ADMM-based framework. Using MAP inference, the regularization parameter is efficiently estimated. The estimation

for background signal is performed inside the ADMM iteration, which is also critical for image reconstruction.

The rest of the paper is organized as follows. The mathematical model for MFM imaging with Poisson noise and the problem that we solve will be described in Section 5.2. Our formulation for MFM image reconstruction based on ADMM framework will be explained in Section 5.3. Experimental results and discussion are provided in Section 5.5 and we conclude our paper in Section 5.6.

5.2. Problem Formulation

Let $\mathbf{f} \in \mathbb{R}^{N\times 1}$, $\mathbf{g}^j \in \mathbb{R}^{M\times 1}$, and $\mathbf{b}^j \in \mathbb{R}^{M\times 1}$ denote the 3D object, the observed image on the j-th MFM tile, and the background signal ($\mathbf{b}^j = b\mathbf{1}$), respectively. For j-th MFM tile ($j = 1, \cdots, K^2$), the image acquisition process is modeled as a linear model with Poisson noise as

$$\mathbf{g}^j = a\mathcal{P}\big(\mathbf{D}\mathbf{H}^j\mathbf{f} + \mathbf{b}^j\big) \tag{5.1}$$

$$= a\mathcal{P}\big(\mathbf{K}^j\mathbf{f} + \mathbf{b}^j\big) \tag{5.2}$$

where $\mathbf{K}^j = \mathbf{D}\mathbf{H}^j$. $\mathbf{D} \in \mathbb{R}^{M\times N}$ is the operator which extracts the central slice of a 3D object and $\mathbf{H}^j \in \mathbb{R}^{N\times N}$ is the PSF matrix of the optical system, respectively. $\mathcal{P}(\cdot)$ denotes the Poisson noise operator, and $a \in \mathbb{R}$ is a conversion factor from the number of photons to pixel intensity that is decided by the quantum efficiency and the electron-multiplying gain of microscope, which is assumed to be known.

Concatenating all the observations from MFM tiles, the image acquisition process in Eq. (5.1) can also be expressed as:

$$\mathbf{g} = a\mathcal{P}\big(\mathbf{K}\mathbf{f} + \mathbf{b}\big), \tag{5.3}$$

where $\mathbf{g} = [\mathbf{g}^{1^T}, \cdots, \mathbf{g}^{K^2{}^T}]^T$, $\mathbf{K} = [\mathbf{K}^{1^T}, \cdots, \mathbf{K}^{K^2{}^T}]^T$, and $\mathbf{b} = b\mathbf{1}$.

By dividing both sides of Eq. (5.3) by a, we obtain

$$\mathbf{g}/a = \mathcal{P}\big(\mathbf{K}\mathbf{f} + \mathbf{b}\big). \tag{5.4}$$

Our goal is to reconstruct the 3D object $\mathbf{f}$, from an observed MFM image, $\mathbf{g}$, where the degradation matrix, $\mathbf{K}$ is known.

The negative log-likelihood of a Poisson distribution of the observed data given the 3D object, produces the following data fidelity term in our objective function

$$\mathcal{L}(\mathbf{f}) = \sum_{i=1}^{MK^2} \Big\{ \big[\mathbf{K}\mathbf{f} + \mathbf{b}\big]_i - \mathbf{g}_i/a \log \big[\mathbf{K}\mathbf{f} + \mathbf{b}\big]_i \Big\}, \tag{5.5}$$

ignoring the constant term from the negative log-likelihood with respect to $\mathbf{f}$. In this work we use a 3D TV regularization term to enforce piecewise smoothness on the reconstructed 3D object [**17**, **68**, **75**], which is defined as

$$\mathrm{TV}(\mathbf{f}) = \sum_{i=1}^{N} \sqrt{(\Delta_i^x \mathbf{f})^2 + (\Delta_i^y \mathbf{f})^2 + (\Delta_i^z \mathbf{f})^2} \tag{5.6}$$

where i is an index for voxels, and Δ^x, Δ^y, and Δ^z denote the first difference operator along the x, y, and z directions, respectively.

Our objective function for 3D image reconstruction is defined as

$$\mathbf{f} = \arg\min_{\mathbf{f}\geq\mathbf{0}} \ \mathcal{L}(\mathbf{f}) + \lambda \mathrm{TV}(\mathbf{f}) \tag{5.7}$$

where λ is a regularization parameter. Note that we also have a non-negativity constraint to obtain the object with non-negative intensity.

5.3. Alternating Direction Method of Multipliers (ADMM) based Optimization

The optimization problem in Eq. (5.7) is hard to solve directly. Even though it is convex, $\mathcal{L}(\mathbf{f})$ is non-quadratic and non-separable with respect to $\mathbf{f}$, and $\mathrm{TV}(\mathbf{f})$ is non-differentiable. In this work we propose to use the ADMM to split the original problem in Eq. (5.7), into two simpler problems: deblurring and Poisson denoising. We will review the standard form of ADMM and then present the ADMM-based algorithm to solve the Poisson image reconstruction.

5.3.1. ADMM

ADMM [88] solves the following problem:

$$\begin{aligned} &\min_{\mathbf{f},\mathbf{u}} f_1(\mathbf{f}) + f_2(\mathbf{u}) \\ &\text{s.t. } \mathbf{A}\mathbf{f} + \mathbf{B}\mathbf{u} = \mathbf{c} \end{aligned} \tag{5.8}$$

where $\mathbf{f} \in \mathbb{R}^{N\times 1}$ and $\mathbf{u} \in \mathbb{R}^{M\times 1}$ are two variables that are related with a linear equality constraint, where $\mathbf{A} \in \mathbb{R}^{P\times N}$, $\mathbf{B} \in \mathbb{R}^{P\times M}$, and $\mathbf{c} \in \mathbb{R}^{P\times 1}$ are known.

The augmented Lagrangian for Eq. (5.8) is formulated as

$$L_\rho(\mathbf{f}, \mathbf{u}, \mathbf{v}) =$$
$$f_1(\mathbf{f}) + f_2(\mathbf{u}) + \mathbf{v}^T(\mathbf{A}\mathbf{f} + \mathbf{B}\mathbf{u} - \mathbf{c}) + \frac{\rho}{2}\|\mathbf{A}\mathbf{f} + \mathbf{B}\mathbf{u} - \mathbf{c}\|_2^2, \tag{5.9}$$

where $\mathbf{v} \in \mathbb{R}^{P\times 1}$ is the Lagrangian multiplier (or dual variable), and $\rho \in \mathbb{R}$ is the penalty parameter of the augmented Lagrangian. The ADMM update rules are derived from Eq. (5.9) as follows:

$$\mathbf{f}^{k+1} = \arg\min_{\mathbf{f}} f_1(\mathbf{f}) + \frac{\rho}{2}\|\mathbf{A}\mathbf{f} + \mathbf{B}\mathbf{u}^k - \mathbf{c}^k + \mathbf{w}^k\|_2^2 \tag{5.10}$$

$$\mathbf{u}^{k+1} = \arg\min_{\mathbf{u}} f_2(\mathbf{u}) + \frac{\rho}{2}\|\mathbf{A}\mathbf{f}^{k+1} + \mathbf{B}\mathbf{u} - \mathbf{c} + \mathbf{w}^k\|_2^2 \tag{5.11}$$

$$\mathbf{w}^{k+1} = \mathbf{w}^k + (\mathbf{A}\mathbf{f}^{k+1} + \mathbf{B}\mathbf{u}^{k+1} - \mathbf{c}), \tag{5.12}$$

where $\mathbf{w} = \mathbf{v}/\rho$.

5.3.2. ADMM for Poisson Image Reconstruction

Let $\mathbf{u} \in \mathbb{R}^{MK^2\times 1}$ be a variable representing the denoised version of the observed variable $\mathbf{g}$. $\mathbf{f}$ and $\mathbf{u}$ are related by an equality constraint which is linear in both variables. Thus the optimization problem in Eq. (5.7) turns into

$$\begin{aligned} &\min_{\mathbf{f},\mathbf{u}} f_1(\mathbf{f}) + f_2(\mathbf{u}) \\ &\text{s.t. } \mathbf{K}\mathbf{f} + \mathbf{b} = \mathbf{u}, \\ &\mathbf{f} \geq \mathbf{0}, \end{aligned} \tag{5.13}$$

where $\mathbf{u} \in \mathbb{R}^{MK^2 \times 1}$, $f_1(\mathbf{f}) = \lambda \mathrm{TV}(\mathbf{f})$, $f_2(\mathbf{u}) = \mathcal{L}_u(\mathbf{u})$, and

$$\mathcal{L}_u(\mathbf{u}) = \sum_{i=1}^{MK^2} \Big\{ \mathbf{u}_i - \mathbf{g}_i / a \log \mathbf{u}_i \Big\}. \tag{5.14}$$

Note that $\mathcal{L}(\mathbf{f})$ in Eq. (5.5) is not separable with respect to $\mathbf{f}$, but $\mathcal{L}_u(\mathbf{u})$ is now separable with respect to $\mathbf{u}$. Thus, it becomes easier to handle the data fidelity term (log-likelihood of Poisson statistics) with respect to $\mathbf{u}$.

This formulation is unique from the previous ADMM formulations for Poisson image deconvolution [86, 87, 89]. In [87] and [86], $f_1(\mathbf{f})$ is set to $\mathbf{0}$ and all the terms are included in $f_2(\mathbf{u}) = \mathcal{L}_u(\mathbf{u}^{(1)}) + \lambda \mathrm{TV}(\mathbf{u}^{(2)}) + \iota_+(\mathbf{u}^{(3)})$, where $\mathbf{u}^{(1)} = \mathbf{K}\mathbf{f}$, $\mathbf{u}^{(2)} = \mathbf{u}^{(3)} = \mathbf{f}$, $\mathbf{u} = [{\mathbf{u}^{(1)}}^T {\mathbf{u}^{(2)}}^T {\mathbf{u}^{(3)}}^T]^T$, and $\iota_+(\cdot)$ is a projection to the non-negative orthant. Rond *et al.* split the objective functions with $f_1(\mathbf{f}) = \mathcal{L}(\mathbf{f})$ and $f_2(\mathbf{u}) = \lambda \mathrm{TV}(\mathbf{u})$ problem with the identity equality constraint, $\mathbf{u} = \mathbf{f}$. The ADMM formulations in [86, 87, 89] are different from ours, and therefore they lead to the different sub-problems.

The augmented Lagrangian for the constrained problem in Eq. (5.13) becomes

$$\begin{aligned} &L_\rho(\mathbf{f}, \mathbf{u}, \mathbf{v}) = \\ &f_1(\mathbf{f}) + f_2(\mathbf{u}) + \mathbf{v}^T(\mathbf{K}\mathbf{f} + \mathbf{b} - \mathbf{u}) + \frac{\rho}{2}\|\mathbf{K}\mathbf{f} + \mathbf{b} - \mathbf{u}\|_2^2 \end{aligned} \tag{5.15}$$

where $\mathbf{v} \in \mathbb{R}^{MK^2 \times 1}$, and this leads to the ADMM update rule for Poisson image reconstruction as follows:

$$\mathbf{f}^{k+1} = \arg\min_{\mathbf{f} \geq \mathbf{0}} \lambda \mathrm{TV}(\mathbf{f}) + \frac{\rho}{2} \|\mathbf{K}\mathbf{f} - \boldsymbol{\xi}^k\|_2^2 \tag{5.16}$$

$$\mathbf{u}^{k+1} = \arg\min_{\mathbf{u}} \mathcal{L}_u(\mathbf{u}) + \frac{\rho}{2} \|\mathbf{u} - \boldsymbol{\nu}^{k+1}\|_2^2 \tag{5.17}$$

$$\mathbf{w}^{k+1} = \mathbf{w}^k + (\mathbf{K}\mathbf{f}^{k+1} + \mathbf{b} - \mathbf{u}^{k+1}) \tag{5.18}$$

where $\boldsymbol{\xi}^{k+1} = -\mathbf{b} + \mathbf{u}^k - \mathbf{w}^k$, $\boldsymbol{\nu}^{k+1} = \mathbf{K}\mathbf{f}^{k+1} + \mathbf{b} + \mathbf{w}^k$, and $\mathbf{w} = \mathbf{v}/\rho$.

The convergence of ADMM is proved [88]. In Sections 5.3.3 and 5.3.4 we explain how to solve the subproblems in Eq. (5.16) and Eq. 5.17), respectively.

5.3.3. Update for f

Fixing the parameters b, ρ and λ, the update rule for $\mathbf{f}$ in Eq. (5.16) can be rewritten as

$$\mathbf{f}^{k+1} = \arg\min_{\mathbf{f} \geq \mathbf{0}} \frac{1}{2} \|\mathbf{K}\mathbf{f} - \boldsymbol{\xi}^k\|_2^2 + \frac{\lambda}{\rho} \mathrm{TV}(\mathbf{f}). \tag{5.19}$$

This is the TV regularized least squares (RLS-TV) with the non-negativity constraint. This problem is convex but non-differentiable because of the TV regularization term. Efficient off-the-shelf algorithms have been developed for RLS-TV [24, 90–92]. We employed TwIST algorithm [24] with two modification: (1) We extend the 2D TV regularization to the 3D TV, and (2) apply the projected gradient scheme by adding the projection to the non-negative orthant for each iteration in order to enforce the non-negativity constraint, following [17, 68, 75].

5.3.4. Update for u

The update for $\mathbf{u}$ in Eq. (5.17) is in the form of proximal operator [93]. This optimization problem is separable with respect to $\mathbf{u}$ as

$$\mathbf{u}_i^{k+1} = \arg\min_{\mathbf{u}_i} \ \mathcal{L}_u(\mathbf{u}_i) + \frac{\rho}{2}(\mathbf{u}_i - \boldsymbol{\nu}_i^{k+1})^2 \tag{5.20}$$

$$= \arg\min_{\mathbf{u}_i} \ \mathbf{u}_i - \mathbf{g}_i/a \log \mathbf{u}_i + \frac{\rho}{2}(\mathbf{u}_i - \boldsymbol{\nu}_i^{k+1})^2 \tag{5.21}$$

where i indicates i-th element of a vector.

Taking derivative of Eq. (5.21) with respect to $\mathbf{u}_i$ and equating it to 0, we obtain a closed form solution as

$$\mathbf{u}_i = \frac{(\rho\boldsymbol{\nu}_i^{k+1} - 1) + \sqrt{(\rho\boldsymbol{\nu}_i^{k+1} - 1)^2 + 4\rho\mathbf{g}_i/a}}{2\rho}. \tag{5.22}$$

Derivation for Eq. (5.22) is provided in Appendix B.

5.4. Parameter Estimation

In the previous sections, we assumed that the parameters, λ, b, and ρ are known. However, in practice, these parameters are unknown, and thus they must be tuned or estimated to obtain a good image reconstruction. In this section, we describe how to jointly estimate the parameters, λ, b, and ρ.

5.4.1. Estimation of Regularization Parameter

The choice of the regularization parameter, λ, is critical in regularization-based reconstruction algorithms. The performance of the image reconstruction highly depends on the parameter. However, the optimal value for the regularization parameter changes depending on the noise variance, and the spectral features of the input image. One way to choose the

parameter is to perform an exhuastive search [17, 68]. After performing the image reconstruction multiple times with different regularization parameters and pick one that produces the best result by some criteria such as mean square error (MSE) or visual quality. But this scheme has serious disadvantages: it is time consuming and it is not possible to have objective evaluation for real data.

In [75], Yoo *et al.* proposed a Bayesian approach to joint estimation problem for 3D image and model parameters from MFM. We propose to adopt this approach to solve the problem in Eq. (5.19) to jointly estimate $\mathbf{f}$ and the regularization parameter. Note that this approach is similar to that of the ADMM Plug-and-Play [89, 94, 95]. Since the ADMM framework split the original problem into two separate problems, the two problems can be handled independently with off-the-shelf methods.

Following the method from [75], the noise level, β, is estimated as

$$\beta = \frac{M}{\|\boldsymbol{\xi} - \mathbf{K}\mathbf{f}\|^2}, \tag{5.23}$$

and the parameter for the TV prior, α, as

$$\alpha = \frac{N}{2\mathrm{TV}(\mathbf{f})}. \tag{5.24}$$

Then, given the estimated parameters, β and α, $\mathbf{f}$, can be estimated by minimizing

$$\hat{\mathbf{f}} = \arg\min_{\mathbf{f}\geq\mathbf{0}} \frac{\beta}{2}\|\boldsymbol{\xi} - \mathbf{K}\mathbf{f}\|^2 + \alpha\mathrm{TV}(\mathbf{f}) \tag{5.25}$$

$$= \arg\min_{\mathbf{f}\geq\mathbf{0}} \frac{1}{2}\|\boldsymbol{\xi} - \mathbf{K}\mathbf{f}\|^2 + \lambda\mathrm{TV}(\mathbf{f}), \tag{5.26}$$

where $\lambda = \alpha/\beta$. Note that the regularization parameter, λ is implicitly calculated by α and β.

In this way, the regularization parameter is automatically estimated and this step is embedded in the first ADMM step of $\mathbf{f}$ estimation.

5.4.2. Estimation of Background Signal

In real measurement, the background signal, $\mathbf{b}$, is not known, and therefore it must be estimated. To solve this problem, we include the following update rule in the original ADMM algorithm in Eqs. 5.16,5.17,5.18 just after the estimation of $\mathbf{f}$:

$$\mathbf{b}^{k+1} = \arg\min_{\mathbf{b}\geq\mathbf{0}} \|\mathbf{b} - \boldsymbol{\gamma}^{k+1}\|_2^2 \tag{5.27}$$

where $\boldsymbol{\gamma}^{k+1} = -\mathbf{K}\mathbf{f}^{k+1} + \mathbf{u}^k - \mathbf{w}^k$.

Taking derivative of Eq. 5.27 with respect to $\mathbf{b}$ and equating to $\mathbf{0}$, we obtain a closed form solution as

$$\mathbf{b} = \boldsymbol{\gamma}^{k+1}. \tag{5.28}$$

Since we assume a uniform background signal, or $\mathbf{b} = b\mathbf{1}$, the estimation of b is

$$b = \frac{1}{MK^2}\sum_{i}^{MK^2} \boldsymbol{\gamma}_i^{k+1} \tag{5.29}$$

where i is an index for pixels. Derivation for Eq. (5.28) and Eq. (5.29) is in Appendix B.

5.4.3. Choice of Penalty Parameter

We fix the value of ρ to 1 for all the experiments. This can be justified with two facts. First, for any fixed ρ, the convergence of ADMM framework is proved [**88**]. Therefore, it is reasonable to use a fixed ρ theoretically. Second, we found that the value of ρ is not

Algorithm 2 ADMM-Based Image Reconstruction for MFM

Require: $k = 0$, $\mathbf{g}$, $\mathbf{f}^0$, b^0, $\mathbf{u}^0$, $\mathbf{w}^0$, α^1, and β^1

repeat
  Update $\mathbf{f}^{k+1}$
    Calculate β^{k+1} if $k > 0$ as Eq. (5.23)
    Calculate α^{k+1} if $k > 0$ as Eq. (5.24)
    Calculate $\mathbf{f}^{k+1}$ using TwIST to solve problem in Eq. (5.25)
  Update b^{k+1} as Eq. (5.29)
  Update $\mathbf{u}^{k+1}$ as Eq. (5.22)
  Update $\mathbf{w}^{k+1}$ as Eq. (5.18)
  $k = k + 1$;
until Convergence

important by itself for the performance from our experiments. Rather, the ratio of ρ and λ is critical as will be shown in Section 5.5.1.8.

The whole procedure of the proposed method is summarized in Algorithm 2.

5.5. Results and Discussion

In this section, we show the experimental results for both synthetic and real data sets. First, we perform the quantitative evaluation the proposed algorithm on simulations with synthetic data. Then, we discuss the details of algorithm including effect of background signal, axial super-resolution, and choice of penalty parameter in the ADMM. Finally, 3D image reconstruction with real experimental data is shown.

The results are compared with the state-of-the-art Poissonian image deconvolution methods, SPIRAL-TV [**85**] and jointly regularized RL-TV (JRL-TV) [**76**]. Note that while our method and JRL-TV jointly estimate the regularization parameter and the background signal as well as 3D image, SPIRAL-TV only estimates the 3D image. An exhaustive search is performed to obtain the optimal regularization parameter. For the background signal, the

true value or the estimated value is given to the algorithm depending on whether the data is either simulated or experimental.

5.5.1. Simulation with Synthetic Data

5.5.1.1. Test data and simulation setup. We test the algorithm with three synthetic data: One-Ellipsoid, Two-Ellipsoids, and Bacterium. The first two objects, One-Ellipsoid and Two-Ellipsoids, are fully synthetic, and Bacterium is based on experimental data from a 3D image stack of a bacterium obtained by confocal microscopy. One-Ellipsoid and Two-Ellipsoids are created to imitate the bacterial periplasm, and differentiate the number of bacteria. Each data has a dimension of $50 \times 50 \times 51$ voxels. These objects are shown in Fig. 5.1. To visualize 3D image effectively, we show slices of the volume in xy / yz / zx planes in the top-left, top-right, and bottom-left of the figure, respectively, and a 3D angle view in the bottom-right. For the 3D angle view, we used a color-map that blue and red indicate the lowest and highest intensity, respectively, and also display three projections onto the xy / yz / zx planes. Voxels whose intensity is less than a threshold are set to 0 to visualize the signal more clear.

To simulate the MFM measurement, we used the forward model defined in Eq. (5.3). The PSF is measured by capturing a fluorescent bead through the MFM system with 5-by-5 tiles and $250nm$ focal step. We set the conversion factor $a = 1$ for our simulation so that the number of photons exactly match the intensity of the MFM images for simplicity. To simulate different levels of Poisson noise (in other words, different budgets of photons), four different maximum photon (MP) counts are set for the simulated MFM images: 25, 50, 100, and 200. The uniform background signal, b, is set to 5 unless we specify it. Simulated MFM images with 50 MP count for the three test data are shown in Fig. 5.2. The center

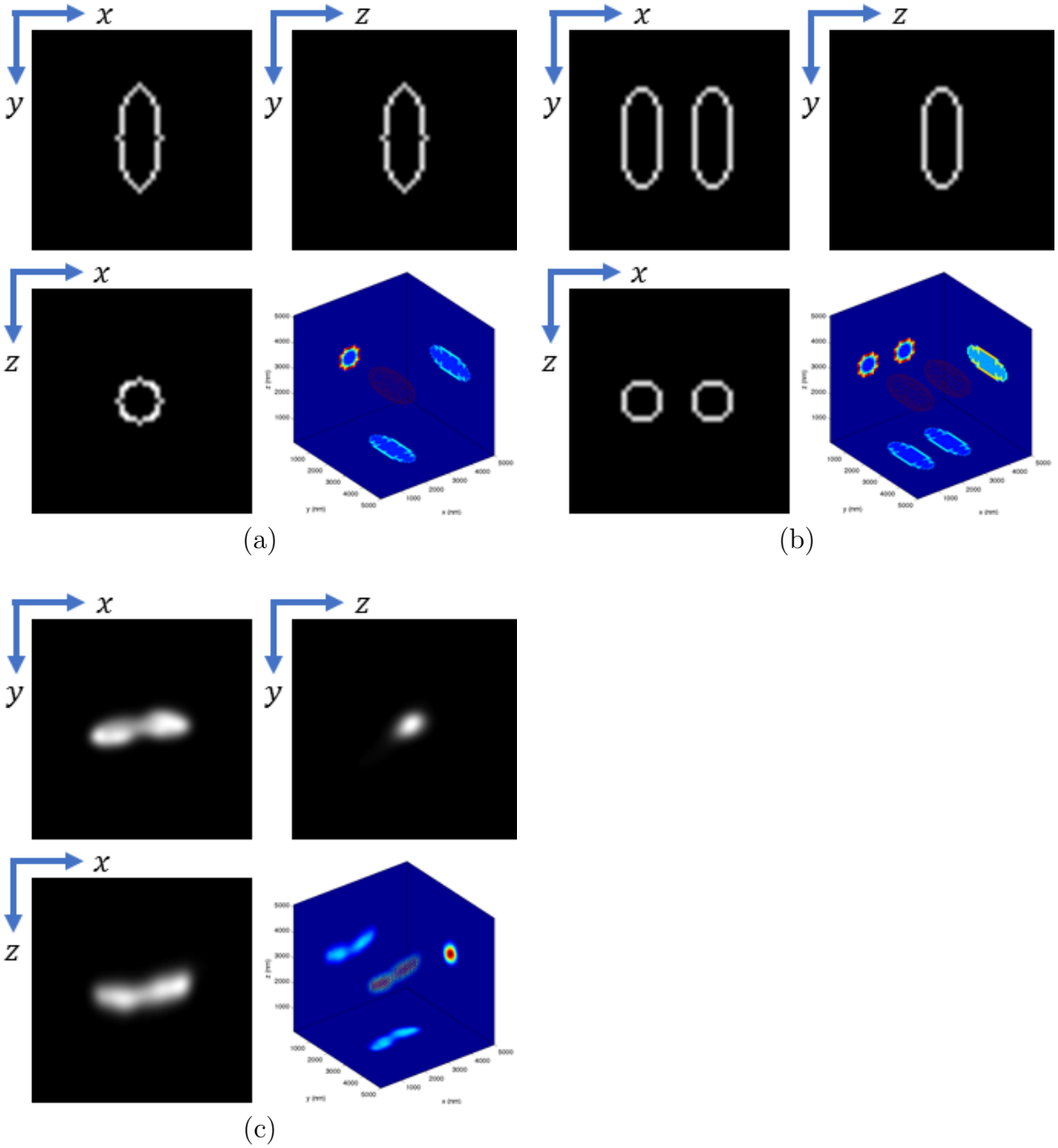

(a) (b) (c)

Figure 5.1. Synthetic data for simulation. The first two images are fully synthetic, and the third one is based on experimental data from a 3D image stack of a bacterium obtained by confocal microscopy (a) One-ellipsoid, (b) Two-ellipsoids, and (c) Bacterium.

area in a red box is zoomed in 5 times and displayed in the top-right corner. Figure 5.3 shows the simulated MFM images of One-Ellipsoid with MPs 25, 50, 100, and 200. As the number of photons increases, the measurement becomes less noisier, following the Poisson noise statistics.

5.5.1.2. Stopping criteria and algorithm initialization. To check the convergence of Algorithm 2, we measure the difference between the reconstructed images in the current and the previous iterations, $\delta_{\mathbf{f}}^k$ as Eq. (5.30). The thresholds are set to 10^{-5} and 10^{-3} for the inner loop (step 5 in Algorithm 2) and the outer loop of the ADMM, respectively. For the other algorithms, the difference of their objective functions, δ_J^k, is measured to check the convergence as Eq. (5.31) and they stop when $\delta_J^k < 10^{-7}$. We observe SPIRAL-TV and JRL-TV approach noisy solutions after some iterations so we limit the maximum iterations to 200 for early stopping where their performance is still reasonable. We set the initial value for λ to 10^{-6}.

$$\delta_{\mathbf{f}}^k = \frac{\|\mathbf{f}^k - \mathbf{f}^{k-1}\|}{\|\mathbf{f}^{k-1}\|} \tag{5.30}$$

$$\delta_J^k = \frac{\|J(\mathbf{f}^k) - J(\mathbf{f}^{k-1})\|}{\|J(\mathbf{f}^{k-1})\|} \tag{5.31}$$

where $J(\cdot)$ indicates the objective function.

5.5.1.3. Qualitative Performance Evaluation. Figures 5.4, 5.5, 5.6 show the reconstructed 3D image from the three different test data when MP = 100. The result from our method is compared with the 3D stack of MFM tiles, and results from two other methods: SPIRAL-TV, and JRL-TV. For the 3D stack, tiles of MFM are piled up in order and re-scaled in the z-axis to the same scale as other reconstruction with Cubic interpolation method. Compared to the 3D stack, SPIRAL-TV, JRL-TV, and our method effectively perform deblurring and denoising from MFM images. We clearly see the empty space inside

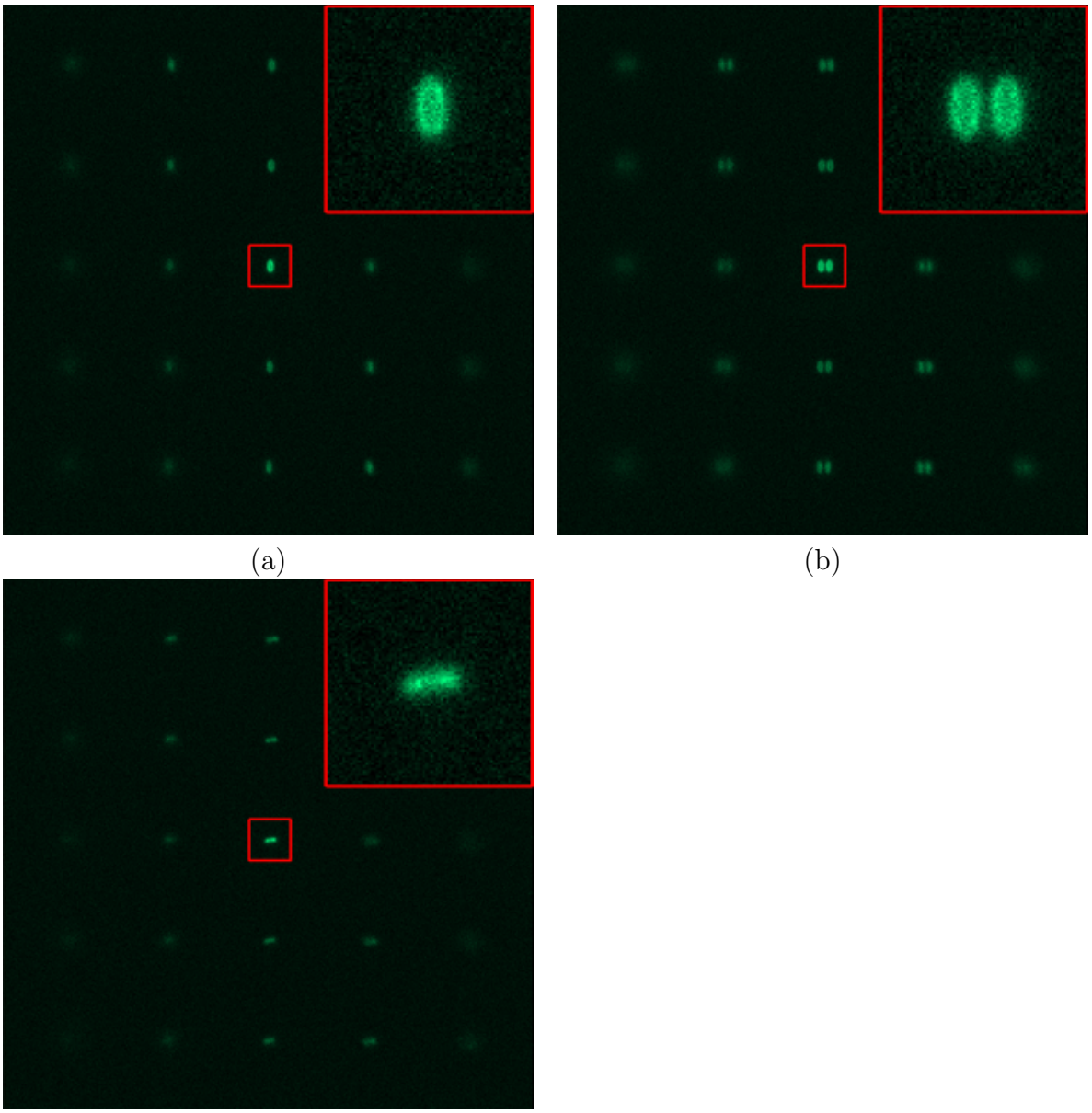

(a) (b)

(c)

Figure 5.2. Simulated MFM measurement of test data in case of MP count 100 and $b = 5$. (a) One-ellipsoid, (b) Two-ellipsoids, and (c) Bacterium.

the objects of One-ellipsoid and Two-ellipsoids, while the 3D stack fills the empty space. It is because of severe out-of-focus blur, which is common in the microscopy [66, 96]. We also observe that the reconstructed images from our method is closer than those of SPIRAL and

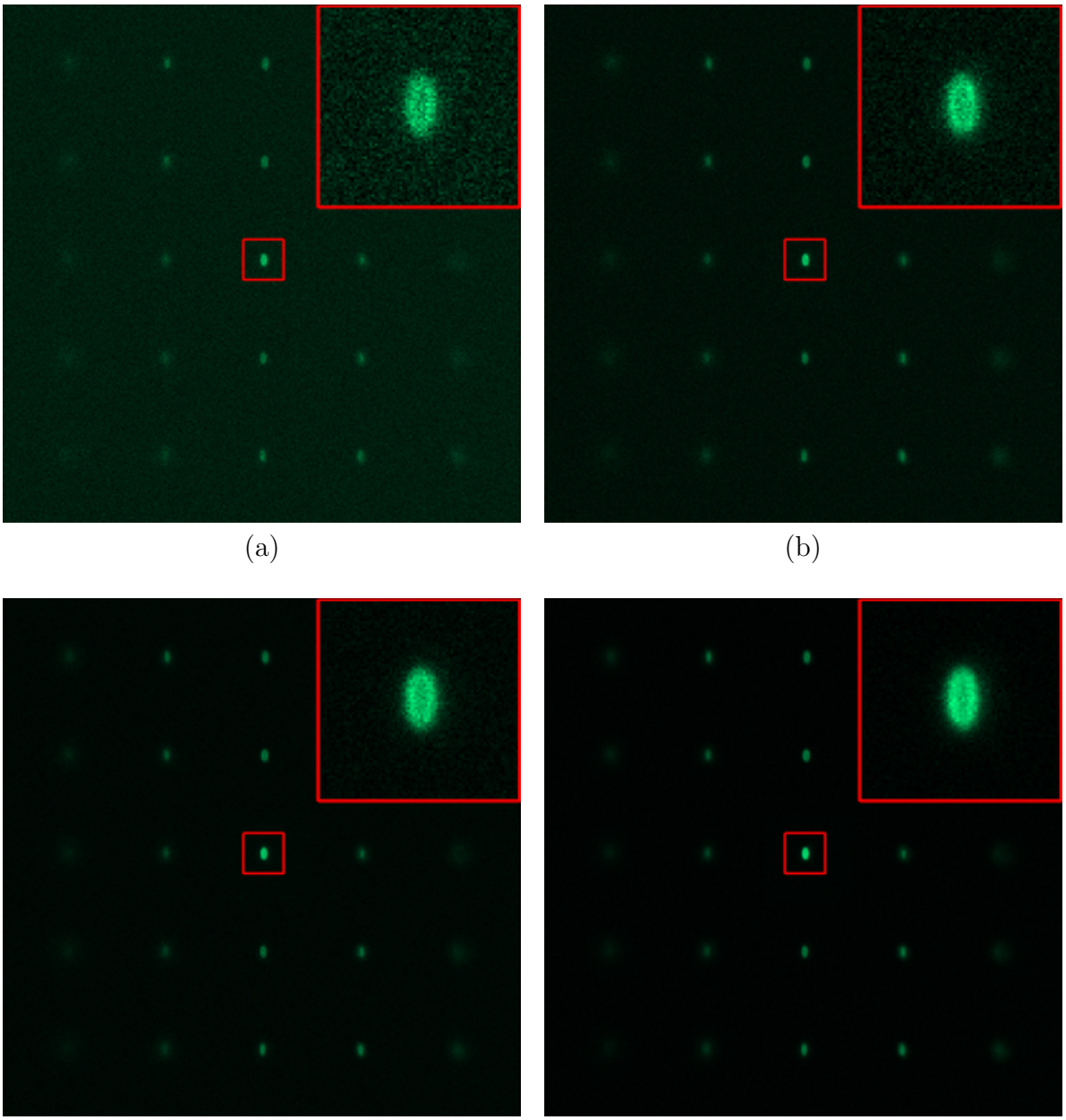

(a) (b)

(c) (d)

Figure 5.3. Simulated MFM measurement of One-ellipsoid with different noise levels, (a) MP 25, (b) MP 50, (c) MP 100, and (c) MP 200.

JRL-TV to the ground truth data that are shown in Fig. 5.1 for One-ellipsoid and Two-ellipoids. The intensity of signal is higher than the others and the boundary is sharper than

the others. Projections in the 3D angle views show that the reconstruction from our method preserve the empty space inside the ellipsoids better than the others. From Fig. 5.6, the visual quality of reconstruction of Bacterium by our method is similar to that of JRL-TV. SPRIAL-TV obtains a smoother but more blurred image.

5.5.1.4. Quantitative Performance Evaluation. Table 5.1 summarizes the performance of the reconstruction algorithms for MFM. The peak signal-to-noise ratio (PSNR) and the structural similarity (SSIM) index are used for qualitative performance measure. In all the cases, we observe that the performance of reconstruction increases as MP increases. Obviously, it is because signal-to-noise ratio (SNR) increases along with MP. While our method obtains the highest PSNRs and SSIMs for One-ellipsoid and Two-ellipsoids in every noise level, JRL-TV has the highest PSNRs and SSIMs for Bacterium. JRL-TV tends to introduce smoothness in the reconstructed images more than our method, resulting in higher PSNRs for the very smooth object. We observe that JRL-TV estimates a higher value of the regularization parameter as will be discussed more in Section 5.5.1.5.

Table 5.1. Performance of 3D image reconstruction from MFM.

Methods		SPIRAL-TV		JRL-TV		Ours	
Test image	MP	PSNR	SSIM	PSNR	SSIM	PSNR	SSIM
One-ellipsoid	25	25.80	0.9497	25.66	0.9624	25.88	0.9662
	50	25.96	0.9606	25.91	0.9651	26.39	0.9710
	100	25.86	0.9649	26.12	0.9677	26.46	0.9717
	200	26.37	0.9697	26.23	0.9693	27.38	0.9785
Two-ellipsoids	25	22.85	0.9169	22.72	0.9205	22.84	0.9274
	50	22.72	0.9257	22.98	0.9301	23.38	0.9435
	100	23.05	0.9337	23.01	0.9331	23.61	0.9475
	200	22.87	0.9319	23.11	0.9357	24.28	0.9558
Bacterium	25	36.51	0.9736	38.70	0.9901	36.80	0.9883
	50	38.28	0.9830	39.19	0.9914	38.49	0.9897
	100	38.64	0.9886	42.33	0.9954	40.84	0.9920
	200	39.75	0.9936	40.26	0.9961	38.21	0.9898

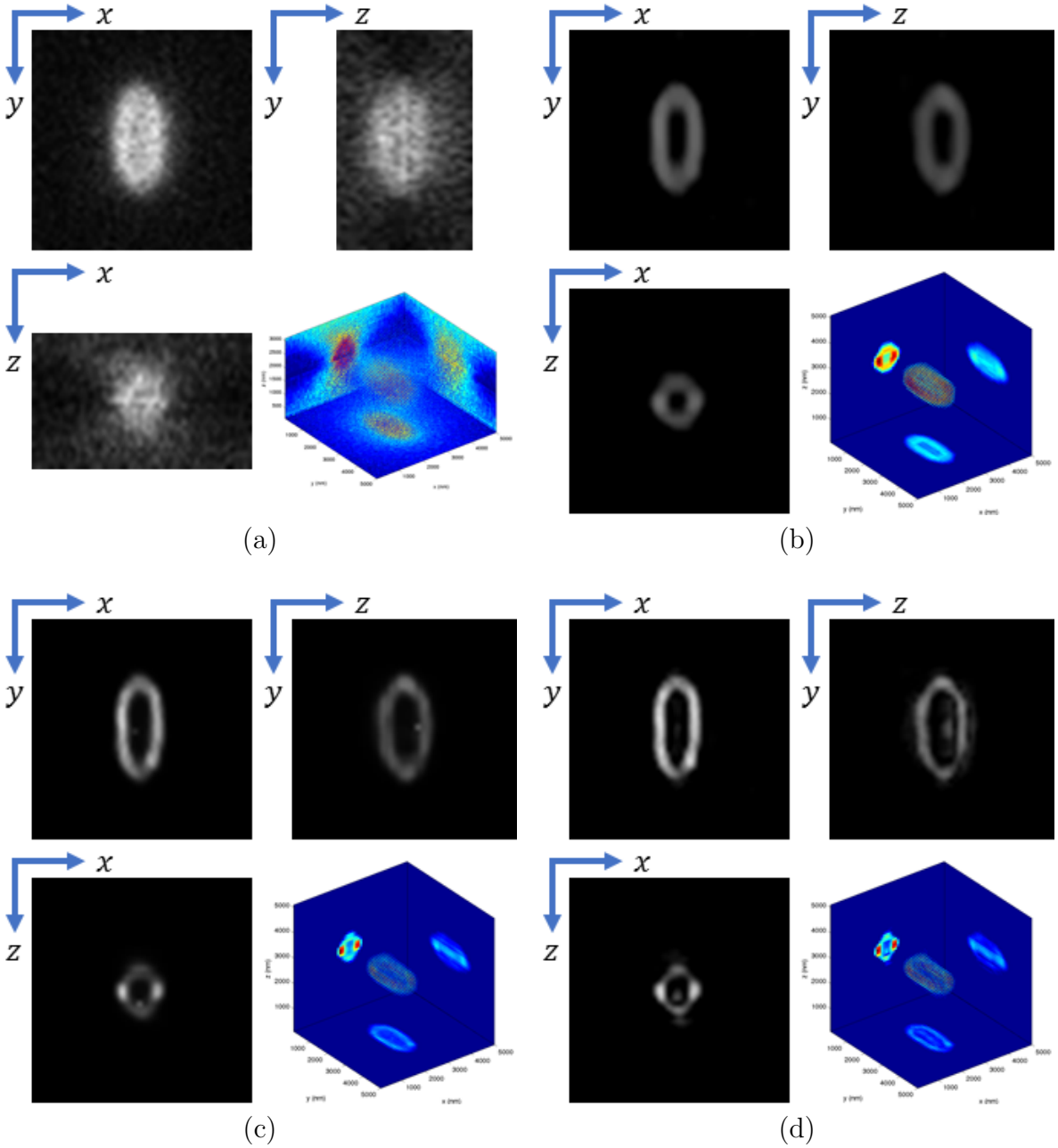

Figure 5.4. 3D image reconstruction from our method for One-ellipsoid in case of MP count 100 and $b = 5$. (a) 3D stack of tiles, (b) SPIRAL-TV, PSNR: 25.86 dB, SSIM: 0.9649 (c) JRL-TV, PSNR: 26.12 dB, SSIM: 0.9677 and (d) ours, PSNR: 26.46, SSIM: 0.9717

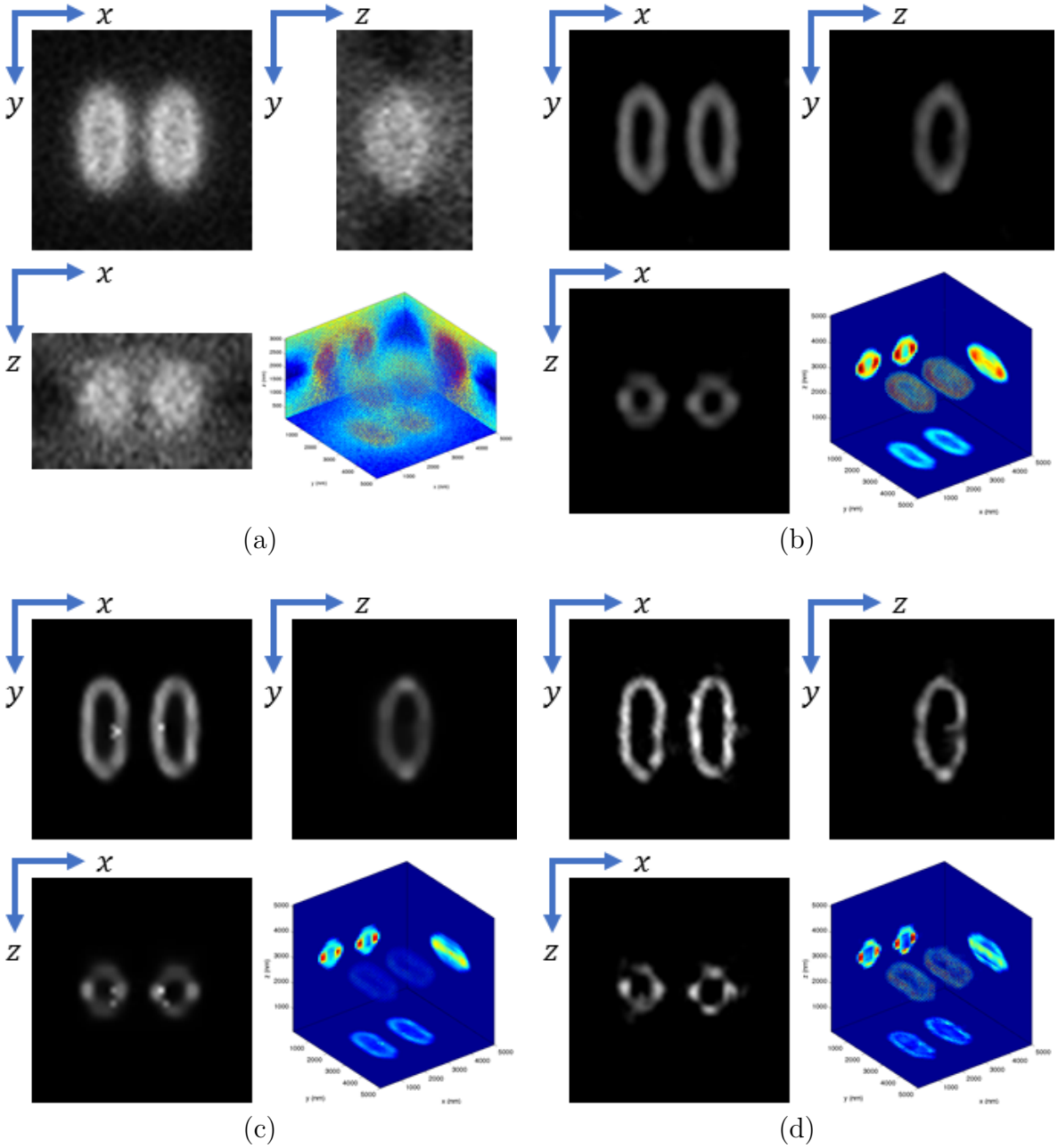

Figure 5.5. 3D image reconstruction from our method for Two-ellipsoids in case of MP count 100 and $b = 5$. (a) 3D stack of tiles, (b) SPIRAL-TV, PSNR: 23.05 dB, SSIM: 0.9337 (c) JRL-TV, PSNR: 23.01 dB, SSIM: 0.9331 and (d) ours, PSNR: 23.61, SSIM: 0.9475

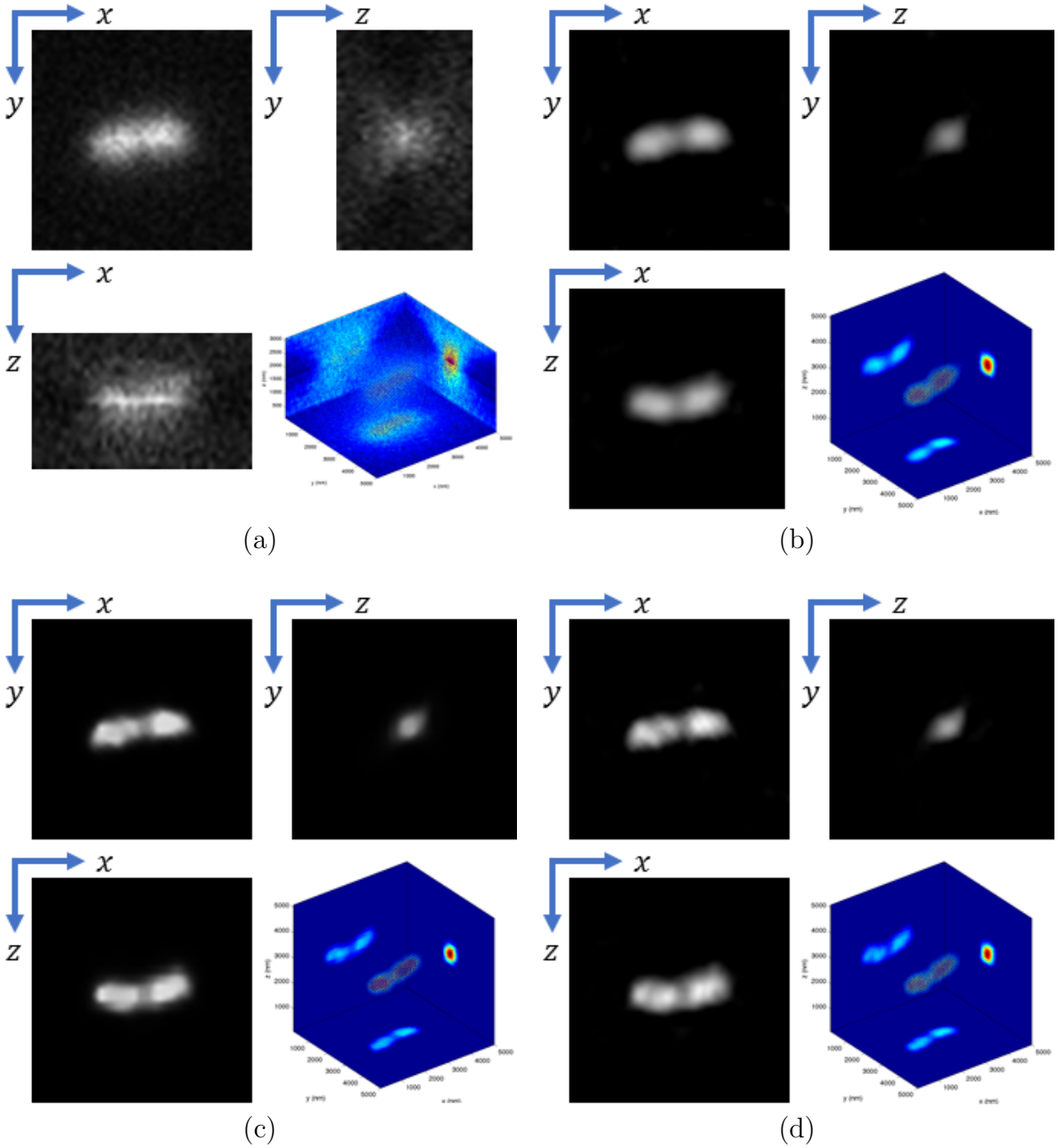

Figure 5.6. 3D image reconstruction from our method for Two-ellipsoids in case of MP count 100 and $b = 5$. (a) 3D stack of tiles, (b) SPIRAL-TV, PSNR: 38.64 dB, SSIM: 0.9886 (c) JRL-TV, PSNR: 42.33 dB, SSIM: 0.9954 and (d) ours, PSNR: 40.84, SSIM: 0.9920

The computation time in minutes and the number of iterations for the reconstruction methods are reported in Table 5.2. Note that, with parallel processing, the actual running time is less than the CPU time. From the table, three methods have comparable computation time. However, JRL-TV often reaches the maximum iteration limit so it would take longer than the time in the table without early stopping. Also, SPIRAL-TV requires a manual search for the regularization parameter, thus the actual computation time should be multiplied by the number of parameters tried. Our method has an outer iteration for the ADMM updates and an inner iteration for $\mathbf{f}$ estimation step, so all the inner iterations are added up for fair comparison.

Table 5.2. Computation time for 3D image reconstruction from MFM. CPU time is in minutes.

Methods		SPIRAL-TV		JRL-TV		Ours	
Test image	MP	Time	Iter.	Time	Iter.	Time	Iter.
One-ellipsoid	25	28.5	76	59.0	200	31.4	54
	50	36.6	99	53.2	193	40.7	79
	100	41.7	103	49.3	200	28.0	103
	200	48.0	124	50.6	200	46.3	168
Two-ellipsoids	25	27.7	76	72.7	191	45.0	59
	50	27.5	70	74.7	200	36.8	85
	100	40.5	110	73.8	200	53.4	139
	200	48.1	115	75.5	200	73.6	221
Bacterium	25	19.1	51	58.2	161	25.1	18
	50	25.2	63	34.2	92	20.0	27
	100	33.6	94	74.6	200	38.3	37
	200	37.3	99	73.1	200	22.5	39
Average		34.5	90.0	62.4	186.4	38.3	70.0

The performance of the background signal estimation is described in Table 5.3. We observe that both JRL-TV and the proposed method, achieve accurate estimations for the background signal parameter, whose real value is $b_{true} = 5$. However, in all the cases, the estimation provided by JRL-TV is slightly closer to b_{true} than the proposed method.

Table 5.3. Performance of estimation of the background signal

Test data	One-ellipsoid		Two-ellipsoids		Bacterium	
MP	JRL-TV	Ours	JRL-TV	Ours	JRL-TV	Ours
25	4.9943	4.9770	4.9919	4.9741	4.9938	4.9776
50	4.9935	4.9759	4.9919	4.9776	4.9940	4.9751
100	4.9935	4.9709	4.9905	4.9769	4.9947	4.9749
200	4.9956	4.9722	4.9910	4.9799	4.9934	4.9693

5.5.1.5. Estimation of the Regularization Parameter. The regularization parameters estimated by JRL-TV and the proposed method for each reconstruction are plotted in Fig. 5.7. First, we observe that the general trend is that the estimated λ decreases as MP increases. This is related to the noise level. A larger photon budget reduces the noise level so less weight on the regularization term is needed. Second, the regularization parameter depends on the data. The estimated regularization parameter for Bacterium is larger than One-ellipsoid and Two-ellipsoids. Bacterium is more piecewise smooth than the others, and thus a higher weight on the TV regularization is more needed than the others. Also, One-ellipsoid is more piecewise smooth than Two-ellipsoids since it has only half of the signal of the other.

There are a couple of differences in λ estimation between JRL-TV and ours. The values of estimated λ of JRL-TV are one to two orders of magnitude larger than those from ours. This tendency results in different reconstruction. As seen in Figs. 5.4, 5.5, and 5.6, JRL-TV makes the 3D image more smooth than our method does. It could improve the visual quality but loses the high frequency content as trade-off. Also, the estimated values do not change as much as MP changes. In case of Two-ellipsoids with 200 MP, it even has a larger λ than the case with 100 MP against the natural trend.

5.5.1.6. Effect of Background. We investigate the effect of the background signal on the performance of image reconstruction in two aspects: (1) the effect of the level of the

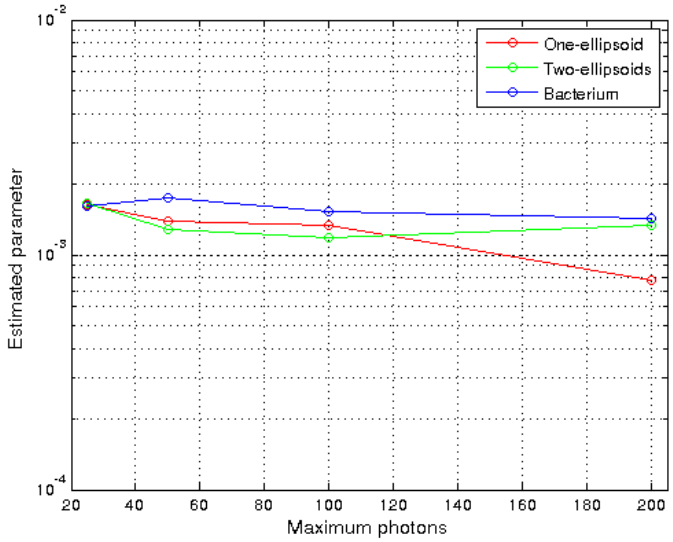

(a)

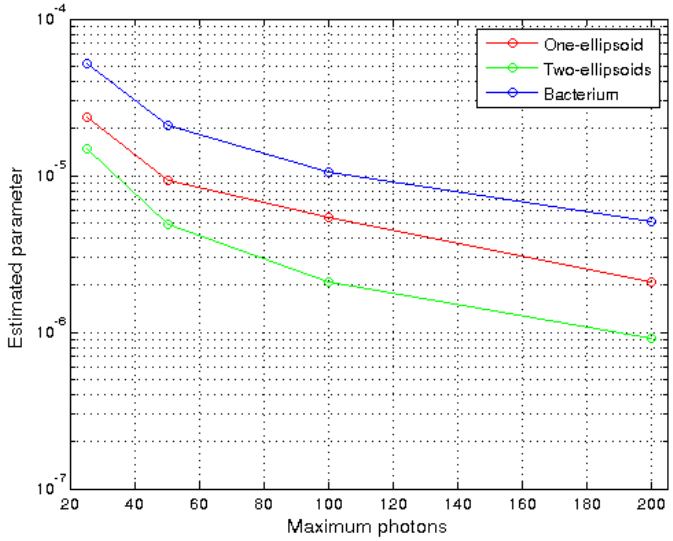

(b)

Figure 5.7. Estimation of the regularization parameter λ for TV term with respect to maximum photon counts for (a) JRL-TV, and (b) our method

background signal on the performance of image reconstruction, and (2) the effect of inaccurate estimation of the background signal. To see the effect of the level of the background signal, we perform simulations with different background signals, $b = 0, 10, 20, \cdots, 100$. MP

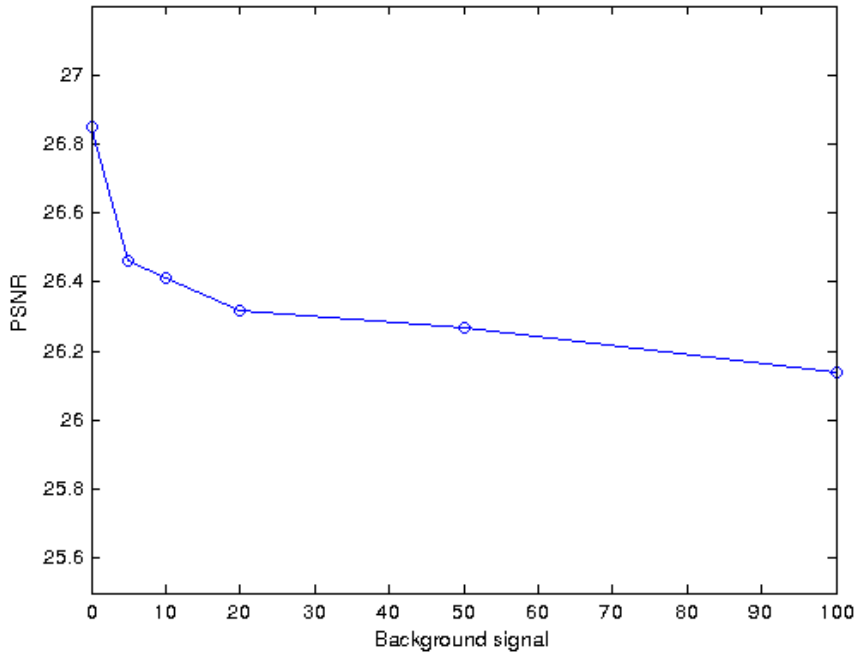

Figure 5.8. Effect of the level of the background signal. The higher background signal decrease the performance of image reconstruction.

is set to 100 for these experiments. The plot in Fig. 5.8 illustrates the performance of image reconstruction in PSNRs with respect to b: the more background, the less PSNR. This can be explained by the nature of Poisson noise. The variance of Poisson noise increases as b gets larger. It is clear that the larger variance of noise will decrease the performance of the image reconstruction.

In order to see the effect of inaccurate estimation of the background signal, we perform simulations without the background signal estimation (Step 6 in Algorithm 2). While we set $b_{true} = 5$, the image reconstruction is performed with different values of b: $b = 0, \cdots, 10$. The results are plotted in Fig. 5.9. As seen in the figures, wrong estimation of the background signal degrades the performance of reconstruction. Even with small difference from the true value, it significantly decrease PSNR and SSIM. The level of degradation is smaller when it

overestimates but PSNR still drops 2 dB with 1 photon count mis-estimation. Estimating the accurate background signal is critical to the image reconstruction of MFM.

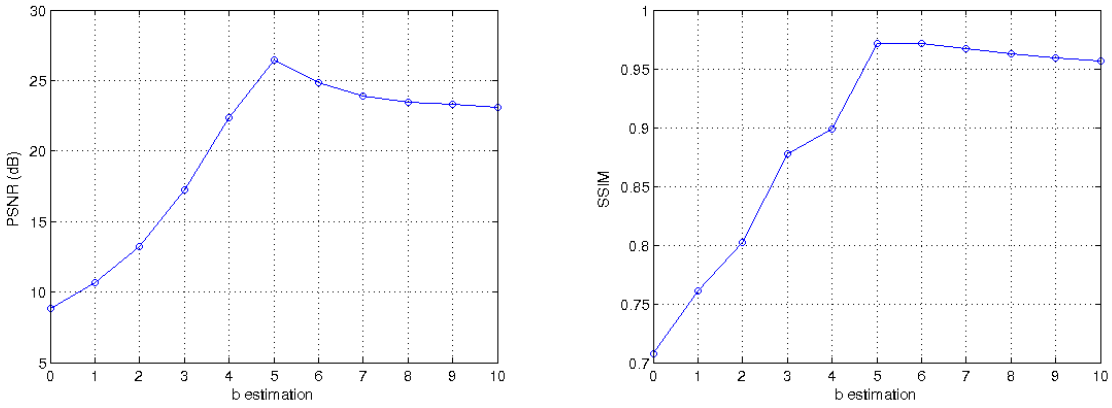

(a) (b)

Figure 5.9. Effect of accuracy of background signal estimation. The true value of b is 5 (b_{true}), and different values of b are used for image reconstruction. Inaccurate estimation of the background signal degrades the performance of reconstruction.

5.5.1.7. Axial Super-Resolution. Compared to 3D stack of MFM tiles, the image reconstruction algorithms provide higher resolution 3D image. Severe out-of-focus blur in microscopy degrades axial resolution of the captured image, but these algorithms can achieve super-resolution. In order to see this, we analyze the reconstructed image with (1) its profile in the z-axis and (2) its $k_x k_z$ slice in frequency domain.

Figure 5.10 shows the z profile of reconstructed 3D image of One-ellipsoid from different algorithms when MP = 200. As shown in Fig. 5.10 (b), 3D stack of MFM tiles cannot resolve two peaks of signal in the distance of 1 μm. By performing image reconstruction methods, they are clearly separated. The reconstructed image from our method is the closest to the ground truth in terms of the intensity and the width of the peaks.

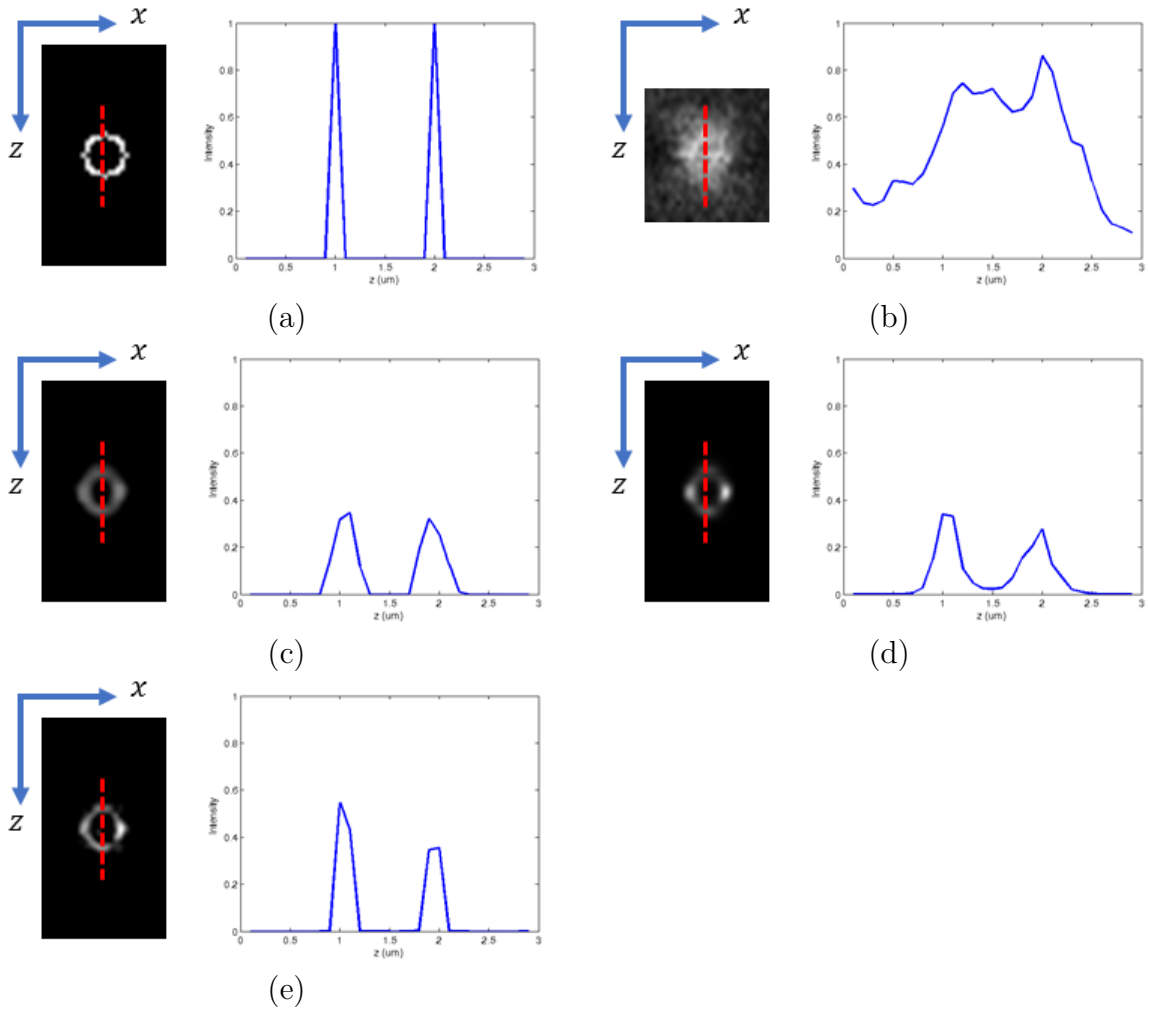

Figure 5.10. Profile in the z-axis of the reconstructed One-ellipsoid image. (a) Ground truth, (b) 3D stack of MFM tiles, (c) SPRIAL-TV, (d) JRL-TV, and (e) our method

The slices in the $k_z k_x$ plane in the frequency domain are shown in Fig. 5.11. The ground truth signal has a pattern of concentric circles, but the 3D stack of MFM tiles loses this pattern except for the center area, which is the low frequency part. While all the computational methods preserve the patterns to some degree, there are differences among their results. We observe a 'missing cone' in Fig. 5.11 (d) where the concentric circle is cut in cone shape to the k_z direction. It means the reconstruction from JRL-TV loses the high

frequency information in the z direction. The pattern of SPIRAL-TV gets distorted and the signal becomes weaker (darker) as it approaches the high frequency area as in Fig. 5.11 (c). There is some distortion of the pattern but it preserves the signal level and the pattern in high frequency area much better than the other compared methods as shown in Fig. 5.11 (e).

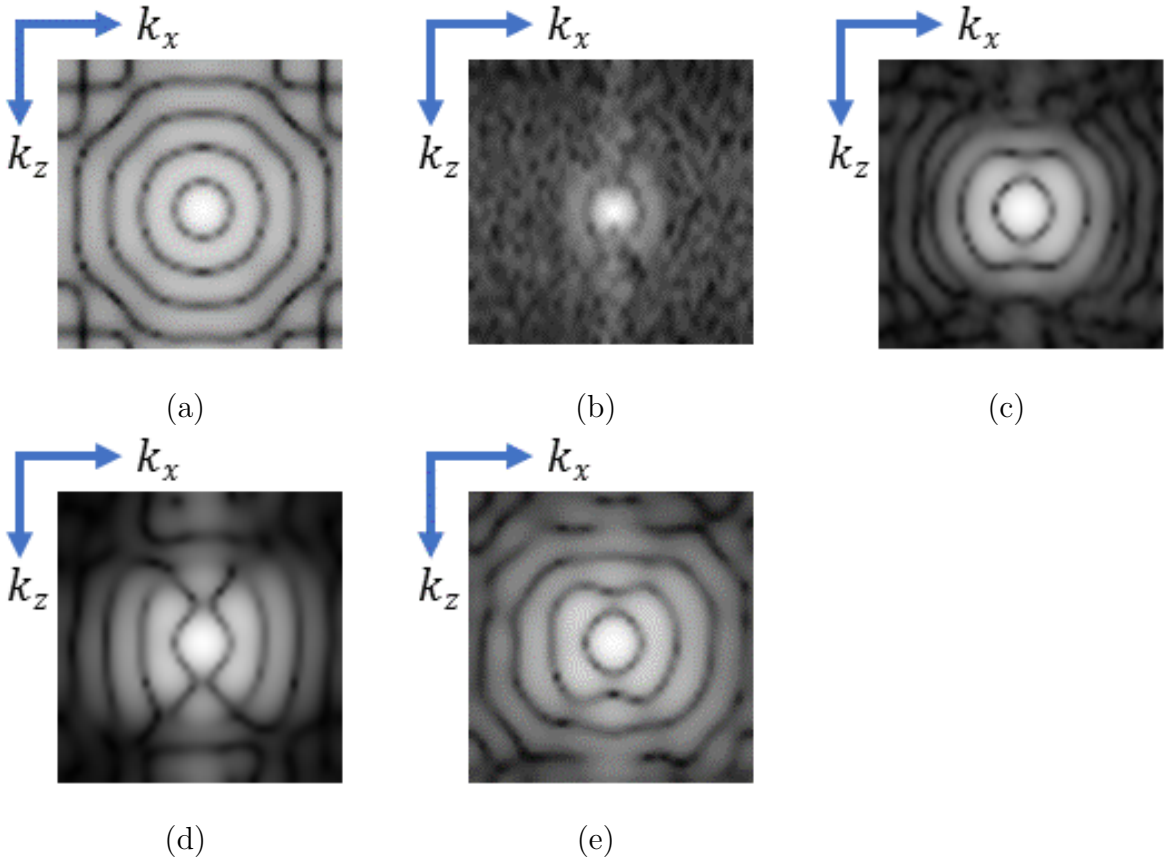

Figure 5.11. Slices in the k_zk_x-plane of the reconstructed One-ellipsoid image in the frequency domain. (a) Ground truth, (b) 3D stack of MFM tiles, (c) SPRIAL-TV, (d) JRL-TV, and (e) our method.

5.5.1.8. Choice of Penalty Parameter ρ. As mentioned in Section 5.3.2, we fix the penalty parameter of the augmented Lagrangian, ρ, to 1. We explain how we pick the value here. First of all, for any fixed ρ, the convergence of ADMM framework is proved [88].

Therefore, it is reasonable to use a fixed ρ, as long as the values of ρ significantly slow down the convergence. Secondly, we performed a grid search to find the better values for the parameters, ρ, and λ, which are the two parameters to be tuned in our method. We performed our algorithm on One-ellipsoid with MP 100. Note that we did not estimate λ but fixed it for each run in these simulations. Figure 5.12 shows the results of the grid search in PSNR and SSIM. From Figs. 5.12 (a) and (b), we observe that the performance does not depend on specific values of λ or ρ but depends on the ratio of these two parameters. The values of PSNR and SSIM in the same diagonal lines are consistent. In this case, the ratio $\lambda/\rho \approx 10^{-7}$ is the best in PSNR and $\lambda/\rho \approx 10^{-6}$ is the best in SSIM. It is interesting to see the different ratios in two different metrics. With the larger ratio, or the larger λ, the reconstructed image becomes more smooth conforming to the TV regularizer. The SSIM metric appreciates the smoothness of the image more than PSNR does.

5.5.2. Real Experiment

5.5.2.1. Experimental Data and Setup. We captured a video of a single bacterium tumbling at 25 frames per second (fps). The DOE of the MFM system is designed to produce 5-by-5 focal planes with 250 nm focal step. The effective pixel size of the camera is $108nm \times 108nm$, and its pixel resolution of the camera is 1024×1024. We reconstruct the 3D image of $150 \times 150 \times 101$ voxels with each voxel size being $108nm \times 108nm \times 200nm$, which is equivalent to $16.2\mu m \times 16.2\mu m \times 20.2\mu m$ in the sample space. The conversion factor for the camera sensor, a, is 139. MFM images at frames 1 and 30 are shown in Fig. 5.13. From the MFM image, we can tell that the bacterium lies on xy plane in Fig. 5.13 (a) and stands along the z-axis in Fig. 5.13 (b).

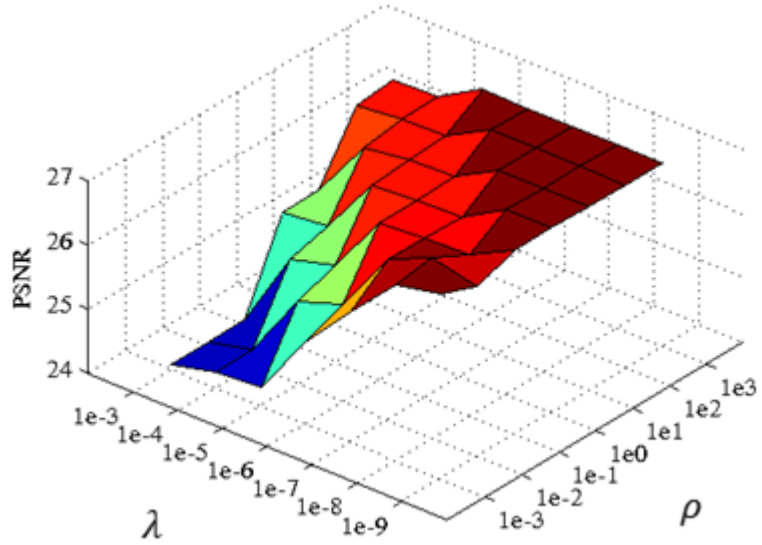

(a)

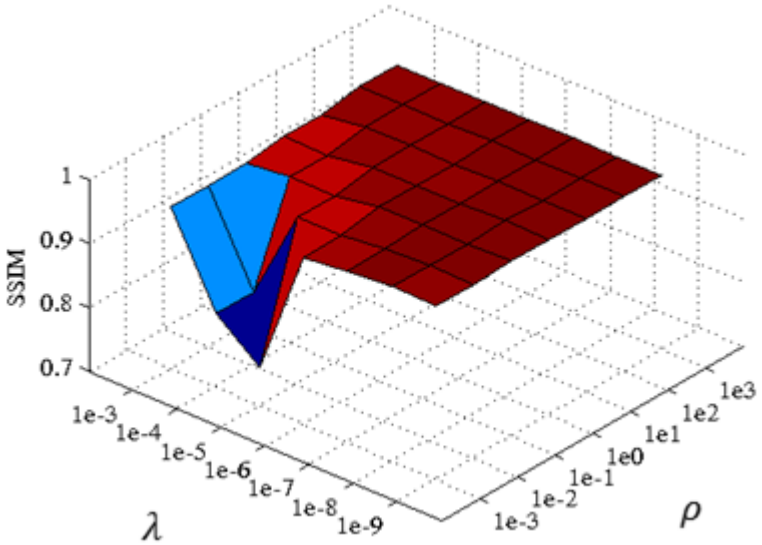

(b)

Figure 5.12. Grid search for ρ and λ in (a) PSNR and (b) SSIM.

Figures 5.14 and 5.15 show the 3D stack of MFM images and 3D images reconstructed by SPIRAL-TV, JRL-TV, and the proposed method from the experimental MFM images. Note that we crop a part of the 3D image that includes the bacterium in the figures for better visualization. Similarly to the simulation results, the 3D stack of MFM tiles has

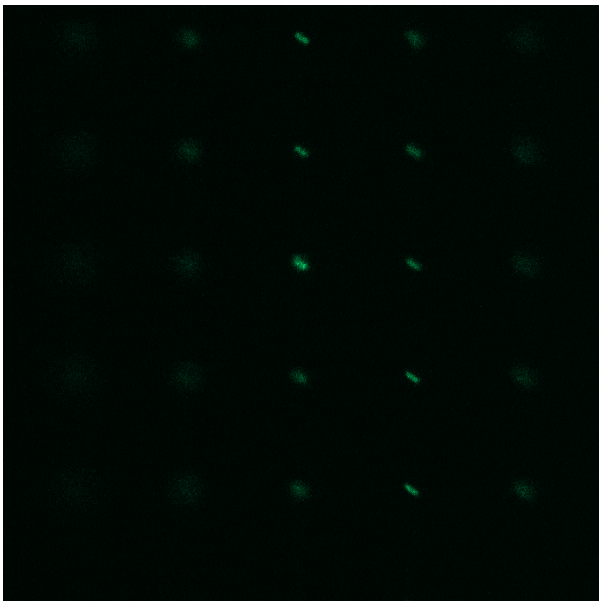

(a)

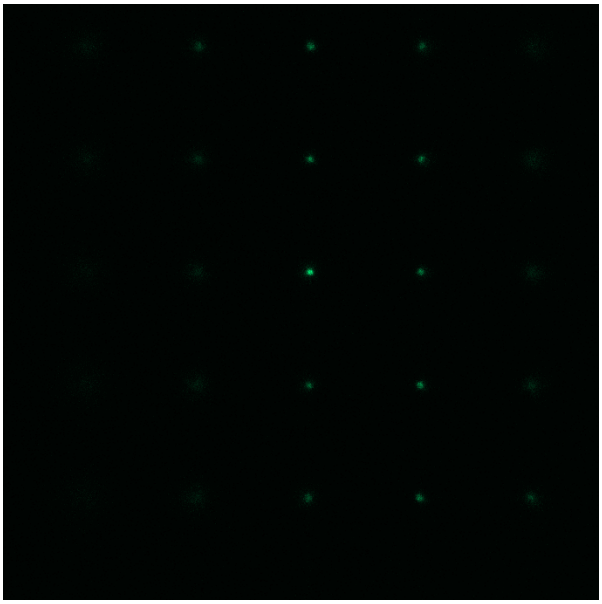

(b)

Figure 5.13. MFM experimental measurement of flourescently labelled sampels. A single tumbling bacterium at frames (a) 1 and (b) 30. The bacterium moves so it is in different poses and locations at the two frames.

poor resolution due to the remaining out-of-focus blur and noise from measurement. Non-uniform light distribution for each tile is also observed from the fact that the center tile has the highest intensity. In contrast, the other methods reconstruct the 3D image with high quality, reducing the blur and the noise. The reconstructed 3D image clearly shows the shape and the pose of the tumbling bacterium. The size and shape of the bacterium in the reconstruction match our prior knowledge. Also, it is clear from the reconstructions that the bacterium lies on xy plane at frame 1 and stands along the z-axis at frame 30. The reconstructed images from SPIRAL-TV, JRL-TV, and the proposed method are consistent in their shapes and positions. However, the reconstruction of SPIRAL-TV tends to be more smooth and thus loses some details, while those of JRL-TV and the proposed method preserve the details as shown in Fig. 5.15.

Table 5.4 compares the computation times of the three methods for the experimental MFM data. Note that maximum iteration is limited to 500 for this data instead of 200 for SPIRAL-TV and JRL-TV. The proposed method converges faster than JRL-TV. The reported time for SPIRAL-TV is for one parameter set but it is much longer if you consider trials of multiple parameter sets for parameter search.

Table 5.4. Computation time for 3D image reconstruction from MFM for real data. CPU time is in minutes.

Methods	SPIRAL-TV		JRL-TV		Ours	
Data	Time	Iter.	Time	Iter.	Time	Iter.
Frame 1	85.2	85	319.2	500	118.5	175
Frame 30	49.7	80	237.1	371	147.3	268

5.6. Conclusion

We have presented an ADMM based Poissonian image deconvolution algorithm for MFM that jointly estimate the regularization parameter and the background signal. By using

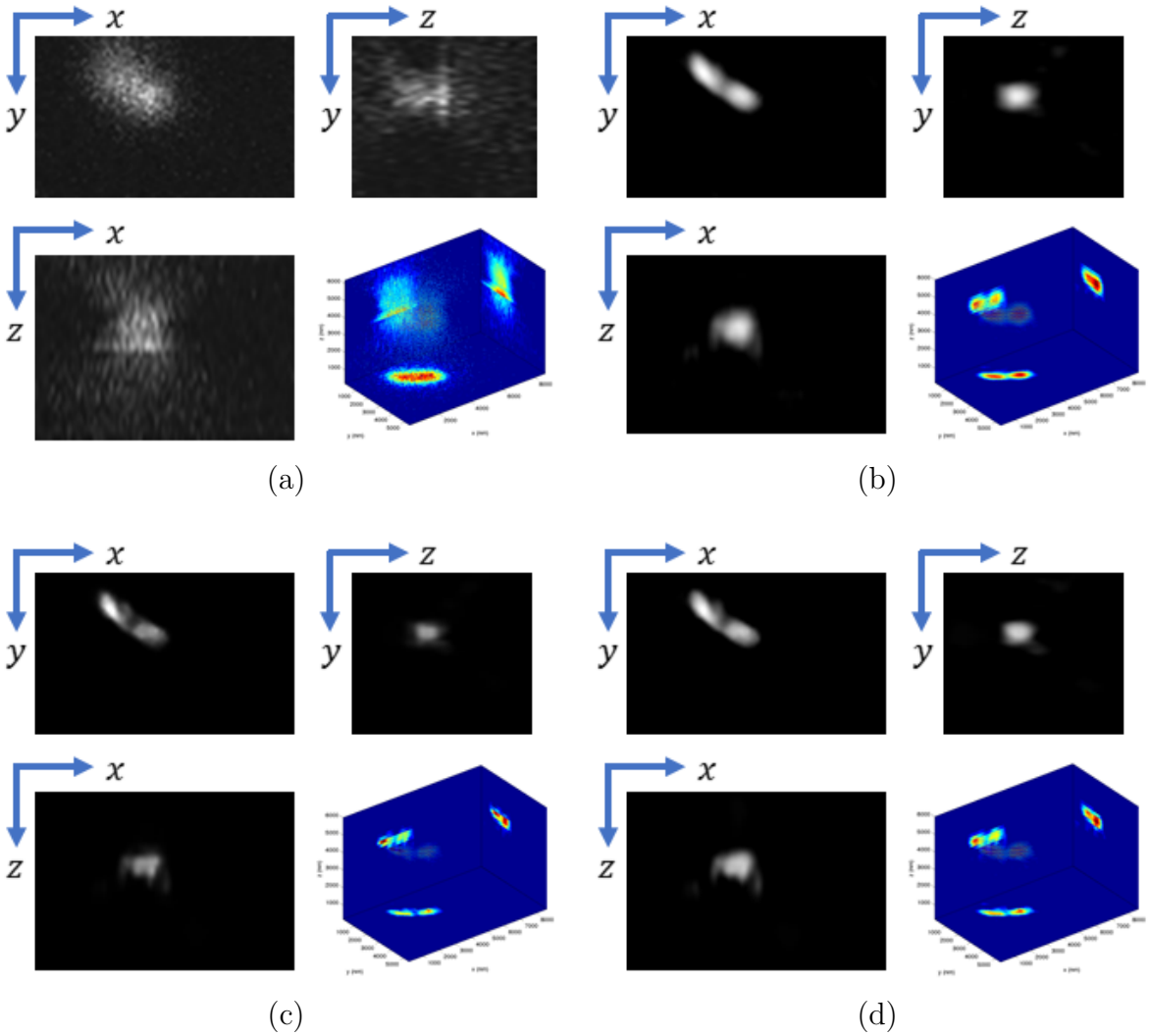

Figure 5.14. 3D image reconstruction from an experimental MFM measurement (frame 1). Scale bar indicates 1 μm. (a) 3D stack of MFM tiles, (b) SPIRAL-TV, $\lambda = 10^{-7}$, (c) JRL-TV, estimated $\lambda = 5.26 \times 10^{-4}$, and (d) our method, estimated $\lambda = 1.76 \times 10^{-5}$,

ADMM framework, the Poissonian deconvolution problem is split into two simpler problems - deblurring and Poisson denoising problems. For deblurring problem, we used the Bayesian approach developed in [75] to estimate the regularization parameter as well as the 3D image. Poisson denoising problem can be solved in a closed-form solution. The step for estimation of the background signal is also incorporated in our ADMM framework.

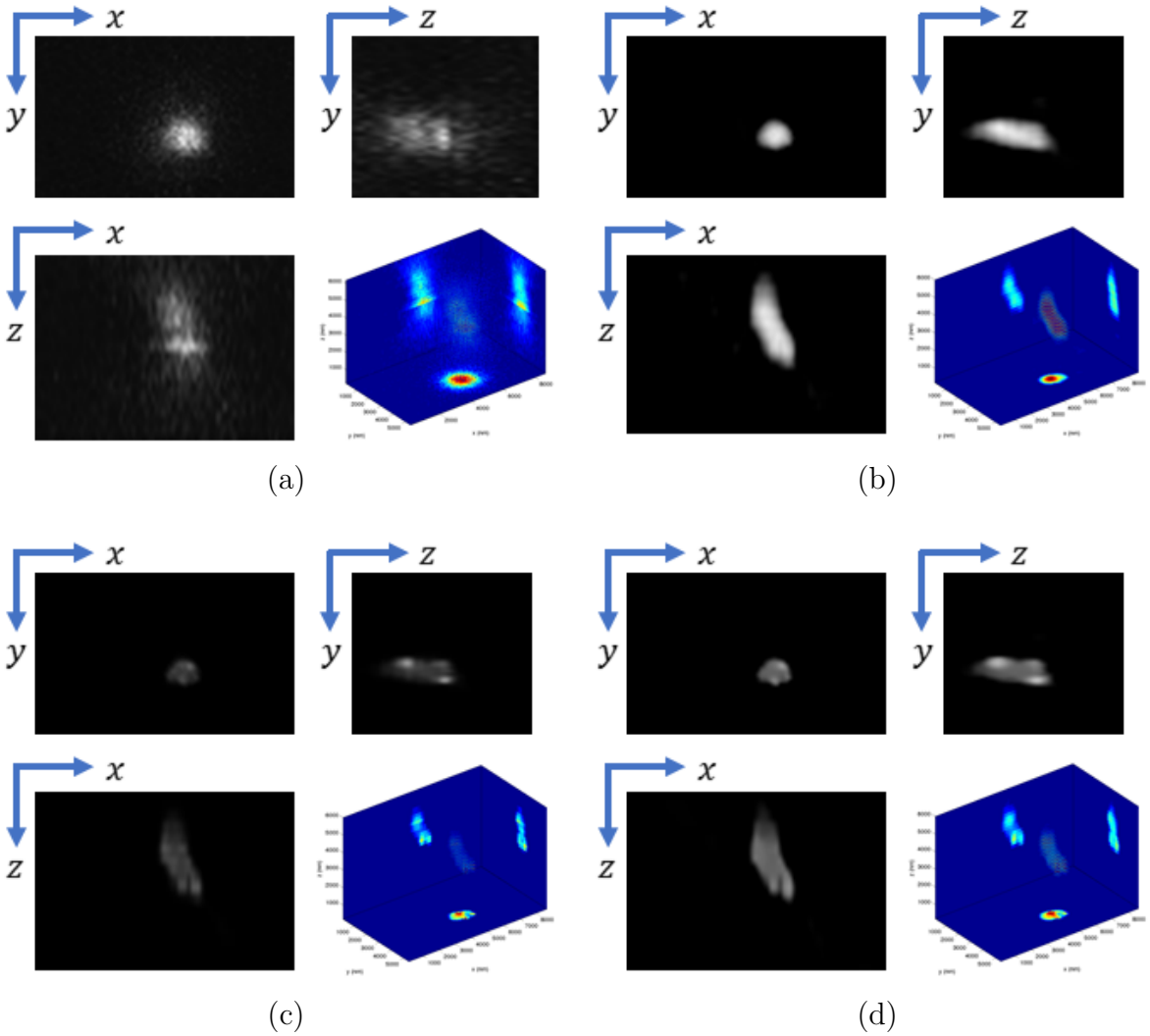

Figure 5.15. 3D image reconstruction from an experimental MFM measurement (frame 30). Scale bar indicates 1 μm. (a) 3D stack of MFM tiles, (b) SPIRAL-TV, $\lambda = 10^{-7}$, (c) JRL-TV, estimated $\lambda = 4.35 \times 10^{-4}$, and (d) our method, estimated $\lambda = 1.82 \times 10^{-5}$,

We achieve higher quality image reconstruction and faster convergence compared to other state-of-the-art methods.

CHAPTER 6

Conclusion

I have presented 3D image reconstruction algorithms for MFM. MFM provides a stack of focal planes with a single snapshot to achieve high temporal resolution for 3D imaging, but it does not provide high spatial resolution. The computational methods I have developed overcome this limitation. We started with modeling of the imaging process of MFM with two different noise models and developed the image reconstruction methods based on the image acquisition models. From the base method of TV-regularized RLS, we have further developed more advanced algorithms to improve the performance of image reconstruction by using (1) multiple-frame processing, (2) joint parameter estimation through a Bayesian framework, and (3) ADMM based Poisson image deconvolution. Multiple-frame processing utilizes the information from neighboring frames in addition to the current frame to improve the image quality. For joint parameter estimation, maximum-a-posteriori (MAP) is used for automatic estimation of the regularization parameter as well as 3D image reconstruction. Poisson noise model is considered to handle the low photon resource of MFM and ADMM framework is used to efficiently optimize the problem. Experimental results with synthetic and real data verify the effectiveness of the methods. The 3D image reconstruction algorithms that we developed make it possible to capture 4D (3D space + time) events of the samples through MFM.

There are still challenges and rooms for improvement. One is to use more accurate noise model. In reality, noise comes from multiple sources so we have to deal with mixed noise

model, for example, Gaussian noise + Poisson noise. Also, it is necessary to have the PSF information closer to the true PSF to obtain better reconstruction. The measured PSF contains a significant amount of noise as well as background signals even though it reflects the true PSF from the experimental setup better than the theoretical version. Applying a denoising algorithm can help to suppress the noise in the measured PSF, and finding a way to combine the theoretical and the measured PSFs can be a solution as well.

References

[1] Coling Donald and Kachar Bechara. Theory and application of fluorescence microscopy. *Current Protocols in Neuroscience*, 00(1):2.1.1–2.1.11, 2001.

[2] Christian A. Combs and Hari Shroff. Fluorescence microscopy: A concise guide to current imaging methods. *Current Protocols in Neuroscience*, 2017:2.1.1–2.1.25, apr 2017.

[3] Rongcheng Han, Zhenghong Li, Yanyan Fan, and Yuqiang Jiang. Recent Advances in Super-Resolution Fluorescence Imaging and Its Applications in Biology. *Journal of Genetics and Genomics*, 40(12):583–595, dec 2013.

[4] Alan R. Hibbs. *Confocal Microscopy for Biologists*. Springer US, Boston, MA, 2004.

[5] James B. Pawley, editor. *Handbook Of Biological Confocal Microscopy*. Springer US, Boston, MA, 2006.

[6] Neil, Squire, Jukaitis, Bastiaens, and Wilson. Widefield optically sectioning fluorescence microscopy with laser illumination. *Journal of Microscopy*, 197(1):1–4, 2000.

[7] Gustafsson M. G. L. Surpassing the lateral resolution limit by a factor of two using structured illumination microscopy. *Journal of Microscopy*, 198(2):82–87, 2000.

[8] Jan Huisken, Jim Swoger, Filippo Del Bene, Joachim Wittbrodt, and Ernst H. K. Stelzer. Optical sectioning deep inside live embryos by selective plane illumination microscopy. *Science*, 305(5686):1007–1009, 2004.

[9] Philipp J. Keller, Annette D. Schmidt, Joachim Wittbrodt, and Ernst H.K. Stelzer. Reconstruction of zebrafish early embryonic development by scanned light sheet microscopy. *Science*, 322(5904):1065–1069, 2008.

[10] Katrin I. Willig, Silvio O. Rizzoli, Volker Westphal, Reinhard Jahn, and Stefan W. Hell. Sted microscopy reveals that synaptotagmin remains clustered after synaptic vesicle exocytosis. *Nature*, 440:935–939, 2006.

[11] R.R. Kellner, C.J. Baier, K.I. Willig, S.W. Hell, and F.J. Barrantes. Nanoscale organization of nicotinic acetylcholine receptors revealed by stimulated emission depletion microscopy. *Neuroscience*, 144(1):135–143, 2007.

[12] Prashant Prabhat, Sripad Ram, E Sally Ward, and Raimund J Ober. Simultaneous imaging of different focal planes in fluorescence microscopy for the study of cellular dynamics in three dimensions. *IEEE transactions on nanobioscience*, 3(4):237–42, dec 2004.

[13] Prashant Prabhat, Sripad Ram, E. Sally Ward, and Raimund J. Ober. Simultaneous imaging of several focal planes in fluorescence microscopy for the study of cellular dynamics in 3D. volume 6090, page 60900L. International Society for Optics and Photonics, feb 2006.

[14] Sara Abrahamsson, Jiji Chen, Bassam Hajj, Sjoerd Stallinga, Alexander Y Katsov, Jan Wisniewski, Gaku Mizuguchi, Pierre Soule, Florian Mueller, Claire Dugast Darzacq, Xavier Darzacq, Carl Wu, Cornelia I Bargmann, David A Agard, Maxime Dahan, and Mats G L Gustafsson. Fast multicolor 3D imaging using aberration-corrected multifocus microscopy. *Nature Methods*, 10(1):60–63, 2012.

[15] Sara Abrahamsson, Rob Ilic, Jan Wisniewski, Brian Mehl, Liya Yu, Lei Chen, Marcelo Davanco, Laura Oudjedi, Jean-Bernard Fiche, Bassam Hajj, Xin Jin, Joan Pulupa, Christine Cho, Mustafa Mir, Mohamed El Beheiry, Xavier Darzacq, Marcelo Nollmann, Maxime Dahan, Carl Wu, Timothée Lionnet, J. Alexander Liddle, and Cornelia I. Bargmann. Multifocus microscopy with precise color multi-phase diffractive optics applied in functional neuronal imaging. *Biomed. Opt. Express*, 7(3):855–869, Mar 2016.

[16] Laura Oudjedi, Jean-Bernard Fiche, Sara Abrahamsson, Laurent Mazenq, Aurélie Lecestre, Pierre-François Calmon, Aline Cerf, and Marcelo Nöllmann. Astigmatic multifocus microscopy enables deep 3d super-resolved imaging. *Biomed. Opt. Express*, 7(6):2163–2173, Jun 2016.

[17] X. Huang, A. Selewa, X. Wang, M. K. Daddysman, I. Gdor, R. Wilton, K. M. Kemner, S. Yoo, A. K. Katsaggelos, O. Cossairt, N. J. Ferrier, M. Hereld, and N. F. Scherer. 3D snapshot microscopy of extended objects, arXiv:1802.01565, 2018.

[18] Xiaolei Wang, Xiang Huang, Itay Gdor, Matthew Daddysman, Hannah Yi, Alan Selewa, Theresa Haunold, Mark Hereld, and Norbert Scherer. Snapshot 3D tracking of insulin granules in live cells. In Thomas G. Brown, Carol J. Cogswell, and Tony Wilson,

editors, *Three-Dimensional and Multidimensional Microscopy: Image Acquisition and Processing XXV*, volume 10499, page 17. SPIE, feb 2018.

[19] William Hadley Richardson. Bayesian-based iterative method of image restoration∗. *J. Opt. Soc. Am.*, 62(1):55–59, Jan 1972.

[20] L. B. Lucy. An iterative technique for the rectification of observed distributions. *Astron. J.*, 79:745, June 1974.

[21] M. R. Banham and A. K. Katsaggelos. Digital image restoration. *IEEE Signal Processing Magazine*, 14(2):24–41, Mar 1997.

[22] V Z Mesarovic, N P Galatsanos, and Aggelos K. Katsaggelos. Regularized Constrained Total Least-Squares Image-Restoration. *Ieee Transactions on Image Processing*, 4:1096–1108, 1995.

[23] R. Molina, J. Mateos, and A. K. Katsaggelos. Blind deconvolution using a variational approach to parameter, image, and blur estimation. *IEEE Transactions on Image Processing*, 15(12):3715–3727, Dec 2006.

[24] J. M. Bioucas-Dias and M. A. T. Figueiredo. A new TwIST: Two-step iterative shrinkage/thresholding algorithms for image restoration. *IEEE Transactions on Image Processing*, 16(12):2992–3004, 2007.

[25] Amir Beck and Marc Teboulle. A Fast Iterative Shrinkage-Thresholding Algorithm. *Society for Industrial and Applied Mathematics Journal on Imaging Sciences*, 2(1):183–202, 2009.

[26] D. Babacan, R. Molina, and A. Katsaggelos. Variational bayesian blind deconvolution using a total variation prior. *IEEE Transactions on Image Processing*, 18(1):12–26, 2009.

[27] Anat Levin, Yair Weiss, Fredo Durand, and William T. Freeman. Understanding blind deconvolution algorithms. *IEEE Transactions on Pattern Analysis and Machine Intelligence*, 33(12):2354–2367, 2011.

[28] Jimmy S J Li Xu, Ren. Deep convolutional neural network for image deconvolution. *Advances in Neural Information Processing Systems*, (413113):1–9, 2014.

[29] P. Ruiz, X. Zhou, J. Mateos, R. Molina, and A. K. Katsaggelos. Variational Bayesian Blind Image Deconvolution: A review. *Digital Signal Processing*, 47:116–127, December 2015.

[30] Rob Fergus, Barun Singh, Aaron Hertzmann, Sam T. Roweis, and William T. Freeman. Removing camera shake from a single photograph. *ACM Transactions on Graphics*, 25(3):787, 2006.

[31] Sunghyun Cho and Seungyong Lee. Fast motion deblurring. *ACM Trans. Graph.*, 28(5):145:1–145:8, December 2009.

[32] Dilip Krishnan and Rob Fergus. Fast image deconvolution using hyper-laplacian priors. *Advances in Neural Information Processing Systems*, pages 1–9, 2009.

[33] Whyte O, Sivic J, Zisserman A, and Ponce J. Non-uniform deblurring for shaken images. *International Journal of Computer Vision*, 98(2):168–186, 2012.

[34] Aram Danielyan, Vladimir Katkovnik, and Karen Egiazarian. BM3D frames and variational image deblurring. *IEEE Transactions on Image Processing*, 21(4):1715–1728, 2012.

[35] L. I. Rudin, S. Osher, and E. Fatemi. Nonlinear total variation based noise removal algorithms. *Physica D: Nonlinear Phenomena*, 60(1):259–268, November 1992.

[36] Antonin Chambolle. An Algorithm for Total Variation Minimization and Applications. *Journal of Mathematical Imaging and Vision*, 20:89–97, 2004.

[37] Antoni Buades, Bartomeu Coll, Jean-Michel Morel CMLA, and Ens Cachan. A nonlocal algorithm for image denoising. *CVPR*, 2005.

[38] K. Dabov, A. Foi, V. Katkovnik, and K. Egiazarian. Image denoising by sparse 3-d transform-domain collaborative filtering. *IEEE Transactions on Image Processing*, 16(8):2080–2095, aug 2007.

[39] Vladimir Katkovnik, Alessandro Foi, Karen Egiazarian, and Jaakko Astola. From local kernel to nonlocal multiple-model image denoising. *International Journal of Computer Vision*, 86(1):1–32, jan 2010.

[40] Michael Elad and Michal Aharon. Image denoising via sparse and redundant representations over learned dictionaries. *IEEE Transactions on Image Processing*, 15(12):2008, 2008.

[41] Yu He, Kim Hui Yap, Li Chen, and Lap Pui Chau. A nonlinear least square technique for simultaneous image registration and super-resolution. *IEEE Transactions on Image Processing*, 16(11):2830–2841, 2007.

[42] Stefanos P. Belekos, Nikolaos P. Galatsanos, and Aggelos K. Katsaggelos. Maximum a posteriori video super-resolution using a new multichannel image prior. *IEEE Transactions on Image Processing*, 19(6):1451–1464, 2010.

[43] Derin K Babacan, Rafael Molina, and Aggelos K Katsaggelos. Variational Bayesian Super Resolution. *IEEE Transactions on Image Processing*, 20(4):984–999, 2011.

[44] Ce Liu and Deqing Sun. On Bayesian Adaptive Video Super Resolution. *IEEE Transactions on Pattern Analysis and Machine Intelligence*, 36(2)(2):346–360, 2014.

[45] Ziyang Ma, Renjie Liao, Xin Tao, Li Xu, Jiaya Jia, and Enhua Wu. Handling Motion Blur in Multi-Frame Super-Resolution. *CVPR*, 07-12-June(d):5224–5232, 2015.

[46] Armin Kappeler, Seunghwan Yoo, Qiqin Dai, and Aggelos K. Katsaggelos. Video Super-Resolution with Convolutional Neural Networks. *IEEE Transactions on Computational Imaging*, PP(99):1–1, 2016.

[47] Qiqin Dai, Seunghwan Yoo, Armin Kappeler, and Aggelos K Katsaggelos. Sparse Representation-Based Multiple Frame Video Super-Resolution. *IEEE Transactions on Image Processing*, 26(2):765–781, 2017.

[48] P. Sarder and A. Nehorai. Deconvolution methods for 3-D fluorescence microscopy images. *IEEE Signal Processing Magazine*, 23(3):32–45, May 2006.

[49] R. M. Willett and R. D. Nowak. Platelets: a multiscale approach for recovering edges and surfaces in photon-limited medical imaging. *IEEE Transactions on Medical Imaging*, 22(3):332–350, March 2003.

[50] Chrysanthe Preza and José-Angel Conchello. Depth-variant maximum-likelihood restoration for three-dimensional fluorescence microscopy. *Journal of the Optical Society of America A*, 21(9):1593, Sept. 2004.

[51] Boyoung Kim and Takeshi Naemura. Blind Depth-variant Deconvolution of 3D Data in Wide-field Fluorescence Microscopy. *Scientific Reports*, 5(1):9894, Sept. 2015.

[52] M Bertero, P Boccacci, G Desider, and G Vicidomini. Image deblurring with Poisson data: from cells to galaxies. *Inverse Problems*, 25(12):123006, 2009.

[53] H. Lantéri and C. Theys. Restoration of astrophysical images—the case of Poisson data with additive Gaussian noise. *EURASIP Journal on Advances in Signal Processing*, 2005(15):643143, Sep 2005.

[54] G.T. Herman. *Fundamentals of Computerized Tomography: Image Reconstruction from Projections*. Advances in Computer Vision and Pattern Recognition. Springer London, 2009.

[55] Doğa Gürsoy, Francesco De Carlo, Xianghui Xiao, and Chris Jacobsen. TomoPy: a framework for the analysis of synchrotron tomographic data. *Journal of Synchrotron Radiation*, 21(5):1188–1193, Sep 2014.

[56] Doa Gürsoy, Young P. Hong, Kuan He, Karl Hujsak, Seunghwan Yoo, Si Chen, Yue Li, Mingyuan Ge, Lisa M. Miller, Yong S. Chu, Vincent De Andrade, Kai He, Oliver Cossairt, Aggelos K. Katsaggelos, and Chris Jacobsen. Rapid alignment of nanotomography data using joint iterative reconstruction and reprojection. *Scientific Reports*, 7(1):11818, dec 2017.

[57] Oliver Cossairt, Kuan He, Ruibo Shang, Nathan Matsuda, Manoj Sharma, Xiang Huang, Aggelos K. Katsaggelos, Leonidas Spinoulas, and Seunghwan Yoo. Compressive reconstruction for 3D incoherent holographic microscopy. *Proceedings of the IEEE International Conference on Image Processing*, 2016-Augus(2):958–962, 2016.

[58] J. P. Oliveira, J. M. Bioucas-Dias, and M. A.T. Figueiredo. Adaptive total variation image deblurring: A majorizationminimization approach. *Signal Processing*, 89(9):1683–1693, 2009.

[59] D.L. Donoho. Compressed sensing. *IEEE Transactions on Information Theory*, 52(4):1289–1306, apr 2006.

[60] E.J. Candes, J. Romberg, and T. Tao. Robust uncertainty principles: exact signal reconstruction from highly incomplete frequency information. *IEEE Transactions on Information Theory*, 52(2):489–509, feb 2006.

[61] E.J. Candes and M.B. Wakin. An Introduction To Compressive Sampling. *IEEE Signal Processing Magazine*, 25(2):21–30, 2008.

[62] M. A. T. Figueiredo and R. D. Nowak. An em algorithm for wavelet-based image restoration. *IEEE Transactions on Image Processing*, 12(8):906–916, Aug 2003.

[63] Daubechies I., Defrise M., and De Mol C. An iterative thresholding algorithm for linear inverse problems with a sparsity constraint. *Communications on Pure and Applied Mathematics*, 57(11):1413–1457.

[64] RY Tsai. Multiframe image restoration and registration. *Adv. Comput. Vis. Image Process.*, 1(2):317–339, 1984.

[65] Sina Farsiu, Dirk Robinson, Michael Elad, and Peyman Milanfar. Fast and Robust Multi-Frame Super-Resolution. *IEEE Transactions on Image Processing*, 13(10):1327–1344, 2004.

[66] F. Macias-Garza, A. C. Bovik, K. R. Diller, S. J. Aggarwal, and J. K. Aggarwal. The missing cone problem and low-pass distortion in optical serial sectioning microscopy. In *Proc. IEEE International Conference on Acoustics, Speech, and Signal Processing*, pages 890–893, 1988.

[67] J. Lim, K. Lee, K. Jin, S. Shin, S. Lee, Y. Park, and J. Ye. Comparative study of iterative reconstruction algorithms for missing cone problems in optical diffraction tomography. *Optics express*, 23(13):16933–48, June 2015.

[68] S. Yoo, P. Ruiz, X. Huang, K. He, N. J. Ferrier, M. Hereld, A. Selewa, M. Daddysman, N. Scherer, O. Cossairt, and A. K. Katsaggelos. 3D image reconstruction from multi-focus microscope: axial super-resolution and multiple-frame processing. In *Proc. IEEE Int. Conf. Acoustic, Speech, and Signal Processing*, Apr. 2018.

[69] S.D. Babacan. *Bayesian Techniques for Image Recovery*. PhD thesis, Northwestern University, 2009.

[70] S.J.D. Prince. *Computer Vision: Models Learning and Inference*. Cambridge University Press, 2012.

[71] R. Molina. On the hierarchical Bayesian approach to image restoration: applications to astronomical images. *IEEE Transactions on Pattern Analysis and Machine Intelligence*, 16(11):1122–1128, 1994.

[72] S. D. Babacan, R. Ansorge, M. Luessi, P. R. Matarán, R. Molina, and A. K. Katsaggelos. Compressive Light Field Sensing. *IEEE Transactions on Image Processing*, 21(12):4746–4757, December 2012.

[73] J. M. Bioucas-Dias, M. A. T. Figueiredo, and J. P. Oliveira. Total variation-based image deconvolution: a majorization-minimization approach. In *Proc. IEEE International Conference on Acoustics Speech and Signal Processing*, volume 2, 2006.

[74] T. L. Jensen, J. H. Jørgensen, P. C. Hansen, and S. H. Jensen. Implementation of an optimal first-order method for strongly convex total variation regularization. *BIT Numerical Mathematics*, 52(2):329–356, June 2012.

[75] S. Yoo, P. Ruiz, X. Huang, K. He, X. Wang, I. Gdor, A. Selewa, M. Daddysman, N. J. Ferrier, M. Hereld, N. Scherer, O. Cossairt, and A. K. Katsaggelos. Bayesian approach for automatic joint parameter estimatioin in 3D image reconstruction from multi-focus microscope. In *Proc. IEEE Int. Conf. Image Processing*, Oct. 2018.

[76] K. He. Computational multifocus microscopy. *Optica*, 2018.

[77] Donald L. Snyder, Abed M. Hammoud, and Richard L. White. Image recovery from data acquired with a charge-coupled-device camera. *J. Opt. Soc. Am. A*, 10(5):1014–1023, May 1993.

[78] Bratsolis, E. and Sigelle, M. A spatial regularization method preserving local photometry for Richardson-Lucy restoration. *A&A*, 375(3):1120–1128, 2001.

[79] Nicolas Dey, Laure Blanc-Féraud, Christophe Zimmer, Pascal Roux, Zvi Kam, Jean-Christophe Olivo-Marin, and Josiane Zerubia. 3D microscopy deconvolution using Richardson-Lucy algorithm with total variation regularization. *INRIA*, 71, 2004.

[80] M Laasmaa, M Vendelin, and P Peterson. Application of regularized Richardson-Lucy algorithm for deconvolution of confocal microscopy images. *Journal of microscopy*, 243(2):124–40, aug 2011.

[81] H. Wang and P. C. Miller. Scaled heavy-ball acceleration of the Richardson-Lucy algorithm for 3d microscopy image restoration. *IEEE Transactions on Image Processing*, 23(2):848–854, Feb 2014.

[82] J. Li, F. Luisier, and T. Blu. PURE-LET image deconvolution. *IEEE Transactions on Image Processing*, 27(1):92–105, Jan 2018.

[83] *Fast regularization technique for expectation maximization algorithm for optical sectioning microscopy*, volume 2655, 1996.

[84] G. M P Van Kempen and L. J. Van Vliet. The influence of the regularization parameter and the first estimate on the performance of Tikhonov regularized non-linear image restoration algorithms. *Journal of Microscopy*, 198(1):63–75, apr 2000.

[85] Zachary T Harmany, Roummel F Marcia, and Rebecca M Willett. This is SPIRAL-TAP: Sparse Poisson Intensity Reconstruction ALgorithms Theory and Practice. *IEEE Transactions on Image Processing*, 21(5):1–11, 2012.

[86] Mário A.T. Figueiredo and José M. Bioucas-Dias. Restoration of poissonian images using alternating direction optimization. *IEEE Transactions on Image Processing*, 19(12):3133–3145, 2010.

[87] S. Setzer, G. Steidl, and T. Teuber. Deblurring Poissonian images by split Bregman techniques. *Journal of Visual Communication and Image Representation*, 21(3):193–199, apr 2010.

[88] Stephen Boyd, Neal Parikh, Eric Chu, and Jonathan Eckstein. *Distributed Optimization and Statistical Learning via the Alternating Direction Method of Multipliers*, volume xx. 2010.

[89] Arie Rond, Raja Giryes, and Michael Elad. Poisson inverse problems by the Plug-and-Play scheme. *Journal of Visual Communication and Image Representation*, 41:96–108, nov 2016.

[90] Yilun Wang, Junfeng Yang, Wotao Yin, and Yin Zhang. A new alternating minimization algorithm for total variation image reconstruction. *SIAM J. Img. Sci.*, 1(3):248–272, August 2008.

[91] Junfeng Yang, Wotao Yin, Yin Zhang, and Yilun Wang. A fast algorithm for edge-preserving variational multichannel image restoration. *SIAM Journal on Imaging Sciences*, 2(2):569–592, jan 2009.

[92] Joachim Dahl, Per Christian Hansen, Søren Holdt Jensen, and Tobias Lindstrøm Jensen. Algorithms and software for total variation image reconstruction via first-order methods. *Numerical Algorithms*, 53(1):67–92, jan 2010.

[93] Neal Parikh and Stephen Boyd. Proximal Algorithms. *Foundations and Trends R in Optimization*, 1(3):123–231, 2013.

[94] Suhas Sreehari, Singanallur V. Venkatakrishnan, Brendt Wohlberg, Lawrence F. Drummy, Jeffrey P. Simmons, and Charles A. Bouman. Plug-and-play priors for bright field electron tomography and sparse interpolation. *IEEE Transactions on Computational Imaging*, pages 1–1, 2015.

[95] Stanley H. Chan, Xiran Wang, and Omar A. Elgendy. Plug-and-Play ADMM for image restoration: fixed point convergence and applications. *IEEE Transactions on Computational Imaging*, 3(1):84–98, 2017.

[96] John W. Sedat Mats G. L. Gustafsson, David A. Agard. Sevenfold improvement of axial resolution in 3d wide-field microscopy using two objective lenses, 1995.

APPENDIX A

Derivation of MFM Degradation Model

In this section, we derive Equation 3.2 from Equation 3.1 in detail.

$$
\begin{aligned}
g(x,y) &= f(x,y,z) *_{3D} h(x,y,z)\Big|_{z=0} + \epsilon(x,y) && \text{(A.1)}\\
&= \sum_{x'}\sum_{y'}\sum_{z'=-\lfloor N_z/2\rfloor}^{\lfloor N_z/2\rfloor} f(x-x',y-y',z-z')h(x',y',z')\Big|_{z=0} + \epsilon(x,y) && \text{(A.2)}\\
&= \sum_{x'}\sum_{y'}\sum_{z'=-\lfloor N_z/2\rfloor}^{\lfloor N_z/2\rfloor} f(x-x',y-y',-z')h(x',y',z') + \epsilon(x,y) && \text{(A.3)}\\
&= \sum_{z'=-\lfloor N_z/2\rfloor}^{\lfloor N_z/2\rfloor}\sum_{x'}\sum_{y'} f(x-x',y-y',-z')h(x',y',z') + \epsilon(x,y) && \text{(A.4)}\\
&= \sum_{z'=-\lfloor N_z/2\rfloor}^{\lfloor N_z/2\rfloor}\sum_{x'}\sum_{y'} f'(x-x',y-y',z')h(x',y',z') + \epsilon(x,y) && \text{(A.5)}\\
&= \sum_{z'=-\lfloor N_z/2\rfloor}^{\lfloor N_z/2\rfloor} f'(x,y;z') *_{2D} h(x,y;z') + \epsilon(x,y) && \text{(A.6)}\\
&= \sum_{z=-\lfloor N_z/2\rfloor}^{\lfloor N_z/2\rfloor} f'(x,y;z) *_{2D} h(x,y;z) + \epsilon(x,y) && \text{(A.7)}
\end{aligned}
$$

where $f'(x,y,z) = f(x,y,-z)$, and N_z is the number of focal planes in object space, and we can assume it is an odd number without loss of generality.

Let $\mathbf{f}_z \in R^{N_xN_y\times 1}$ and $\mathbf{g} \in R^{M_xM_y\times 1}$ denote vectorized $f'(x,y;z)$ and $g(x,y)$, respectively. The 2D convolution of $f'(x,y;z)$ and $h(x,y;z)$ can be expressed as matrix-vector multiplication by constructing the PSF matrix, $\mathbf{H}_z \in R^{M_xM_y\times N_xN_y}$, in lexicographical way.

$$\mathbf{g} = \sum_{z=-\lfloor N_z/2 \rfloor}^{\lfloor N_z/2 \rfloor} \mathbf{H}_z \mathbf{f}_z + \epsilon \tag{A.8}$$

$$= \left[\mathbf{H}_{-\lfloor N_z/2 \rfloor} \cdots \mathbf{H}_{\lfloor N_z/2 \rfloor}\right] \left[\mathbf{f}^T_{-\lfloor N_z/2 \rfloor} \cdots \mathbf{f}^T_{\lfloor N_z/2 \rfloor}\right]^T + \epsilon \tag{A.9}$$

$$= \mathbf{H}\mathbf{f} + \epsilon \tag{A.10}$$

where $\mathbf{H} = \left[\mathbf{H}_{-\lfloor N_z/2 \rfloor} \cdots \mathbf{H}_{\lfloor N_z/2 \rfloor}\right] \in R^{M_x M_y \times N_x N_y N_z}$, and $\mathbf{f} = \left[\mathbf{f}^T_{-\lfloor N_z/2 \rfloor} \cdots \mathbf{f}^T_{\lfloor N_z/2 \rfloor}\right]^T$ $\in R^{N_x N_y N_z \times 1}$.

APPENDIX B

Derivation of Solutions for u and b in ADMM Formulation

In this section, we derive the equations in Chapter 5.

First, we derive the closed-form solution for estimation of $\mathbf{u}^{k+1}$ in Eq. 5.22. We will omit the superscript $k+1$ above $\mathbf{u}$ for simplicity. Let $J(\mathbf{u})$ denotes the objective function for estimation of $\mathbf{u}$.

$$J(\mathbf{u}) = \mathcal{L}_u(\mathbf{u}) + \frac{\rho}{2}\|\mathbf{u} - \boldsymbol{\nu}^{k+1}\|_2^2 \tag{B.1}$$

$$= \sum_{i=1}^{M} \left\{ \left[\mathbf{u}\right]_i - \mathbf{g}_i/a \log \left[\mathbf{u}\right]_i \right\} + \frac{\rho}{2}\|\mathbf{u} - \boldsymbol{\nu}^{k+1}\|_2^2 \tag{B.2}$$

$$J(\mathbf{u}_i) = \left\{ \left[\mathbf{u}\right]_i - \mathbf{g}_i/a \log \left[\mathbf{u}\right]_i \right\} + \frac{\rho}{2}\left(\mathbf{u}_i - \boldsymbol{\nu}_i^{k+1}\right)^2 \tag{B.3}$$

$$\frac{dJ(\mathbf{u}_i)}{d\mathbf{u}_i} = 1 - \frac{\mathbf{g}_i/a}{\mathbf{u}_i} + \rho\mathbf{u}_i - \rho\boldsymbol{\nu}_i^{k+1} \tag{B.4}$$

$$\frac{dJ(\mathbf{u}_i)}{d\mathbf{u}_i} = \mathbf{0} \tag{B.5}$$

$$1 - \frac{\mathbf{g}_i/a}{\mathbf{u}_i} + \rho\mathbf{u}_i - \rho\boldsymbol{\nu}_i^{k+1} = \mathbf{0} \tag{B.6}$$

$$\mathbf{u}_i - \mathbf{g}_i/a + \rho\mathbf{u}_i^2 - \rho\boldsymbol{\nu}_i^{k+1}\mathbf{u}_i = \mathbf{0} \tag{B.7}$$

$$\rho\mathbf{u}_i^2 + (1 - \rho\boldsymbol{\nu}_i^{k+1})\mathbf{u}_i - \mathbf{g}_i/a = \mathbf{0} \tag{B.8}$$

$$\mathbf{u}_i = \frac{(\rho\boldsymbol{\nu}_i^{k+1} - 1) + \sqrt{(\rho\boldsymbol{\nu}_i^{k+1} - 1)^2 + 4\rho\mathbf{g}_i/a}}{2\rho}. \tag{B.9}$$

Second, we derive the closed-form solution for estimation of $\mathbf{b}^{k+1}$ in Eq. 5.27 and Eq. 5.28. We will omit the superscript $k+1$ above $\mathbf{b}$ for simplicity. Let $J(\mathbf{b})$ denotes the objective function for estimation of $\mathbf{b}$.

$$J(\mathbf{b}) = \|\mathbf{b} - \boldsymbol{\gamma}^{k+1}\|_2^2 \tag{B.10}$$

$$= \mathbf{b}^T\mathbf{b} - 2\boldsymbol{\gamma}^{k+1^T}\mathbf{b} + \boldsymbol{\gamma}^{k+1^T}\boldsymbol{\gamma}^{k+1} \tag{B.11}$$

$$= \sum_i^M \left\{\mathbf{b}_i^2 - 2\boldsymbol{\gamma}_i^{k+1}\mathbf{b}_i + \boldsymbol{\gamma}_i^{k+1^2}\right\} \tag{B.12}$$

$$\frac{dJ(\mathbf{b})}{d\mathbf{b}_i} = 2\mathbf{b}_i - 2\boldsymbol{\gamma}^{k+1} \tag{B.13}$$

$$\mathbf{b}_i = \boldsymbol{\gamma}_i^{k+1} \tag{B.14}$$

$$\mathbf{b} = \boldsymbol{\gamma}^{k+1}. \tag{B.15}$$

If $\mathbf{b} = b\mathbf{1}$,

$$J(\mathbf{b}) = \sum_i^M \left\{b^2 - 2\boldsymbol{\gamma}_i^{k+1}b + \boldsymbol{\gamma}_i^{k+1^2}\right\} \tag{B.16}$$

$$\frac{dJ(\mathbf{b})}{db} = \sum_i^M \left\{2Mb - 2\boldsymbol{\gamma}^{k+1}\right\} \tag{B.17}$$

$$b = \frac{1}{M}\sum_i^M \boldsymbol{\gamma}_i^{k+1}. \tag{B.18}$$

This dissertation was typeset with LaTeX 2_ε[1] by the author.

[1]The macros used in formatting this dissertation are based on those written by Miguel A. Lerma, (Mathematics, Northwestern University) which have been further modified by Debjit Sinha (EECS, Northwestern University) to accommodate electronic dissertation formatting guidelines.